NANYANG TECHNOLOGICAL UNIVERSITY

TANTALUM BASED AMORPHOUS THIN FILMS AS COPPER DIFFUSION BARRIER

YAN HUA
SCHOOL OF MATERIALS SCIENCE AND ENGINEERING
2012

TANTALUM BASED AMORPHOUS THIN FILMS AS COPPER DIFFUSION BARRIER
YAN HUA
2012

TANTALUM BASED AMORPHOUS THIN FILMS AS COPPER DIFFUSION BARRIER

YAN HUA

School of Materials Science and Engineering

A thesis submitted to the Nanyang Technological University
in fulfillment of requirement of the degree of
Doctor Philosophy

2012

Abstract

This dissertation presents a study of Ta-based Cu diffusion barrier for advanced semiconductor technology. With the fast development of semiconductor industry, a novel barrier is required in order to address two challenges in the back-end-of-line technology: enhancing the interconnect reliability of back-end-of-line and reducing resistance-capacitance delay faced during further scaling of semiconductor devices.

Two groups of thin film barriers formed on two distinctive principles are studied in this work. The first group consists of barriers formed by Ta and inorganic elements N and Si, including Ta-N and Ta-Si-N, named as compound barriers. The second group consists of barriers formed by alloying Ta with another transition metal, to form Ta-Ni, Ta-Cr and Ta-Ti binary alloys.

In this work, the properties of compound barriers, Ta-N and Ta-Si-N with a range of compositions formed by reactive sputtering, are studied. Ta-N and Ta-Si-N are stable on Si substrate at temperatures up to 800 °C and 900 °C respectively. The electrical resistance, however, is high for Ta-Si-N, up to the order of 10^5 μm·cm. The current work also studies the chemical bonding status of the amorphous Ta-N and Ta-Si-N film in an attempt to explain their high thermal stability.

Binary alloys with amorphous structures are studied as a novel group of Cu barriers. The ability to form amorphous phase, annotated as glass formation ability or GFA, is initially predicted based on theoretical understandings. Ta-Ni, Ta-Cr and Ta-Ti films show different GFA. The experimental studies show that Ta-Ni and Ta-Cr form stable amorphous phase on Si substrate up to 800 °C, while Ta-Ti forms crystalline phase at as-deposited state first, transforms to amorphous phase at 600 °C and finally crystallizes at 800 °C. These binary alloy barriers show comparable thermal stability as

Ta-N and better electrical conductivity than Ta-N and Ta-Si-N, making them potential candidates for Cu diffusion barrier.

During Cu barrier performance evaluation, Ta-Si-N shows the best results among all barriers studied. It effectively blocks Cu diffusion into Si substrate after annealing in vacuum at temperatures up to 750 °C, with the formation of Cu_3Si at barrier/Si interface as an indication of barrier failure. In comparison, Ta-N and binary alloy barriers fail at 700 °C. Among all Ta-based binary alloy barriers, interface integrity of Ta-Ni barrier is well maintained at initial failure temperature, while interface integrity is completely lost for Ta-Cr and Ta-Ti barriers. The diffusion profile of Cu in and failure mechanisms of the binary alloy barriers have also been investigated in order to reveal the insights behind the barrier performance of the Ta-Ni barrier. A beneficial effect of oxygen is also observed for both thin films stability and barrier performance. The current study has further advanced the understanding of the formation, stability, and diffusion mechanism of the Cu diffusion barrier. From practical point of view, it is thus proposed that Ta-Ni is the best candidate for advanced barrier application based on the barrier performance and electrical conductivity.

In summary, two groups of Cu diffusion barriers, including compound barriers (Ta-N, Ta-Si-N) and binary alloy barriers (Ta-Ni, Ta-Cr and Ta-Ti), are studied. Ta-based binary amorphous alloy barriers, especially Ta-Ni barrier, show advantages over non-metallic compound barriers Ta-N and Ta-Si-N, in terms of low electrical resistance, high stability with process variation and excellent barrier performance. Guidelines of developing reliable Cu diffusion barrier are drawn base on this study.

Acknowledgements

The success of this work would not have been possible without the support of many individuals.

First and most, I would like to show the deepest appreciation to my thesis advisor, Associate Professor Chen Zhong, for offering the opportunity to further my postgraduate study. It is a great honor to work under him. In the past few years he has shown great support and guidance in many aspects, not only to enhance my technical knowledge, but also to train me as an individual with independent thinking, strong mindset, analytical skills and communication skills. He has provided me many opportunities to collaborate with other universities and industrial companies, which have been precious opportunities to learn from other researchers and to broaden my knowledge. I would also like to express my thanks to my co-supervisor, Associate Professor Liang Meng Heng, for his detailed and patient guidance in my research work, on the training of simulation theories and methods.

I am thankful for Dr Lap Chan and Dr Ng Chee Mang, from Globalfoundries Singapore, for providing the fruitful weekly discussion and technical support in my research.

I would like to thank Professor Xu Shuyan from National Institute of Education (NIE) and Professor Liu Changqing from Loughborough University, UK for providing opportunities to access the facilities in their labs and work with their teams. I am also grateful to my friends and collaborators, Dr Tay Yee Yan and Dr Xu Hui, for their help on thin film characterization. Thanks also go to Dr Pan Jisheng from Institute of Materials Research and Engineering (IMRE) for his support on the thin film

characterization. I would also like to thank many professors in MSE, especially Associate Professor Wong Chee Chong, Associate Professor Gan Chee Lip, Assistant Professor Huang Yizhong, Associate Professor Raju V Ramanujan, Associate Professor Lee Pooi See, for many inspiring discussions.

I am thankful to the staff of the laboratories from MSE, Heryani, Mastura, Guo Jun, Irene, Swee Kuan, Poh Tin, Yong Kwang, and Sandy, for their technical support.

I would like to also acknowledge my fellow students from Micro Electronics lab, Yu Hua, Yang Ying, Pushkar, May, Riko, Kwan Wee, Chan Hoe, Mei Yin, Yeong Huey, Lay Kuan, Xiao Fang, Meng Keong, Derrick, Duen Yang, and all my friends from Special Program of GFS. They have provided me with technical help, discussion, encouragement, and companionship in the last few years. I also thank my colleagues from GFS, who have encouraged me during the last stage of thesis writing.

Last but not least, I would like to say thank you to my family and friends, for their love and great support throughout the long journey of postgraduate study. Their loves always empower me to take any challenge and keep on moving.

Table of Contents

List of Figures

List of Tables

List of Publications

Journal publication

Formation and characterization of magnetron sputtered Ta-Si-N-O thin films
H. Yan, L. Li, F. Y. Ho, M. H. Liang, J. S. Pan, S. Xu, Z. Chen
Thin Solid Films, 2009, Vol. 517 (17), pp. 5207-5211

Copper Diffusion Barrier Performance of Amorphous Ta-Ni Thin Films
H. Yan, Y. Y. Tay, Y. Y. Jiang, N. Yantara, J. S. Pan, M. H. Liang, Z. Chen
Applied Surface Science, 2012, Vol. 258, pp. 3158-3162

Effect of oxygen concentration on the thermal stability of magnetron sputtered amorphous Ta-Ni thin films
H. Yan, R. N. Santoso, Y. Y. Jiang, M. H. Liang, Z. Chen
Thin Solid Films, 2012, Vol. 520, pp. 2356-2361

Conference publication

Molecular dynamics simulation of copper diffusion in titanium based systems
H. Yan, M. H. Liang, Z. Chen, C. M. Ng
International Conference on Materials for Advanced Technologies, 2007, Singapore

Formation and characterization of magnetron sputtered Ta-Si-N-O thin films
H. Yan, L. Li, F. Y. Ho, M. H. Liang, J. S. Pan, S. Xu, Z. Chen
Thin Films 2008, 2008, Singapore

Amorphous Metallic Thin Films as Copper Diffusion Barrier for Advanced Interconnect Applications
H. Yan, Y. Y. Tay, M. H. Liang, Z. Chen, C. M. Ng, J. S. Pan, H. Xu, C. Liu, V. V. Silberschmidt
11th Electronics Packaging Technology Conference, 2009, Singapore

Chapter 1. Introduction

1.1. Background and motivation

In 1947, the world's first semiconductor transistor was born in the Bell Telephone Laboratories. This solid state amplifier soon replaced bulky vacuum tubes in computers and other electronic devices. Since then, with drastic growth of semiconductor industry, the silicon transistors ultimately have changed human society and have become one of the most important inventions of the 20^{th} Century. By integrating billions of silicon transistors into a single chip, a mobile phone today has more computing power than the first supercomputers like ENIAC. The fast development of semiconductor industry has been described by the widely known Moore's law, which predicts that number of components in integrated circuits (IC) doubles every two years (it was revised to every 18 months in 1980s). Valid until now, Moore's law is still guiding the development of semiconductor technology, and driving the research in both academics and industry to achieve a smaller IC with greater speed and higher reliability.

Modern IC manufacturing process consists of two stages: front-end-of-line (FEOL) to form transistors, and back-end-of-line (BEOL) to form interconnection between transistors and passive devices. In BEOL, the interconnect metal and the dielectric layer are two important factors limiting the device performance because of the RC delay. RC delay is determined by the electrical resistance of interconnect metal (R) and the capacitance of the dielectric layer (C). With increasing backend interconnect density, the interconnect resistance and dielectric capacitance becomes higher. In deep sub-micron technology, RC delay from BEOL has overtaken the intrinsic device delay

and become the limiting factor in the circuit speed. Hence both R and C have to be minimized in order to reduce the RC delay. Such requirement has driven the backend interconnect metal changing from Al to Cu to reduce R and the dielectric material changing from SiO_2 to low-κ materials to reduce C. Cu has been used as interconnecting metal since early 2000s, in order to reduce resistance-capacitance (RC) delay. Compared to Al, Cu has shown many advantages such as lower electrical resistivity, better electromigration resistance and superior corrosion resistance. However, Cu is not compatible with Si or dielectrics when in direct contact because Cu is a fast diffuser in Si. It acts as a triple acceptor in Si, generates deep level at 0.24, 0.37 and 0.52 eV above the valence band and acts as recombination center in Si [1]. Diffusion of Cu into p-n junction was observed at 120 ºC through XTEM investigation [2]. Diffusion of Cu into dielectrics will cause degradation of dielectrics, resulting of catastrophic breakdown of the dielectrics [3].

In order to prevent the damage of Cu to Si or dielectrics, a conductive thin film is applied between Cu and adjacent Si or dielectric layers to block the diffusion of Cu. This thin film, known as diffusion barrier, has to meet several requirements [4]: thermal stability with Cu and dielectric layer, ability to prevent Cu diffusion into dielectrics at elevated process temperature, good adhesion with Cu and dielectric layers, low electrical resistance, high mechanical strength and good compatibility with subsequent processes.

The Cu diffusion barriers are generally refractory metal based thin films. They are able to prevent Cu from diffusing into dielectrics even at high temperatures and strong electric fields. The good barrier performance is attributed to the high melting point of refractory metals, as it was empirically observed that the diffusivity is inversely

proportional to the absolute melting point of the host metal [5]. Refractory metals and their nitride such as Ta, Ti, W, Ru, Ta-N, Ti-N, W-N, have been studied as Cu diffusion barrier. However, the elemental barriers such as Ta, Ti, W, Ru generally do not behave satisfactorily because they are usually deposited with polycrystalline structure, in which Cu diffuses fast through grain boundaries [6]. On the other hand, their binary nitride counterparts show better barrier performance. In many practices, a bi-layer of Ta/Ta-N has been serving as Cu diffusion barrier with satisfying performance. It was explained by the "stuffing effect" of nitrogen in the grain boundaries, which blocks the fast diffusion of Cu through the grain boundaries. As reported, a Ta-N barrier fails at 700 ºC [7], and a 1.5 nm thick W-N barrier fails at 600 °C [8].

When the IC feature size is migrated to 32 nm and smaller, some of the above-mentioned requirements become more crucial, especially the electrical resistance. As the metal line width shrinks further, electrical resistance increases. Hence barrier with smaller electrical resistivity are needed to reduce RC delay in BEOL layers. Ta-N generally shows electrical resistivity up to 10^5 μΩ·cm depending on the N concentration [7]. The high resistance of Ta/Ta-N layer becomes a bottleneck in the advanced technology. Therefore, there have been many explorations on replacements of Ta/Ta-N barrier. Some works extended the study to the ternary barrier such as Ti-Si-N and Ta-Si-N. These barriers were reported with superior performance, able to prevent Cu diffusion at temperature as high as 900 °C [9]. This is attributed to their stable amorphous structure. The elimination of grain boundaries in amorphous barriers effectively reduces Cu diffusion rate. However, Ta-Si-N also shows high electrical resistivity, which limits their application as Cu diffusion barrier in industrial application.

Therefore, with the stringent requirement of low electrical resistance to further reduce the RC delay in advanced technology, it is necessary to develop a barrier with both good barrier performance and low electrical resistivity.

1.2. Objectives and scope of work

Motivated by the discussion above, this work is going to explore novel candidates for Cu diffusion barriers. A series of Cu diffusion barriers are studied. Two objectives have been achieved through the studies:

1. To develop a good Cu diffusion barrier that has both good barrier performance and low electrical resistivity.
2. To develop guidelines for thin film diffusion barrier selection through understanding of thin film stability and diffusion barrier mechanisms.

In this work, we propose a new group of Cu diffusion barriers formed from well designed binary amorphous alloy (also known as “metallic glass”). Metallic glass, which is alloy system with amorphous structure, has been widely studied in many fields. In these few years, thin films deposition methods such as physical vapor deposition (PVD) and pulse laser deposition (PLD) are adopted in the study of metallic glass. Due to the fast densification process involved in PVD or PLD, the as-deposited alloy tends to show amorphous structure. These films generally show low electrical resistivity due to their metallic nature. The amorphous structure and low electrical resistivity makes the binary amorphous alloys potential candidates for Cu diffusion barrier. We first designed Ta-based binary films with amorphous phase by forming alloy of Ta and other elements selected from row-4 transition metal (TM), including Ni, Cr, and Ti. The glass forming ability of studied Ta-TM thin films are estimated using

glass forming rules, including size difference rules, and structural difference rules, and verified through experimental investigation. Through the study of Ta-Ni, Ta-Cr, and Ta-Ti, a systematic understating of Ta-TM thin films properties are summarized.

Besides studying the binary alloy barrier performances, it is important to understand the similarities and differences between the binary alloy barriers and other barriers involving the non-metallic elements, such as Ta-N and Ta-Si-N. Most of the works on Ta-N and Ta-Si-N so far focused on the barrier performance of the films. Few addressed on the material properties and the chemical bonding of the films, especially for Ta-Si-N, which has a complicated chemical formation. Thus, this work will also provide an in-depth understanding of the thin films from the perspective of material properties, which explains their high thermal stabilities. Ta-N and Ta-Si-N are named thereafter as compound barriers, as they are compound formed by Ta and non-metallic element N or/and Si.

The Cu diffusion barrier behavior of these two groups are then studied and compared, in terms of barrier failure temperature, stack integrity, and chemical reaction during barrier failure. Based on the understanding obtained from these studies, a guideline for developing stable thin films barriers is drawn. It will provide good reference for future studies in binary amorphous thin films in similar applications.

It should be pointed out that barrier is deposited on dielectric layer instead of Si in industrial application. In the current work, Si is used as the substrate, because formation of Cu_3Si at barrier/Si interface is a good indicator of Cu diffusion through barrier. Typically there is a native oxide on Si surface. The surface morphology of the native oxide is similar to the dielectrics that is in direct contact with Cu diffusion layer. This similarity ensures that the properties of the barrier film formed on Si surface are

comparable with ones formed on dielectric surface. During the barrier performance study, the interaction between Cu and barrier will not be affected by the substrate unless the substrate reacts with barrier before Cu does which is not observed in current work, thus the selection of substrate is less critical. However it should be pointed out that during barrier breakdown, the reaction between barrier and substrate is triggered by Cu diffusion. These phenomena will be different with that of dielectric substrate. Thus the study could be extended to dielectric substrate in future work.

During the study, it is observed that small percent of oxygen has been incorporated in thin films during deposition using a magnetron sputter. Experiments are designed to compare films with different amount of oxygen to understand the effect of oxygen on the thin film properties and barrier performance.

1.3. Contributions of the work

Towards the science and technology development of Cu diffusion barrier films, following contributions are made in this work:

1. It provides a comprehensive study on Ta-N and Ta-Si-N barrier with a wide composition range. It investigates the chemical bonding of Ta-Si-N barrier for the first time, revealing the reason of its high thermal stability and good barrier performance.
2. It proposes amorphous binary alloys as novel barrier candidates through the study of Ta-Ni, Ta-Cr and Ta-Ti barriers. The results suggest that Ta-TM, especially Ta-Ni, is a good barrier comparable with Ta-N barrier. The low electrical resistance makes it a promising candidate to be integrated in the IC fabrication.

3. The effect of oxygen in thin film formation and barrier performance is studied in depth. The scientific understanding provides good reference for other studies.
4. Through a comparison of the two groups (binary alloy and compound) of barriers, a series of material selection criteria of thin film barriers with stable amorphous structure are drawn. It provides a good guideline for material selection for similar application.

1.4. Organization of thesis

The thesis is organized to eight chapters.

Chapter one introduces the background and motivation of this work. It defines the objectives of the work, and also outlines organization of the thesis.

Chapter two provides a review on Cu diffusion barrier studies. It explains the diffusion mechanism of Cu in Si and dielectrics, and the damage caused by Cu diffusion on semiconductor devices. It also reviews previous studies on Cu diffusion barriers, including the elementary barriers, binary barriers, ternary barriers, and alloy barriers. In addition, it also introduces some theoretical understanding on Cu diffusion barriers, including the parameters affecting the barrier performance, the thermodynamics and kinetics theory related to Cu diffusion, and some analytical modeling on Cu diffusion barrier.

Chapter three describes the experimental details and the characterization methods used in this work.

Chapter four studies the formation and properties of Ta-N and Ta-Si-N through reactive sputtering. Ta-N and Ta-Si-N with a wide composition range are deposited on Si substrate. The electrical resistivity and microstructures are examined. The thermal stability of the thin films is analyzed by the microstructure evolution study at elevated temperature. The chemical bondings of the films are studied through XPS to understand the nature of their high thermal stability.

Chapter five studies the deposition of Ta-TM thin films on Si substrate. The glass forming ability of Ta-Ni, Ta-Cr and Ta-Ti system are predicted based on glass forming rules and verified by experiments. The effects of process control on the film compositions and film properties are discussed. The electrical resistivity and microstructures are studied on as-deposited samples. The thermal stabilities of Ta-TM/Si stacks are analyzed after the films are annealed.

Chapter six studies the Cu diffusion barrier performance of Ta, Ta-N, Ta-Si-N, Ta-Ni, Ta-Ti, and Ta-Cr. Diffusion of Cu in these barriers is detected after high temperature annealing in vacuum. The barriers showed different barrier performance and failure mechanisms. Ta-Ni is proposed as a good candidate for replacing Ta-N in IC fabrication, because it has comparable Cu diffusion barrier performance and lower electrical resistance compared to Ta-N does. A material selection guideline for diffusion barrier is also proposed based on the studies.

Chapter seven studies the effect of oxygen on the film properties and barrier performance by comparing Ta-Ni films with different oxygen concentration. Oxygen shows beneficial effect on the thin film stability and barrier performance, but negative effect on electrical conductivity.

Chapter eight summarizes and concludes the current work, and proposes further works for in-depth studies on thin film barriers.

Chapter 2. Literature Review

In this chapter, an in-depth and comprehensive literature review on Cu diffusion barrier studies is provided. In Section 2.1, relevant theories on diffusion in thin film systems are introduced, including a summary of the diffusion phenomena of Cu in microelectronic materials including Si, dielectrics, and low-κ materials, as well as the impacts of Cu diffusion on microelectronics devices. It also introduces the concept of diffusion barrier, the material property requirement and barrier design. In Section 2.2, previous studies on barrier candidate are summarized, including studies on Ta, Ti, Ru, Ta-N, Ti-N, Ta-Si-N, Ti-Si-N, etc. In Section 2.3, these works are summarized and some understanding on the diffusion theory are discussed, such as the effect of microstructure on barrier performance, thermodynamical and kinetic controlling factors in Cu diffusion barrier behavior, and some analytical modeling based on these understandings.

2.1. Cu diffusion in semiconductor materials

In the Back-end-of-Line (BEOL) of Si based microelectronic systems, Cu and dielectrics are the most important materials. While Cu interconnects link the Si devices to form functional circuits, interlayer dielectrics (ILD) provide mechanical support and electrical insulation between Cu lines. However, Cu cannot be in direct contact with Si or dielectric layers such as SiO_2 or low κ materials because Cu reacts with these materials. When Cu is in contact with Si, it reacts with Si at temperature as low as 200 °C, with formation of Cu_3Si or mid gap defect. When Cu is in contact with ILD, it diffuses fast into ILD, causing dielectric degradation, and eventually dielectric

breakdown. This part reviews the diffusion phenomena of Cu in microelectronics systems and the catastrophic impacts of such diffusion.

2.1.1. Diffusion in solid

Diffusion process occurs in all solid, liquid and gas. It is a migration of chemically different atoms in order to obtain lower free energy and reach equilibrium state [11]. Diffusion is under the driving force of chemical gradients, such as the different concentration differences, a negative reaction energy, electric field, thermal energy, strain gradient, or combination of these factors. [11]

The theoretical understandings of diffusion are summarized by Fick's first law and second law [12]. Fick's first law states that diffusion flux is proportional to the concentration gradients in ideal solution, where the gradient of chemical potential is controlled by the concentration gradient. The one-dimensional description of Fick's first law is $J = D\frac{dC}{dx}$, where D refers to the diffusion coefficient, J refers to the atomic flux per second per unit area, x refers to the distance, and C refers to the atomic concentration, and. As a derivation from Fick's first law, Fick's second law predicts the concentration field change with time during a diffusion process: $dC/dt = D\frac{d^2C}{dx^2}$, where t is the time, and other parameters are the same as those in Fick's first law.

As can be seen in Fick's law, the diffusion rate depends on the driving force ($\frac{dC}{dx}$) and the diffusion coefficient (D). As a thermal activated process, the diffusion coefficient D depends on temperature and follows Arrhenius relationship:

$$D = D_0 \exp(-Q/kT) \tag{2.1}$$

Table 2-1 Activation energy of Cu self-diffusion through different diffusion channels

Diffusion mechanism	Ea (eV)	Reference
Lattice diffusion	1.4	[13]
Grain boundary diffusion	0.4-0.5	[14]
Grain boundaries to bulk	0.62	[15]
Defects to bulk	>0.62	[16]
Surface	0.28	[17]

where D_0 is pre-exponential constant, T is the temperature in Kelvin, Q is activation energy of diffusion, and k is Boltzmann's constant. Generally, Q and D_0 are dependent on the material properties such as atomic bonding, microstructure, presence of defects, etc. Each diffusion mechanism has its own activation energy. As a result of activation energy difference, diffusion rates vary with the diffusion mechanism. In reality, when multiple diffusion mechanisms exist, diffusion is dominated by the mechanism with the lowest activation energy. A good example is Cu electromigration which is widely observed in BEOL of microelectronics. During Cu electromigration, Cu migration is mostly observed at Cu surface, where it requires lowest activation energy for Cu self-diffusion (Table 2-1).

In the case of inter-diffusion of two materials, the diffusion rate is found to be dependent on two factors, the melting point (MP) of the host material and the dominant diffusion mechanism. There is an empirical relationship that diffusion rate of the diffusing material is inversely proportional to the absolute melting temperature of the host material. It can be described by $D \propto AT_m$, where T_m is the melting point of the host material, and A is a proportionality constant which is related to the diffusion mechanism [18]. The physical meaning of constant A was reported by Gjostein Na

[21]: it depends on factors such as lattice structure and material type. The lowest A and slowest diffusion rate is resulted from Lattice diffusion with the exchange of vacancy-atom. Diffusion through defects such as dissociated dislocation exhibits intermediate rates. The largest A with fastest diffusion rate is usually observed in high-angle grain boundary diffusion, which results from large misfit between two grains [18]. As a result, diffusion in single crystalline materials, in which the only available diffusion mechanism is lattice diffusion, is the most difficult compared to that in other structures [12]. Same as observed in case of self diffusion, when multiple diffusion paths exist, the diffusion path which possesses lowest activation energy dominates. In most cases diffusion in bulk materials at room temperature is dominated by grain boundaries diffusion and diffusion through extended defects because of the low activation energy.

2.1.2. Cu in Si

Theoretically, diffusion of solid in single crystalline materials usually shows very slow diffusion rate because of the high activation energy needed for vacancy formation and substitutional diffusion. Thus diffusion in epitaxial Si is generally expected to be slow because of the elimination of defects and grain boundaries in the single crystalline structure. Surprisingly, it was experimentally observed that Cu diffuses into Si fast even at room temperature.

Effective diffusivity of copper in Si was described by Hall and Recette [19] in 1964 with formula $D = 4.7 \times 10^3 \times \exp(-0.43\ eV/k_BT)\ cm^2\ s^{-1}$ through radiotracer measurement. However, it was noticed that the effective diffusivity of Cu in Si was a result of two driving forces, the intrinsic diffusion of Cu in Si, and the effect of Cu^+ trapping by immobile acceptors B^- in the p-type Si used in this work. At a given

moment, only a certain percent of Cu concentration is mobile, and the rest is temporally trapped because of the pairing of Cu^+ and B^-. Later on, a few studies on calculation of intrinsic diffusion coefficient of Cu in Si were reported, most of which were based on the transient ion drift experiments [20-21]. The intrinsic diffusion activation energy was reported to be as low as 0.18eV [22]. This low activation energy was attributed to the relatively ionic radius of Cu in Si and the weak covalent interactions between Cu and crystal lattices. While the slow diffusers are substitutionally dissolved in the intrinsic point defects such as vacancies or self-interstitials, Cu is predominantly interstitially dissolved and move by jumping in between interstitial positions, so diffusion is still possible without any intrinsic point defects [23]. As a result, Cu becomes a "fast" diffuser in silicon and it exhibits diffusion coefficient of many orders of magnitude higher than that of its self-diffusion [22]. The exact diffusion rate is determined by temperature and the dopant concentration. It increases with temperature, and decreases with boron concentration. As estimation, Cu can diffuse through a 625 μm thick non-doped wafer in 3 hrs at room temperature, or through a doped wafer (10^{15} cm^{-3}) in about 15 hours at the same temperature [24].

At supersaturated state, Cu in Si precipitates by Cu silicide formation. It was also reported that the Cu silicide formation was affected by the dopant state of the silicon. It was observed that Cu precipitates are electrically amphoteric. When the Fermi level crosses their electro-neutrality level at about E_c-0.2eV,their charge state change from positive to negative. Thus in p-type Si the Cu precipitate nuclei is positively charged and the repulsive electrostatic force in between Cu_i^+ and Cu precipitate nuclei depress Cu precipitation in the bulk. On the other hand, Cu precipitate in n-type Si is negatively charged or neutral, thus the electrostatic force between Cu precipitate

nuclei and Cu_i^+ is either attractive or neutral, and copper can easily precipitate in the bulk Si [25-26].

Because of the fast diffusion and formation of Cu silicide precipitate, Cu could cause detrimental impact on the electrical performance of Si devices. Diffusion of Cu into p-n junction was observed at 120 ºC through XTEM investigation. The electrical breakdown occurs after annealed at 200 °C, with diode leakage current increasing for several orders of magnitude [2] . The electrical breakdown was because of the formation of Cu_3Si spike at Cu-Si interface, most likely starting from the n^+ region as shown by the extensive Cu precipitation at the n^+ area [3]. Besides that, several Cu related defect reaction was reported, including interstitial defect with shallow acceptors, Cu-transition metal pairs, Cu-irradiation induced defect complexes, etc. [27].

2.1.3. Cu in dielectrics

Studies on Cu/dielectrics systems have shown that Cu could be transported into dielectrics layers under both thermal stress and Cu ion drift. These studies were usually carried out under bias-temperature-stress test (BTS). In BTS test, positive potential is applied to the Cu electrodes to evaluate the behavior of Cu/dielectrics interface under thermal and electrical stress.

Both electrical and physical techniques are used for diffusion characterization, the former one including shift of capacitance-voltage (CV) flat band curve and junction leakage, and the later one including depth profiling spectroscopy such as secondary ion mass spectroscopy (SIMS), Rutherford back-scattering (RBS), and Auger electron spectroscopy (AES).

Experimental works have shown that electric field generally accelerates the Cu transport into dielectrics. The Cu transport through silicon dioxide was observed at 350 °C without electric field [28], and the activation energy was extracted to be 1.82 eV. With the presence of an applied electric field, this temperature was measured to be 100 to 150 °C [29]. The mechanism of Cu transport in dielectric is yet to be clarified. Wills and Lang reported that the Cu oxidation could be the reason of the fast transportation of Cu into dielectrics. They showed that only the Cu deliberated oxidized in ambient gases is diffused to SiO_2 dielectrics for BTS test with temperature lower than 450 ºC and electric fields smaller than 1.0 MV/cm, while no diffusion of metallic Cu under such bias conditions was observed [30].

Cu diffusion in dielectrics causes dielectric degradation and catastrophic damage of chips. A three stage degradation mechanism was proposed by Raghavan and coworkers in 1995 [29]. Cu ions are trapped in dielectric, which in turn increases the electric field across the oxide and results in high leakage current and/or dielectric breakdown.

When low dielectric constant (low- κ) material is widely used in semiconductor industry, the interaction of Cu and low- κ dielectric has also been widely discussed. A few researches were carried out to evaluate Cu diffusion into low-κ materials [31-32]. Most low-κ dielectric materials are developed based on SSQ, Silica, organic polymers or amorphous carbon. In order to further reduce the dielectric constant, pores are introduced into these materials. However, the porous structure reduces the mechanical strength and stability, which causes interface instability. Therefore, interfacial adhesion becomes a critical issue in Cu/low- κ interconnects. A thin film delamination or cracking is often observed at interfaces.

2.1.4. Cu diffusion barriers

2.1.4.1. Introduction of diffusion barriers in solid thin film systems

In metallic thin film systems, there are situations in which the interfaces between two adjacent layers are not stable, e.g. high chemical affinity between the two materials, high solubility of atoms in each other, or high diffusion rate of one material in another, etc. As discovered by DuMond and Youtz, inter-diffusion in thin film was associated with a lower diffusion activation energy than that in bulk materials [33]. In Nicolet attributed it to the high grain boundaries density and other defects [34]. Barrier layers are introduced in such systems, serving as intermediate layer to separate two thin films with favorable chemical interactions. As discussed in the fundamental diffusion theory in section 2.1.1, the diffusion rates in solid systems are determined by a few factors, such as the materials, chemical reaction, diffusion mechanism, extended defects, and microstructure. Thus barriers are designed from different approaches to retard Cu diffusion.

The barriers are designed based on two general approaches: 1) to form a secondary interaction path with a lower energy barrier between barrier layer and metallic layer. This will promote the secondary interaction and suppress the inter-diffusion; 2) to stop the atoms passing through barrier layer by eliminating the short diffusion path, mostly grain boundary, in the barrier layer. Practically, diffusion barriers are catalogued into three types, including sacrificial barriers, stuffed barriers, and amorphous diffusion barriers as shown in Fig. 2-1 [35]. In sacrificial barrier, the intermediate layer will react with one or both of the materials. The barrier remains effective until it is completely consumed. Therefore, reaction rates among the barrier, layer A and layer B must be slow enough to maintain the effectiveness of barrier. Sacrificial barriers thus

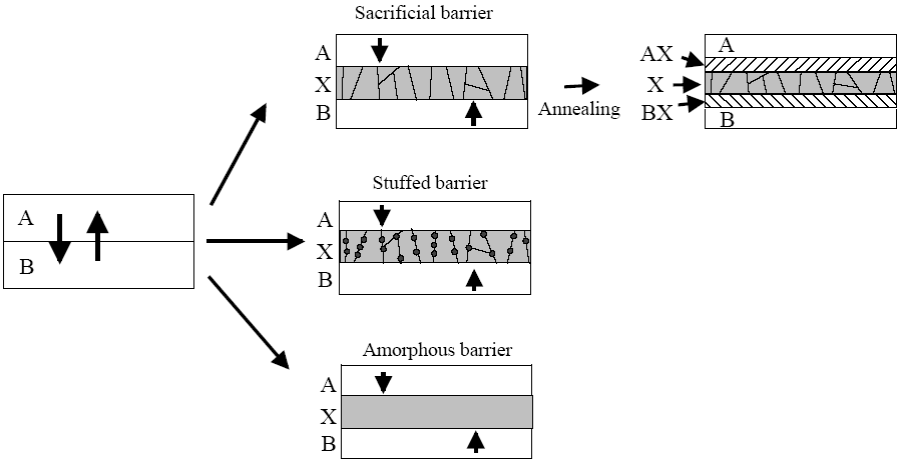

Fig. 2-1 Schematic illustration of the three classes of diffusion barriers [35].

shows limited lifetime. The permanent protection requires the barrier to be thermodynamically stable with the layers A and B. Furthermore, the diffusion of A and B across X through short-circuit paths needs to be eliminated. Two methods can be used, either to eliminate the short circuit path, or to fill these short path with small atoms or molecules.

Stuffed barrier was developed to fill the short paths. With the purposely introduced small atoms, the diffusion path of A or B through short-circuit path is effectively blocked, thus reducing the diffusion rate.

Another method to eliminate the short-circuit path is to make the structure of the barrier amorphous, which reduce the easy paths (i.e. grain boundaries). Practically, four types of microstructure could be potentially formed during thin films deposition, single crystalline, polycrystalline (sometimes bamboo structure in thin films), nanocrystalline, or amorphous (Fig. 2-2). As to the diffusion rate, it is usually accepted

that the diffusion in single crystalline is the slowest because it relied solely on lattice diffusion. The lack of extended defect in amorphous or nanocrystalline structure eliminates fast diffusion paths. But because of the difficulty of processing, single crystalline was not considered as practical barrier structure. However, it is worth considering whether a single crystalline is more efficient than amorphous barrier in case of short path elimination. As a contrast, polycrystalline film does not usually form effective diffusion barrier because of the large volume of free space at the grain boundaries and triple point. As a special case of polycrystalline film, bamboo (or columnar) structure is often observed in thin film systems when the crystal size is larger than thin film thickness. Experiments showed that, in as-deposited amorphous barrier, columnar structure could be formed after high temperature annealing as a result of grain growth driven by thermal energy. When grain size is larger than film thickness, columnar structure forms [36]. This structure should be avoided since it provides a fast diffusion path. Ou et al. [37] examined the barrier performance of columnar Ti and amorphous Ti layer. In the purposely formed columnar Ti, Cu diffusion was observed at temperature below 400 ºC while amorphous Ti fails after anneal at 600 ºC. Obviously, the elimination of grain boundary in amorphous materials helps achieving high activation energy and suppresses diffusion. Therefore, amorphous structure or stable nano-structure should be beneficial for barrier materials [38]. However, these amorphous layers are usually metastable, and will crystallize with enough thermal energy input. Thus, the crystallization temperatures of the amorphous films are very important.

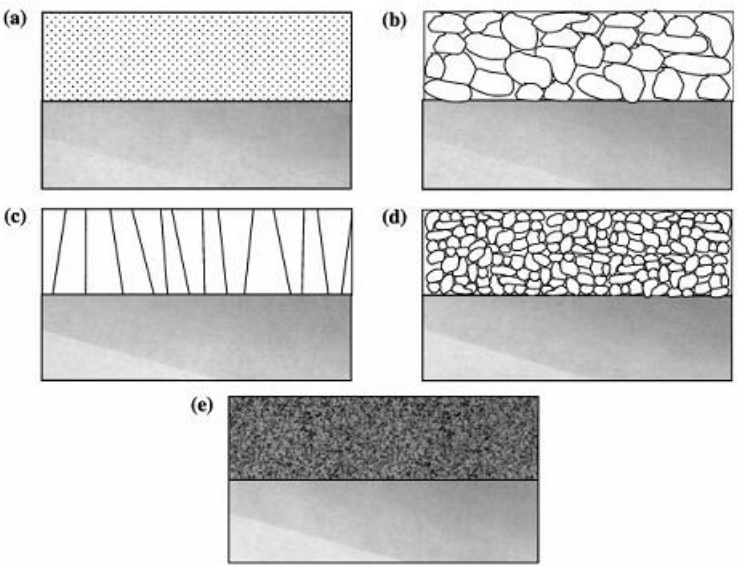

Fig. 2-2 Schematics of different microstructure of barrier (a) single crystalline; (b) polycrystalline; (c) columnar polycrystalline; (d) nanocrystalline; (e) amorphous [38]

2.1.4.2. Introduction and requirement of Cu diffusion barrier

In many fields including semiconductor devices, the diffusion barrier has been widely used to suppress inter-diffusion in thin films [34]. Cu diffusion barrier layer was introduced as an intermediate layer to separate contact between Cu and adjacent dielectric layer. Ideally, this barrier layer should not maintain their desired chemical, electrical and mechanical physical properties during processing and device application. The schematic of Cu barrier in IC device fabrication is shown in Fig. 2-3, where Cu diffusion barrier is deposited between dielectric and Cu seed layer, followed by electroplating of Cu.

Barriers can be deposited on Si and dielectrics through various methods, such as physical-vapor deposition (PVD), chemical-vapor deposition (CVD), and atomic-layer deposition (ALD), etc. PVD process is by far the most widely adopted method in both

Fig. 2-3 Schematic illustration of Cu diffusion barrier

the academia and the industry. In recent years there have been emerging studies on ALD deposited barriers, mainly because of the precise thickness control of ALD which benefits the more advanced technologies. More details will be discussed in section 2.2.4.

In order to become a reliable diffusion barrier, the materials are required to possess a set of properties, as summarized by Kaloyeros in 2000 [38], including high thermal and structural stabilities, good adhesion to adjacent layers, microstructure which can minimize grain boundaries diffusion, low electrical resistances, and compatibility in IC fabrication.

As the semiconductor feature size and barrier thickness reduce further, some of these requirements become more critical. In ultrathin barrier, it tends to form columnar structure by crystallization at high temperature; therefore, high thermal stability is more emphasized in recent research. Adhesion, texture and roughness control is also very important since electron scattering is strongly affected by interface roughness.

With reduced Cu width, contribution of barrier resistance on the overall resistance becomes more significant, thus requirement of electrical conductivities of the barrier layer is becoming more important.

2.2. Cu diffusion barrier candidates

The diffusion processes has strong dependence on the melting point of the host lattice. Therefore it is important desirable to select the barrier material with a high melting point. According to this rule, refractory metallic systems with high melting points and chemical inertness usually behave as reliable diffusion barrier in Cu-based metallization. A few groups of refractory transition metals and their binary or ternary compounds have been proposed as Cu diffusion barrier [39]. These barriers have been classified into seven groups, including refractory metals, refractory metallic alloys, refractory metal-silicon alloys or compounds, refractory metal-nitrogen, metal-oxygen, metal-carbon, metal-boron compounds, silicon-nitrogen and silicon-carbon compounds, Amorphous ternary barriers, and carbon-based alloys and compounds. The barriers proposed so far include refractory metals such as Ta, Ti, W, Ru, Nb, Cr and Mo. These barriers usually consist of single element or alloy metal, and/or small non-metallic elements, like O, N, Si, and C, stuffed at the grain boundary of metal grains. Widely studied candidates include Ta, Ti, W, Ru, Ta-N, Ti-N, W_2N, Ta-Si-N, Ti-Si-N, while other combination like TaGeN [40] has also been investigated because Ge has been applied in strain Si technology. Barriers consisting of two layers are also widely studied [41-43], because of the overall better properties which single layer barriers do not have.

Success of binary barrier with non-metallic elements is attributed of the “stuffing” effect caused by the small non-metallic elements which help blocking grain boundary

diffusion [44-45]. Compared to the binary counterparts, ternary compounds generally show better barrier properties but result in higher resistivity [38]. The success of ternary barrier is attributed to the stable amorphous phase because of multi-phase structure. Isolated nano-particles embedded in amorphous phase were found in as-deposited ternary Ti-Si-N barrier [46]. Nano-particles make the crystallization more difficult, thus increase thermal stability, while amorphous matrix eliminates grain boundary diffusion, thus enhances barrier performance.

In this section, studies on various barrier candidates are summarized. The materials properties, microstructures, barrier behaviors, failure mechanisms and deposition methods will be reviewed for each candidate.

2.2.1. Elemental barriers and binary barriers

Due to the performance limitation, elemental metals such as Ti, Ta, W, and Ru are not usually used alone as the Cu diffusion barrier. A bi-layer barrier is widely used combining refractory metals and their binary compounds such as Ti-N, Ta-N, WN, RuN, etc. Therefore the elemental barrier and their binary counterparts will be discussed together.

2.2.1.1. Ti and Ti-N barriers

In Al metallization, Ti-N/Ti barrier was used as diffusion barrier layer and adhesion layer. The availability of gaseous precursor assures the use of CVD process, which provides a relatively good conformity and low roughness compared to PVD process. Thus it was expected that Ti-N/Ti could be extended to Cu metallization. However, in Cu metallization, it is shown that Ti/Ti-N cannot provide a good Cu diffusion barrier with a thickness under 20 nm [47]. Ti forms intermetallic compounds Cu_3Ti and

Cu_4Ti with Cu at 350 °C [47]; moreover, Ti-N fails through grain boundary diffusion at temperature between 450 °C and 600 °C, because the columnar structure is formed at higher temperature [48]. In columnar structure, grain boundaries extend through the thickness of the Ti-N film. They will form short-circuit paths, which result in fast Cu diffusion, and thus cause the device failure. In Al metallization, it was observed that the diffusion of oxygen in barrier grain boundaries can block Al diffusion inside Ti-N by forming Al oxide; however, this so-called "oxygen stuffing" mechanism does not apply for Cu metallization, because there is a lack of self-limited oxide formed by Cu [38]. Instead, it was observed that Cu oxide formed in atmosphere accelerates diffusion of Cu^+ ion into dielectric layer under electrical stress [30].

It was expected that by destroying the columnar structure, the barrier property of Ti-N can be improved. Effort was made to deposite multiple barrier layers to eliminate columnar structure. However, amorphorization process usually introduces extra steps [49-50]. Some works showed that by using metalorganic CVD (MOCVD) techniques, amorphous Ti-N structure could be obtained. However, MOCVD process usually involves contamination such as O, C or H, resulting in a porous and low-density Ti-N microstructure. Although some work managed to deposite the amorphous Ti-N using techniques like plasma-assisted MOCVD and post-deposition annealing treatments, the attempts did not yield required Ti-N barrier performance either.

2.2.1.2. Ta and Ta-N barriers

Ta/Ta-N are applied as Cu diffusion barrier ever since Cu substituted Al in the early 21st century. The bi-layer structure provides relatively high electrical conductivity, good adhesion and high thermal stability. Recent advances in PVD technology have extended the applicability of Ta/Ta-N barrier down to the 90/65 nm nodes [41].

However, the Cu-seed/Ta/Ta-N tri-layer configuration will encounter scaling difficulties at more advanced technology node.

Compared to Ti, Ta is apparent to be a more effective barrier candidate. It has a melting point as high as 3020 ºC, compared to 1670 °C of Ti. According to the empirical relationship reported by Gjostin, diffusion of Cu in Ta is expected to show high activation energy for both lattice diffusion and grain boundary diffusion [34]. Ta and Cu do not form intermetallic compounds, therefore ensures a stable Ta/Cu surface with good adhesion. A BTS study investigated the barrier performance of Ta and Ti-N with capacitor structure of Cu/30 nm thick barrier/100 nm SiO_2/Al [51]. It was shown the capacitor with Ta barrier has longer mean time to failure (MTTF) compared to the one with Ti-N barrier. The MTTF of device with Ta barrier further increased about two orders of magnitude after annealed. The Cu/Ta/Si structure fails at 550 °C with formation of Ta_3Si, and it is stable within the thermal processing window and operation temperature [47, 52]. It should be noted that different failure temperature might be resolved with the change of deposition method, film thickness, and characterization method. A more detailed failure mechanism of Cu/Ta/Si was suggested by Lorila et al. [52]: Cu_3Si phase is formed first after Cu diffuses through Ta barrier, and followed by formation of tantalum silicides. At temperatures below the formation temperature required for $TaSi_2$, a significant Cu diffusion already started. The key to prevent the vertical structure breakdown is to hinder the Cu diffusion. However, it is well known that as elemental metal, Ta tends to crystallize at elevated temperature. The large density of grain boundary in polycrystalline or bamboo-structure leads to diffusion of copper through Ta. There has been Effort to increase the crystallization temperature of Ta, including doping using small atoms such as O, N [53] or oxide (CeO_2) [54]. While the doping with O and N in Ta barrier

did not show better performance than Ta-N barrier, the CeO_2 doping significantly increased the Cu diffusion temperature from 550 ºC to 800 ºC. However, Ta-N results in high resistance, which is a serious concern in advanced technology node.

In spite of the imperfect barrier performance when used alone, Ta is a good adhesion layer with Cu [55]. It also promotes the preferred (111) orientation for Cu seed layer deposition [4], thus could be used as adhesion layer between the barrier layer and Cu.

Since Ta shows superior barrier performance compared to Ti, it was reasonable to expect its nitride could behave as a good barrier candidate. The early study from Stavrev's group showed that a sputtered 50 nm Ta-N films was able to prevent copper reaction with silicon substrate for temperature up to 560 ºC for 1 hr, compared to a Ta barrier which prevented interaction between Cu and Ta up to 450 ºC for 5 h [56]. In another study by Oku et al., a Ta-N layer of 8 nm deposited by reactive sputtering showed the ability to prevent intermixing of Cu and Si at 700 ºC for 30 min. The as-deposited Ta-N showed polycrystalline phase with disordered grain boundaries [7]. A more comprehensive study was reported by Wang et al. [57]. A Cu/barrier/P(+)-n junction diode structure was built to evaluate the barrier behavior of Ta and Ta-N. The Ta barrier of 5, 10, and 25 nm thicknesses were able to sustain a 30 min thermal annealing at temperatures up to 450, 500, and 550 ºC, respectively. On the other hand, For the Cu/Ta-N/p(+)-n junction diodes with the Ta-N barrier of 5, 10, and 25 nm thicknesses, thermal stability was able to reach 500, 600, and 700 ºC, respectively. They also observed that the failure of Ta and Ta-N barriers was due to Cu diffusion through the barrier via local defects rather than Ta silicidation. Their work did not mention the exact microstructure and phase of the Ta-N barrier. The phase diagram of Ta-N indicated that Ta-N had several stable structures at different N concentrations.

Min et al. showed that the reactively sputtered 50 nm Ta_2N and TaN barrier failed at 700 °C and 750 °C annealing [58]. Chen and Lee observed that Ta-N with different phase and stoichiometry can be deposited by reactive sputtering with change of N_2 flow rate [59]. Yang et al. further studied the barrier behavior of the reactive sputtered Ta-N with different N_2 flow, and reported that N_2 flow ratio had to be limited below 10 % to avoid high resistance. Ta-N (3-5 %) with amorphous Ta(N) phase showed best barrier performance [60]. But this work did not present the atomic concentration of the barriers, thus no correlation between the N_2 flow ratio and the Ta-N film composition could be concluded. Later Hecker et al. investigated the barrier performances of α-Ta, Ta(N) with 20 at% and stoichiometric TaN, among which TaN showed best result, followed by Ta(N). They concluded that the performance increased with N content [61]. The failure mechanisms of Ta-N with different composition range were found different in these studies. Ta(N) fails by the reaction between Ta and Si. It was believed that improvement is due to the N segregating at the existing grain boundary, or the "stuffing" of grain boundary [62]. The failure of Ta_2N was initiated by reaction between Ta_2N and Si substrate [58, 63]. TaN fails by crystallization of TaN at elevated temperature and diffusion of Cu through TaN grains [63-64].

In most of the mentioned works, the failure of Ta-N was due to Cu diffusion through barrier and thereafter the reaction between Cu and barrier. Lin and Lee measured the diffusion of Cu in Ta-N barrier, showing that grain boundary diffusion dominates in the failure of Ta-N barrier [64]. Thus the structure of Ta-N plays an important role in the barrier performance. By tuning the Ta-N structure barrier behavior could be improved. Specifically, sputtered Ta-N showed superior performance than CVD deposited Ta-N [65]. This implies that the excess N in the PVD TaN*x* might have been located interstitially, and at the TaN*x* matrix grain boundaries. As such, it might

have “stuffed” the grain boundaries and acted as a good barrier against diffusion along such pathways. Some studies targeted at forming amorphous Ta-N structure. Chang et al. showed that by increasing the N_2 flow ratio to 15 %, amorphous Ta-N could be obtained, with the increase of electrical resistance [66]. In another work, a two layered Ta_2N structure (20 nm $Ta_{67}N_{33}$/20 nm $Ta_{62}N_{38}$) shows better barrier performance than a single layer Ta_2N (40 nm $Ta_{67}N_{33}$) with a degradation temperature increased by 100 °C. The enhancement was greatly attributed to the breaking of grain boundary path in double layered structure [67].

With the understanding of the performance of Ta and Ta-N, Ta/Ta-N bi-layer is widely accepted by industry [68]. It was known that Cu on Ta-N layer exhibits voiding even at 400 °C [69], thus a Ta adhesion layer helps solving this issue. A two layer structure further improves the barrier property [70]. Therefore, in spite of the two process steps needed, it is accepted as the best solution by the semiconductor industry so far.

The most common deposition method for Ta is PVD, due to the ease of process. Inorganic CVD using halide source precursors, such as $TaCl_5$, TaF_5, $TaBr_5$, and MOCVD process was also investigated by some group [71]. Some of these works showed good step coverage, low contamination and low resistance. However the potential corrosion caused by halide precursor and contamination from MOCVD constrained the application of CVD in industry application. Same as Ta deposition, deposition of Ta-N is mostly through reactive PVD or CVD process. Each has their pros and cons. While Ta-N process is more widely used because of its ease of application and better film integrity, CVD process is able to deposite films with better step coverage which is critical in the advanced technology [71-72]. Besides PVD and

CVD process, atomic layer deposition (ALD) process was also studied in depth in recent years [73-76], mainly due to the precise thickness control and excellent step coverage. However, due to the constraint of precursor requirement and potential poisoning of devices, ALD process is mainly used in research field.

2.2.1.3. Ru and Ru based barrier

In semiconductor industry, a thin Cu layer is usually sputtered on Ta/Ta-N barrier in order for the subsequent Cu electroplating. Ruthenium as a barrier has attracted much attention in recent years because Ru itself can act as seed layer for Cu, with the capability of direct electroplating of Cu on Ru barrier. Chyan et al. demonstrated the electrochemical deposition Cu on Ru substrate, in which Cu nucleated and grew on Ru substrate, with strong adhesion and stable interface [77]. It was thus expected that by using Ru as Cu diffusion barrier, the Cu seed layer deposition process could be eliminated. However, Ru was not a satisfying barrier. A 20 nm PVD Ru allowed Cu diffusion into Si layer at 450 °C and above [78], and a 5 nm PVD Ru failed with ruthenium silicide interlayer formation at Ru/Si interface after annealing at 350 °C [79]. It was expected that by introducing N into Ru, the barrier performance could be improved. Study showed that by sputtering Ru in N_2 atmosphere, N could be introduced in Ru. But it was observed that there was no N-Ru bonding formation; instead, an out diffusion of N with time was observed after annealing [80]. As a result, unlike other refractory metal such as Ta or Ti, Ru barrier performance cannot be enhanced by N stuffing. On the other hand, addition of P in Ru showed improved barrier performance than Ru barrier [81]. Yet it did not provide better performance than Ta-N barrier.

Inspired by Ta-N/Ta and Ti-N/Ti stack concept, barrier properties of bi-layers like Ru/Ta-N, Ru/Ti-N, and Ru/Ta are also investigated. Kim et al. studied multi-layered barriers using three different thin metal layers (Ru, Cr and Zr) between two 5 nm Ti-N films [82]. Their results showed that, compared to Cr and Zr, Ru has little effect on improving Ti-N barriers performance. In another work, a 100 nm Ru_{1-x} $(Ti\text{-}N)_x$ mixed layer showed stable amorphous structure at above 750 °C, which is higher than Ru and Ti-N [83]. Cu/Ru/Ta/Si and Cu/Ru/Ta-N/Si both showed improved thermal stability than Cu/Ru/Si, while Ru/Ta-N behaved better than Ru/Ta [84]. A recent research showed that Cu/Ru/Ta-N/Si stack fails at 750 °C compared to that of Cu/Ru/Si structure at 450 °C. The failure is of same mechanism as Cu/Ta/Si system with the formation of $TaSi_2$ [85]. The higher stability of Ru/Ta-N barrier is mainly attributed to the amorphous nature of Ta-N.

As discussed before, though it is an excellent seed layer of Cu electroplating, the barrier performance of Ru remains questionable. The Ru/Ta-N bilayer provides a reliable solution, but the bi-layer structure increases the process complexity. More study is needed to improve the Ru barrier performance in order to form a promising barrier.

2.2.2. Ternary barriers

As discussed above for Ta-N barrier, the failure of Ta-N is due to the crystallization at elevated temperature followed by the diffusion of Cu through barrier grain boundaries into Si. In order to improve the barrier effectiveness, microstructure control of barriers need to be emphasized, for which a stable amorphous barrier is preferred as discussed in section 2.1.4. Ternary barriers are proposed in order to fulfill the objective. Ternary barriers usually involves three elements formed by refractory metals (Ti, Ta, W, etc)

and small atoms (Si, B, O，N, etc.) [86]. Most studied candidates include one refractory metal, including Ta-Si-N [9, 87-88], Ti-Si-N [89-91], W-B-N [92], Ta-B-N [93], Ta-Ge-N [94] etc. A few studies investigated ternary barriers with two refractory metals, such as Ta-W-N [95], Co-W-P [96], etc. Understanding was extracted from the extensive studies of Ti-Si-N and Ta-Si-N [97-100]. It was noted that the failure mechanism varied with the barrier deposition method and composition.

The introduction of Si into Ti-N/Ta-N has been discussed since 1980s. As expected, the ternary barriers showed more stable amorphous structure compared to their binary counterparts. The failure temperature of Ti-Si-N barrier was reported ranging from 650 °C to 850 °C, depending on the barrier thickness [89]. The Cu diffusion did not occur until the crystallization of barriers. The failure of Ti-Si-N was due to the reaction between Cu and barrier, with the formation of Cu-N and Cu-Ti compounds [91]. One study reported that Ti-Si-N with 46 % N showed best barrier performance [99].

For Ta-Si-N, the crystallization temperature can be up to 1100 °C, much higher than Ta (600 °C) and Ta-N (750 °C) [38]. A BTS study reported that a capacitor of Ta-Si-N/ Cu /Ta-Si-N-oxide-silicon remained functioning after stressed at 300 °C with electric fields higher than 1 MV/cm for more than 80 hour [87]. In our work, we also observed that by purposely introducing O into the Ta-Si-N films, thermal stability of the amorphous system would be further increased, which is due to the formation of $TaSiO_x$ [101].

Other amorphous or quasi-amorphous M-Si-N barriers also showed high thermal stability and good Cu diffusion retarding ability [86, 102] . Reid et al. reported that the barrier performance of M-Si-N (M = Co, Ta, W) was dependent on both barrier

formation method and composition. With optimized atomic ratio, W-Si-N and Ta-Si-N achieved failure temperatures of 900 ºC, while the highest failure temperature achieved for Co-Si-N was at 800 ºC [102]. For W-Si-N and Co-Si-N, the crystallization was driven by the out-diffusion of N which was not observed for Ta-Si-N. It is also reported that barrier deposition in atmosphere will result in better barrier performance [4] . It might be due to the O stuffing inside barrier layer. In another study on Me-Si-N (Me = Ti, Ta, Re, W), W-Si-N behaved as the most promising barrier candidates with the consideration of barrier behavior and electrical properties [86]. Different performances were noted in these studies, which were probably due to the effect of composition, thus systematic studies are needed.

Failure of ternary barrier is usually attributed to the crystallization at high temperature which induces fast grain boundary formation, Cu diffusion into substrate and Cu silicide formation [103]. But it was discovered in other research that the failure mechanism may also depend on nitrogen concentration. For Ta-Si-N barrier, it was reported that with N content more than 25 at%, Cu diffused into substrate without significant crystallization, while with N content less than 25 at%, Cu diffusion was not observed until the crystallization of barrier [100].

The high effectiveness of ternary barrier is largely attributed to its stable amorphous structure, based on the reports that for ternary barriers the Cu diffusion mostly occurs after crystallization of the amorphous barriers. The high stability of the amorphous structure can be illustrated by their ternary phase diagram. Ramberg provided a collection of phase diagrams for some popular ternary system [104]. The phase diagrams show that ternary barriers are a mixture of metallic and non-metallic compounds, and the nucleation and crystal growth requires extensive atoms migration

and phase change. It results in high crystallization activation energy, e.g. high thermal stability. The stuffing effect was also suggested with the incorporation of small atoms such as Si, N and B [24] . However based on the experimental observation and phase diagram, stuffing effect should be attributed more to the compounds with high crystallization temperature, such as Si_3N_4 [105].

In addition to TM-Si-N barriers, ternary systems such as TM-B-N, TM-Ge-N were also studied by some researchers. Their barrier performances are similar as those of TM-Si-N barrier, due to the same concept of formation (TM-semiconductor-N) [92-94].

Although the high breakdown temperature makes ternary family a good barrier, ternary compounds usually have much higher electrical resistance, compared to the binary compounds. For Ti-Si-N barrier, resistivity can be as high as 800-1200 μΩ·cm. Higher surface roughness was also reported. Olowolafe et al. [106] reported that barrier stability and resistance are dependent on composition. Higher Si-Ta ratio results in higher resistivity. The increase of resistivity with nitrogen concentration was reported recently [107]. The high resistivity of ternary compounds makes them not preferred Cu diffusion barrier in industrial application because they will increase RC delay.

2.2.3. Binary alloys

Cu diffusion barriers are usually composed of both refractory metallic elements (Ta, Ti, etc), and non-metallic elements (Si, N, B, etc). Non-metallic atoms contribute to the stability and effectiveness of barrier. The drawback is the reduction of electrical conductance as a result of ionic bonding. As a contrast, alloys consisting of two

transition metals showed low resistivity because of the metallic nature. With stable amorphous structure, it could be good choice for barrier candidates with low electrical resistivity and good barrier performance.

Amorphous alloys are usually alloys containing atoms of significantly different sizes, which results in small free volume. In order to form amorphous alloy (also called metallic glass), atom sizes have to be significantly different from each another, usually over 12 %. There have been a few studies on alloy barriers. Wang et al. [108] summarized 24 barriers studied in 1993, including alloys of Ni-Nb, WSi_x, Ni-Mo, Ir-Ta, together with their own work on Ti-W. Resistivity around 80-110 μΩ·cm was reported, lower than that of Ta-N and Ti-N, with the stability up to 750 ºC. Ta-TM (Ni [109], W [110], Fe, Co [111]) barriers showed high stability and acceptable resistivity.

Compared to the barriers containing nonmetallic element, amorphous alloys show the advantage of high conductivity and comparable barrier performance with Ta-N. In the advanced semiconductor technology, the requirement of high electrical conductivity becomes more critical. Amorphous alloy will attract more attention because of the advantage of high conductivity. However, so far studies on amorphous alloy are still preliminary. It is of great importance to establish an in-depth understanding on amorphous alloys as Cu diffusion barrier.

2.2.4. Barrier deposition methods

The deposition methods of Cu diffusion barrier are listed as:

1. physical-vapor deposition (PVD) [37, 112]
2. chemical vapor deposition (CVD) [113-117]
3. atomic-layer-deposition (ALD) [118-121]

In industry, CVD deposition was commonly used for Ti/Ti-N in Al metallization, while PVD deposition was widely adapted for Ta/Ta-N in Cu metallization. Compared to CVD and ALD, PVD process was a simple process because of the avoidance of gaseous precursor, and hence a lot of efforts were made to extend PVD-based barrier to 45 nm node CMOS process [112]. In terms of barrier performance, it was reported that PVD based barrier is also better than CVD based barrier, due to the more stable amorphous phase formed by PVD process [38]. However, application of PVD is restricted because of the less conformal barrier formed, while CVD process is able to provide barriers with better conformity and lower surface roughness. However this drawback of PVD process can be improved by a multiple step deposition which involves dry etching process to enhance the step coverage. Therefore PVD process is still the most popular process in industry. Compared to CVD and PVD process, ALD is studied more in research field. It shows precise thickness control at atomic level and to produce films with high conformality. which is promising for more advanced technology [118]. It was believed that ALD based barrier is a promising replacement for current PVD based barrier in industry application at 45 nm node and beyond [121]. However, the higher production cost and need of gaseous precursor restricted the application of ALD.

Besides the above mentioned deposition techniques, Ee et al. demonstrated novel deposition methods such as induced couple plasma (ICP) implantation of N into Ti-Si films [91], or chemical-physical vapor deposition (C-PVD) of Ti-Si-N film with Ti target, SiH_4 gas, and N_2 gas [90].

Other deposition and integration issues arise from integration with low-κ dielectric materials. In barrier deposition process like CVD or ALD deposition, it is difficult o

integrate pores larger than 2nm due to gaseous precursor penetration into the low-κ material [118], while ionized PVD processes usually are not able to provide a dense metal barrier on sidewalls. Sealing of pore structures are studied to avoid the integration issue of precursor penetration [122].

2.2.5. Summary

Based on the Cu diffusion retarding ability, the barrier property can be ranked as: TM-Si-N > Amorphous alloy / Ta-N > Ti-N > Ru-N > Ta > Ti > Ru. It should be noted that for amorphous alloy more studies are needed to understand the barrier behavior and failure mechanism. The properties are also dependent on other factors such as barrier thickness, barrier composition, deposition methods, deposition ambient, and substrate. A more detailed theoretical study will be discussed in Section 2.3.

2.3. Theoretical understanding on Cu diffusion barrier

Besides the experimental works on various barrier candidates, there are studies focusing on the theoretical understanding of Cu diffusion barrier, in terms of the factors affecting the barrier performance, the kinetics and thermodynamics involved in Cu barrier study, etc. There have also been studies on analytical simulation on Cu barrier performance. This section summarizes the theoretical understanding from Cu diffusion barrier study.

Table 2-2 Comparison among elemental metal, binary barrier and ternary barrier

	Elemental metal	Binary barrier	Ternary barrier
Barrier performance		**Increase** →	
Conductivity		**Decrease** →	
Thermal stability		**Increase** →	

2.3.1. The factors affecting barrier performance

2.3.1.1. Chemical formation

As discussed in Section 2.2, the Cu barriers mostly involve elemental, binary and ternary elements. Their barrier performance can be summarized in Table 2-2. However the theoretical understanding of the performance difference is not clear. Experimental works show that by doping with small atoms like N, Si, and C in transition metal, barrier effectiveness is improved with sacrifice of electrical conductance. The improvement of performance was usually explained by the "stuffing" effect of small inorganic atoms at the grain boundaries. However, Holloway et al. [45] showed different performance of Ta alloyed with 5 at% N and Ta_2N. In their work, while Ta_2N provided superior barrier performance than Ta, similar barrier performance and failure mechanism as Ta is shown by Ta (N). Therefore it is argued that effect of N on improving barrier properties should not be attributed to the "stuffing" effect. Other researches on TM-Si-N also show that for barrier with high N concentration, in spite that barrier stability increases with N concentration, Cu diffusion into dielectric layer was detected before barrier layer crystallization [123-125]. In research of ternary

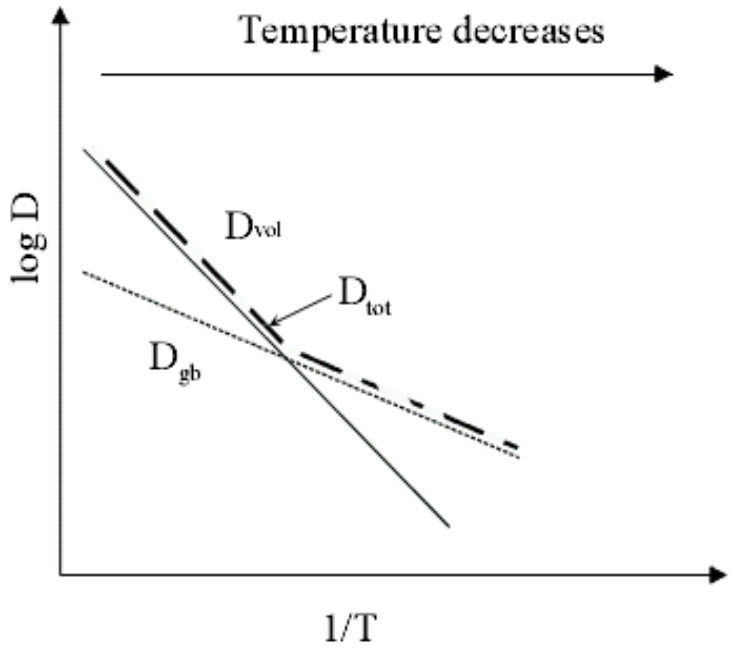

Fig. 2-4 Graph of Log D vs. 1/T showing that dominating diffusion mechanism changes from lattice diffusion to grain boundary diffusion with temperature increase

barrier with Si involved, it is believed that the high activation energy of Si_3N_4 crystallization helps increase thermal stability [126].

2.3.1.2. Microstructure

Diffusion kinetics show that diffusion mechanism strongly depends on temperature. As a result of larger activation energy, the diffusion coefficient of lattice diffusion is more sensitive to temperature change than grain boundary diffusion is. As shown in Fig. 2-4, the graph of log D vs. 1/T shows a general comparison between grain boundary diffusion and lattice diffusion. At temperature lower than 0.3 – 0.4 T_m of the host material, grain boundary diffusion is the predominant diffusion mechanism, which is 5-6 orders of magnitude faster than the bulk diffusion at 0.5 T_m. At room temperature, diffusion process is mostly controlled by grain boundary diffusion. This

phenomenon suggests that the key point to enhance the Cu diffusion barrier performance is to remove or reduce grain boundary. Therefore, barrier of either single crystalline or amorphous phase is needed [127].

Although it is generally believed that high stability can only be achieved by increasing energy barrier for crystallization, other research shows that amorphous or nano-crystalline phase itself could be quasi-stable by adjusting structure and composition. Recently, Millett [128] presented atomistic simulations that shows that oversized dopants segregated in FCC Cu has stabilizing effect. It shows that at certain dopant concentration, the nano-crystalline phase will have same free energy as crystalline phase of the same composition. The driving force of crystallization is therefore eliminated and nano-crystalline phase is quasi-stable. In Ramberg's calculation [129], it is also shown that for MoN and WN, crystalline phases are less stable.

2.3.2. Thermodynamics and kinetics in Cu diffusion barrier

Thin films with different microstructures can be obtained by the different deposition methods. In PVD deposition, due to the low atomic energy and directional atomic bombardment, the movement of atoms on substrate surface is kinetically hindered. It results in easier amorphous film formation. As a contrast, in CVD and ALD deposition, atoms usually have higher atomic energy and isotonic atomic movement. Compared to PVD, formation of amorphous film by ALD and CVD are not kinetically favored. Rather than obtaining quasi-stable amorphous barrier by kinetic control, design of

barrier with thermodynamical stability will be more important with CVD and ALD process.

Properties of Cu barriers could be studied based on interface reactivity and thermal stability. An ideal barrier should have stable Cu/barrier interface, e.g. minimized chemical reactivity. Otherwise the chemical gradient will contribute to the diffusion driving force according to Fick's first and second law. Ramberg summarized a series of binary and ternary phase diagram of transition metal-Cu and transition metal-Cu-N system [129]. It partially explained why Ta-N has better stability than Ti-N. While Ta has no reactivity with Cu, Ti and Cu and react and form Cu_4Ti to $CuTi_2$. Stability of silicide and boride were also extracted and compared through analysis of the phase diagrams.

Ramberg compared applications of transition metals based on the analysis of TM-B (Si, N)-Cu phase diagram. Based on this thermal dynamics approach, they summarized a few requirements for a stable amorphous metal formation, such as low free energy, existence of directional bonding, metals with different sizes but similar electronic structures, elements with several crystalline phases.

2.3.3. Analytical modeling of Cu diffusion barrier

Although less established as experimental works, there are a few analytical models on barrier studies. As barrier thickness reduces, Ouyang proposed a size-dependent kinetic model for studying interfacial diffusion in immiscible metallic multilayers [130]. They showed that in a Cu/Ta couple, when Ta thickness is less than 2 nm, Cu diffusion coefficient increases exponentially with decreasing diffusion length. There were a few studies on analytical simulation of diffusion system. Tian et al. [131]

described a model of diffusion couple, including the quantitative discussion of the barrier resistance. In a specific application, Gill et al. [132] recently presented a diffusion barrier model by considering a interconnect stack of metal/barrier/dielectric/semiconductor under electrical field. The diffusion flux is then expressed as $j = \mu EC - D\frac{\partial C}{\partial x}$, where μEC refers to the flux raised by electrical field, depending on capacitance C and electric field E. They concluded that the barrier performance was determined by combination of properties of the entire system. Their results show that at small diffusion coefficient of Cu in dielectric, a small change of the diffusion coefficient will significantly increase the time to failure.

2.4. Amorphous metallic thin films

Formation of amorphous metal and alloy are generally achieved by fast quenching of the metallic liquid or vapor. Metal atoms in melt state have very high mobility. It makes the crystallization difficult to be hindered when the melt is cooled down to the solid phase. The first amorphous pure metal was fabricated in mid-1950s by evaporating Ga and Bi onto glass substrates cooled to liquid-helium temperatures (about 4 Kelvin or -269 °C) [132]. The cooling rate was estimated to be higher than 10^{10} °C to freeze adatoms on the substrate. Compared to amorphous pure metal, formation of amorphous alloy could be achieved at a lower cooling rate (about 10^6 °C) [132]. It is because the atom mobility is lowered down by the interference of constituent atoms in the alloy. Bulk amorphous alloys with dimension of 1mm can be achieved commercially by fast quenching.

Compared to bulk metallic glass formation by fast quenching, amorphous metallic and semiconductor thin films are usually prepared by PVD and CVD process. Compared to

the liquid-to-solid transformation as in quenching process, the vapor-to-solid transformation in PVD or CVD deposition increases the tendency of forming amorphous phase [133]. However, not all alloys can form amorphous phase. Some empirical rules were drawn that glass forming binary alloys can be categorized in four groups, including alloy formed by transition metals and semimetals, noble metals and semimetals, early transition metals and late transition metal, and alloys of consisting IIA metals [132]. The glass forming range is usually near the deep or low temperature eutectics on the phase diagram.

Compared to crystalline metals and alloys, amorphous metallic thin films have superior properties such as good soft-magnetic properties, high specific strength, large elastic limit, and high resistance to corrosion and wear. Therefore they are often used as coating layers. In recent years, there have been studies on using amorphous metallic thin films on optoelectronics, MEMS, and memory devices.

As discussed in section 2.2.3, there have been some studies on Cu diffusion barrier using binary alloys. In spite of the early works, there is a lack of systematic study and in-depth understanding. Therefore there is a need to have a systematic study from the fundamental of amorphous thin films formation based on binary alloys. It will provide good guidance for Cu diffusion barrier material selection, and provide a reference for future exploration on the formation and application of binary amorphous alloy thin films.

2.5. Summary remarks

Because of the potential damage of Cu diffusion into Si and dielectric layers, especially when low- κ materials are widely used, further research on diffusion barriers with good thermal stability and diffusion retarding ability is required. Current

research mainly focused on experimental studies, although some theoretical studies through thermodynamical and analytical calculation also exist.

Despite many studies on Cu diffusion barrier, there is a lack of systemic understanding and evaluation of the performance of various barriers, especially when the electrical properties are considered. A study to understand the mechanism of forming stable and conductive Cu diffusion barrier is thus needed. The review on amorphous metallic thin films showed the potential of using amorphous metallic thin films as diffusion barrier.

Chapter 3. Experimental Methods

The experimental details of the work are introduced in this chapter, including the barriers formation, thin film properties measurement, and barrier performance evaluation.

3.1. Sample preparation

3.1.1. Substrate preparation

The studied barriers were deposited on Si substrates. The substrates were prepared from a 12 inch (1 0 0) Si wafer of 700 μm think. The Si wafer was cut to pieces of 1 cm × 1 cm, and cleaned using standard cleaning process SC1 solution (1 H_2O_2 : 1 HCl: 5 DI water) and SC2 solution(1 H_2O_2: 1 NH_4OH: 6 DI water). The substrates were soaked in SC1 for 10 min to remove the organic contamination and rinsed with DI water, then soaked in SC2 solution for 10 min to remove inorganic contamination and rinsed with DI water. They were then dried with N_2 gun.

3.1.2. Sputtering system

Multi-targets magnetron sputtering system was utilized in this study. Fig. 3-1 shows the schematics of the multi-targets magnetron sputtering system. It consists of a few parts: a high vacuum chamber with vacuum level up to 5.32×10^{-4} Pa, target magnetrons with DC/RF power supply, substrate holder with rotation control and RF power supply, and gas precursor of Ar or N_2.

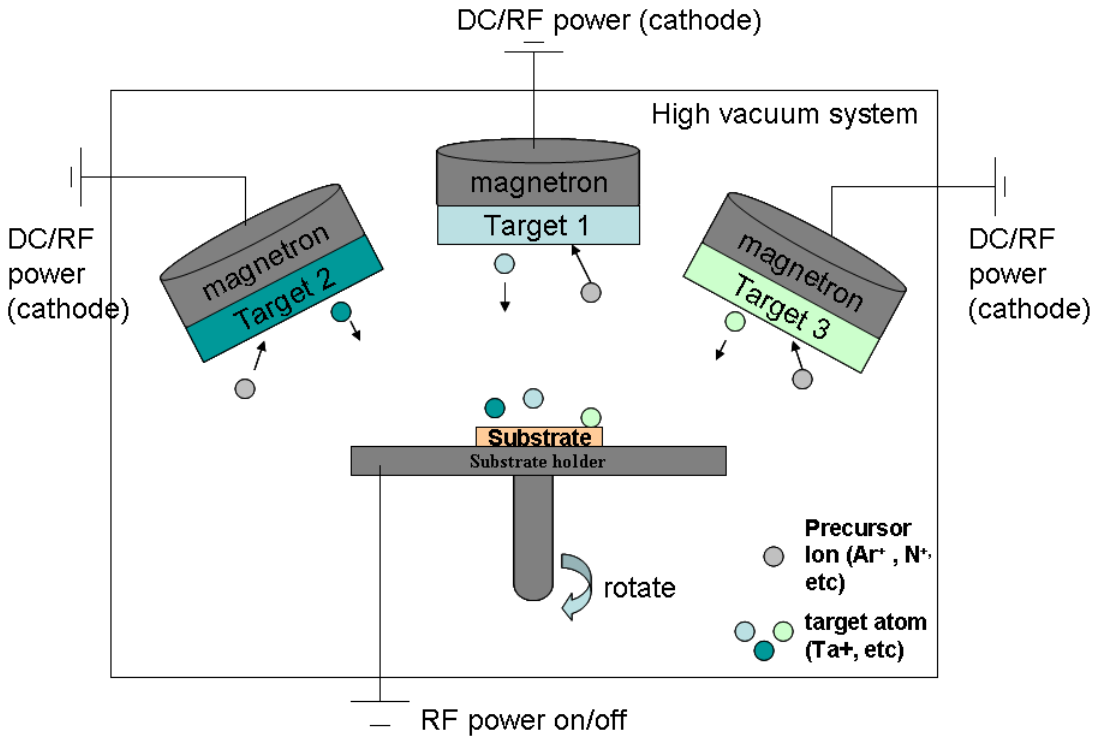

Fig. 3-1 Schematics of the multi-targets magnetron sputtering system

This system supports up to three targets, with either direct current (dc) or radiofrequency (rf) power. By using the multi-targets magnetron sputtering system, the barriers and Cu can be deposited in sequence within vacuum environment. DC power from 0 W to 300 W can be applied to the nonmagnetic metallic target, while RF power from 0 W to 250 W can be applied to magnetic target. Each target can be blocked from substrate by a shutter. For all the sputtering, the targets are pre-sputtered for 5 min without open the shutter to remove the surface contaminations. RF power from 0 W to 150 W can be applied to substrate. Substrate rotation at 40 rpm can be applied during the sputtering to ensure uniform film composition.

3.1.3. Sample preparation for Ta, Ta-N, and Ta-Si-N barrier study

Formation, properties, and Cu diffusion barrier performances of Ta, Ta-N and Ta-Si-N film on Si substrate are studied. Ta-N and Ta-Si-N films with a wide composition range were deposited on Si substrates. 3-inch Ta and Si targets were used. DC and RF powers were applied on Ta and Si targets during deposition. Ta-N and Ta-Si-N films with multiple compositions were formed by adjusting the N_2 gas flow. The electrical resistance and thermal stability of Ta-N and Ta-Si-N thin film of various compositions were studied. The barrier formation was followed by the Cu deposition on selected samples within vacuum environment. The barrier performance and failure mechanism of Ta, Ta-N, and Ta-Si-N films were studied. The sputtering conditions are listed in Table 3-1.

Table 3-1 Deposition conditions for Ta-N/Si, Ta-Si-N/Si, Cu/Ta/Si, Cu/Ta-N/Si and Cu/Ta-Si-N/Si samples

	Ta-N/Si	Ta-Si-N/Si	Cu/Ta/Si	Cu/Ta-N/Si	Cu/Ta-Si-N/Si
Pre-sputtering vacuum (Pa)	5.32×10^{-4}	5.32×10^{-4}	5.32× 10-4	5.32× 10-4	5.32×10^{-4}
Sputtering power	Ta: 200 W DC	Ta: 200 W DC Si : 100 W RF	Ta: 200 W DC Cu: 200 W DC	Ta: 200 W DC Cu: 200 W DC	Ta: 200 W DC Si : 100 W RF Cu: 200 W DC
Ar flow rate (sccm)	20	20	20	20	20
N2 flow rate (sccm)	3, 7, 8.5, 10	3, 5, 7, 8.5, 10	0	10	8.5
Sputtering pressure (mtorr)	20	20	20	20	20
Film thickness (nm)	83-112	102-120	Cu: 230 Ta: 92	Cu: 212 Ta-N: 107	Cu: 195 Ta-Si-N: 89

3.1.4. Sample preparation for Ta-Ni, Ta-Cr and Ta-Ti barrier study

Ta-TM/Si thin films with several compositions were prepared to study the microstructures and thermal stabilities of Ta-TM thin films with change of compositions. Three groups of Ta-TM thin films were prepared, including Ta-Ni, Ta-Cr, and Ta-Ti. A magnetron sputtering system with two targets was used for the sample preparation with the targets of Ta and TM (TM = Ni, Cr, or Ti). The power settings of Ta and transition metals were adjusted to obtain films of different compositions. The films were deposited on Si substrate. The thicknesses were controlled to be around 1000 nm. The relatively thick Ta-TM films were to understand the microstructures of the films, as well as the microstructural revolution at elevated temperatures. The thin film samples Cu/Ta-TM/Si were prepared by using three targets. DC power was applied on a Cu target. Ta-TM barriers were deposited by co-sputtering using Ta and TM targets with selected compositions, followed by sputtering of Cu films within vacuum environment. The sputtering parameters are shown in Table 3-2.

Table 3-2 Deposition conditions for Ta-TM/Si and Cu/Ta-TM/Si samples

	Ta-Ni/Si	Cu/Ta-Ni/Si	Ta-Cr/Si	Cu/Ta-Cr/Si	Ta-Ti/Si	Cu/Ta-Ti/Si
Pre-sputtering vacuum (Pa)	5.32×10^{-4}	5.32×10^{-4}	5.32×10^{-4}	5.32×10^{-4}	5.32×10^{-4}	5.32×10^{-4}
Sputtering power	Ta: 200 W DC, Ni: 200 W RF	Ta: 200 W RF Ni : 80W DC Cu : 200 W DC	Ta: 200 W RF, Cr: 30 W DC	Ta: 200 W RF Cr : 80W DC Cu : 200 W DC	Ta: 200 W RF, Ti: 30 W DC	Ta: 200 W RF Ti : 80W DC Cu : 200 W DC
	Ta: 300 W RF, Ni: 50 W DC		Ta: 200 W RF, Cr: 50 W DC		Ta: 200 W RF, Ti: 50 W DC	
	Ta: 200 W RF, Ni: 100 W DC		Ta: 200 W RF, Cr: 80 W DC		Ta: 200 W RF, Ti: 80 W DC	
	Ta: 200 W RF, Ni 150 W DC		Ta: 200 W RF, Cr : 100 W DC		Ta: 200 W RF, Ti : 100 W DC	
Ar flow rate (sccm)	20	20	20	20	20	20
Sputtering pressure (mTorr)	20	20	20	20	20	20
Film thickness (nm)	957 – 1131	Cu: 232 Ta-Ni: 89	932 – 987	Cu: 198 Ta-Cr: 78	897 – 1033	Cu: 190 Ta-Ti: 85

Table 3-3 Deposition conditions for Ta-Ni/Si and Cu/Ta-Ni/Si samples with variation of substrate bias

	Ta-Ni/Si	Cu/Ta-Ni/Si
Pre-sputtering vacuum (Pa)	5.32×10^{-4}	5.32×10^{-4}
Sputtering power	Ta: 200 W RF Ni : 80W DC	Ta: 200 W RF Ni : 80W DC Cu: 200 W DC
Ar flow rate (sccm)	20	20
Sputtering pressure (mTorr)	20	20
Substrate RF bias applied during barrier deposition (W)	0, 25, 50, 75, 100	0, 100
Film thickness (nm)	899-1023	Cu: 232, 178 Ta-Ni: 89, 67

3.1.5. Sample preparation for Ta-Ni barrier study with controlled oxygen concentration

During the study on the barrier films, oxygen was found in the barrier thin films. As discussed in the literature review, it is important to understand the source of the O and the effect of O on the barrier performance. As reported by previous studies, DC bias applied on substrate during sputtering could affect O concentration during thin film deposition [133]. In the current work, O concentration was adjusted by applying RF bias substrates during thin film deposition using the multi-targets magnetron sputtering system. Ta-Ni/Si thin films with different bias were studied to investigate the effect of substrate bias on the thin film compositions and film properties. In order to understand the O source, a set of samples were deposited with passivation layers of Cu. The Cu films were deposited on Ta-Ni thin films within vacuum environment, in order to protect the film from oxygen in atmosphere after film deposition. The deposition parameters are shown in Table 3-3.

3.1.6. Annealing treatment

In order to study the thermal stability of the samples and the microstructure evolution, selected samples were annealed at temperatures ranging from 400 °C to 1000 °C for 30 min. As it is well known that Ta is O getter, the annealing was done in the vacuum furnace at 10^{-2} Pa in order to avoid thin film oxidation in atmosphere. A Carbolite vacuum furnace system was used this work, with the furnace temperature up to 1200 °C and the heating rate of 3 °C/min.

3.2. Characterization methods

3.2.1. Step surface profiler

Alpha-Step 500 surface profiler was used to calculate the deposition rate and to measure the thin film thickness. One edge of the substrate was covered by thermal tape during deposition. The thermal tape was removed after deposition and a step was formed. The step height was measured using the surface profiler. The deposition rate was calculated from the thin film thickness and the sputtering time.

3.2.2. 4 - Point probe station

The Keithley 4-point probe station was used to measure the sheet resistance of the thin films. The sheet resistance of the thin film was calculated using the equation:

$$Rs = \frac{A \times V}{I} \tag{2.2}$$

where Rs is the sheet resistance, V is the applied voltage and I is the measured current. The constant A is related to the geometry of the thin film, and equals to 4.53 when the size of the films is relatively large. The resistivity of the thin film can be calculated by

$$\rho = Rs \times t \tag{2.3}$$

where ρ is resistivity and t is film thickness. In this study, as the resistivity of Si is much higher than that of the thin films, it can be assumed that the current mainly goes through the thin films during resistance measurement.

3.2.3. X-Ray diffractometer (XRD)

Grazing angle incidence 2θ mode X-ray diffraction (GAXRD) was used for microstructure identification. For GAXRD, the incident beam is fixed, while the reflected angle moves across the 2θ angle. The schematic of a GAXRD is shown in Fig. 3-2. By fixing the incident angle, the signal collected from the substrate can be minimized. It thus improves the sensitivity of the thin films signal detection. In the current work, Rigaku Dmax 2200 XRD was used. The incident angle α was fixed at 1°. Scanning speed was set from 1°/min to 2°/min.

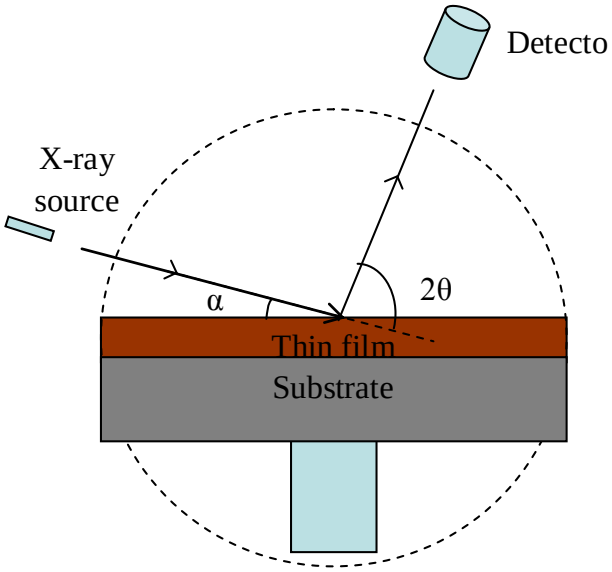

Fig. 3-2 Schematics of a glancing Angle X-ray Diffractometer (GAXRD)

3.2.4. Field emission scanning electron microscopy (FESEM)

High-resolution field emission scanning electron microscope (FESEM) was used to study the surface morphology of the thin films. JEOL JSM-6340F SEM with cold cathode FEG electron source was used in current work.

In scanning electron microscope, primary electron beams are generated from electron sources with beam size as small as 2 – 10 nm. The primary electron beams are accelerated in vacuum with energy of 0.5 - 30 keV before hitting the sample surface. Different types of particles are generated as result of the collision, among which low energy secondary electrons are collected for imaging. Secondary electrons are generated from the samples surface. Intensity of the secondary electrons is largely determined by the topography of the sample. The small spot size enhances the lateral

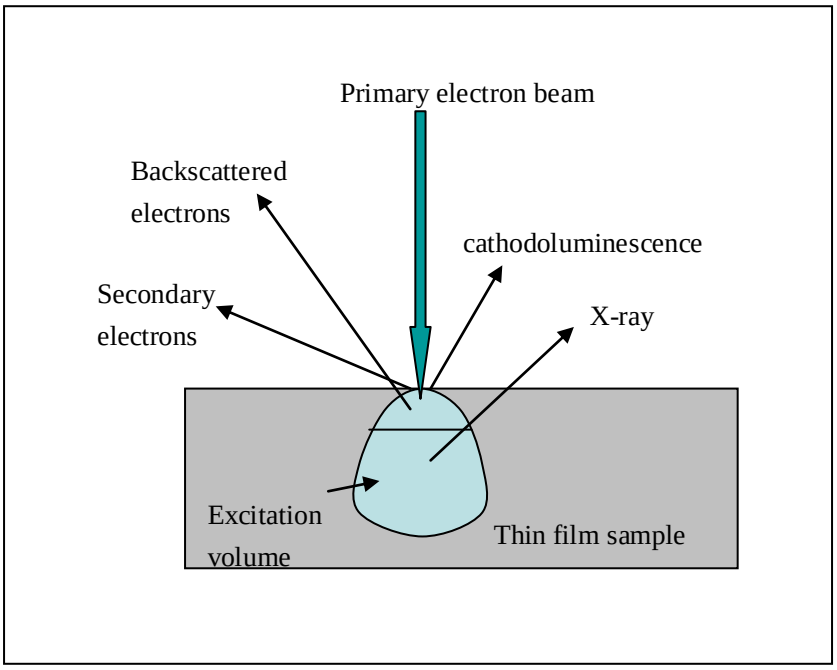

Fig. 3-3 Generation of secondary electron during SEM operation

resolution of the SEM images. The surface topography image of the sample is thus obtained from the secondary electrons intensities when scanning the electron beam on the sample surface. The generation of secondary electrons during SEM operation is shown in Fig. 3-3.

The difference between FESEM and conventional thermionic SEM is the electron source. In thermionic SEM, electrons are generated from W or LaB_6 tips under high voltage. High accelerating voltage is needed to generate primary electrons with narrow beam size. The high energy of the primary electrons may cause sample surface damage and surface charging, resulting in poor imaging. In FESEM, electron beam with high coherency and narrow beam size can be generated with low accelerating voltage. The accelerating voltage is 5 keV in current study. Compared with thermionic SEM, FESEM provides greater spatial resolution due to the smaller scattering volume at

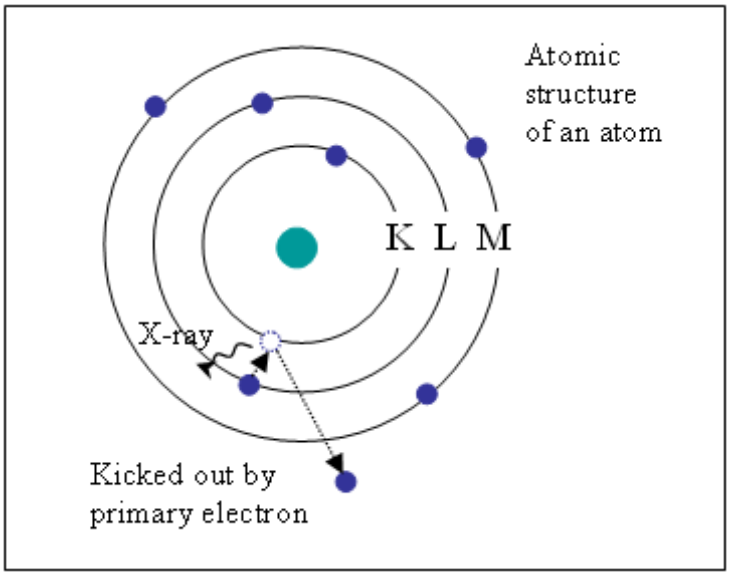

Fig. 3-4 Characteristic X-ray generation mechanism when high energy electron bombard with sample atom

lower electron energy. It also achieves greater depth of field and minimal chromatic aberration. Image with better qualities can be obtained by using FESEM.

3.2.5. Energy dispersive x-ray spectroscopy (EDX)

Energy- dispersive x-ray spectroscopy (EDX) was used to analyze the composition of the thin films. The EDX was attached to a scanning electronic microscopy (SEM). JEOL JSM-6360 SEM with an EDAX energy dispersive x-ray detectors was used in current work.

During the SEM operation, x-rays are generated when the primary electron beam interact with the elements' inner core electrons of the materials under study. When the energy of the primary electron beam is high enough, electron on the inner most orbital of the sample atom will be kicked out and neighboring outer electrons. An electron from outer high energy shell will move to the vacant inner electron shell. The

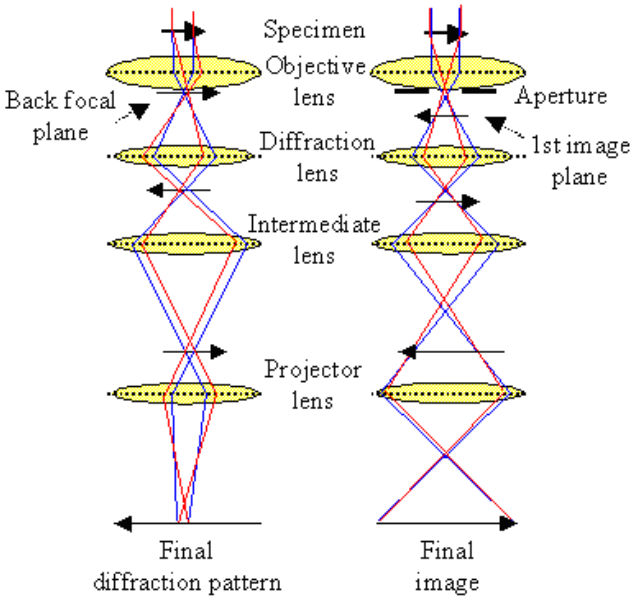

Fig. 3-5 Schematic of transmission electron microscopy [On-line, www.tf.uni-kiel.de]

energy difference between the outer high energy shell and the inner low energy shell will be released in the form of X-ray. The X-ray energy is determined by the atomic structure of the element. Elemental composition can thus be obtained from the energy and the counts of the X-ray. The mechanism is illuminated as in Fig. 3-4. Higher primary electron energy is needed in order to stimulate atoms with high atomic weight. Accelerating voltage of 20KeV is used in the current work.

3.2.6. Transmission electron microscopy (TEM)

Transmission electron microscopy (TEM) is a powerful tool to study the morphology and crystal structure in nano-scale. JEM-2100F with energy dispersive X-ray spectrometer (EDS) system was used in this study. It worked at accelerating voltage of 200 keV, with resolution of 1.9 Å.

In general operation of TEM, electrons are generated from thermionic gun under accelerating voltage of 125 to 300 keV. The high energy electron has small effective wavelength, resulting in high lateral resolution. When the electron beam is focused on the surface of the sample, the high energy electron beam penetrates through the thin sample with diffraction. Diffraction occurs when elastic scattering occurs when electron interacts with potential field of the atoms with no energy loss. On the other hand, structure such as grain boundaries, dislocations, secondary phase will result in irregular diffraction pattern. The diffracted electron beam passes through a set of lenses and apertures in high vacuum after they transmits through the TEM samples. The diffraction patterns or image can collected by the fluorescent screen or detector located below the lenses. The schematic drawing of the TEM is given in Fig. 3-5.

In order to obtain TEM images or diffraction pattern with good quality, TEM samples has to be thin enough to allow electron transition. Good sample preparation is critical to obtain reliable information from TEM observation. TEM sample of 50 – 100 nm is usually required. Cross-sectional TEM samples were prepared in order to understand the interfacial reaction between Cu, barrier, and substrate. A typical sample includes a few stages: (1) cut sample to required size; (2) attach sample to holder; (3) thin down sample by grinding and polishing; (4) make sample with required thickness by ion-milling. Fig. 3-6 shows a typical cross-sectional TEM sample

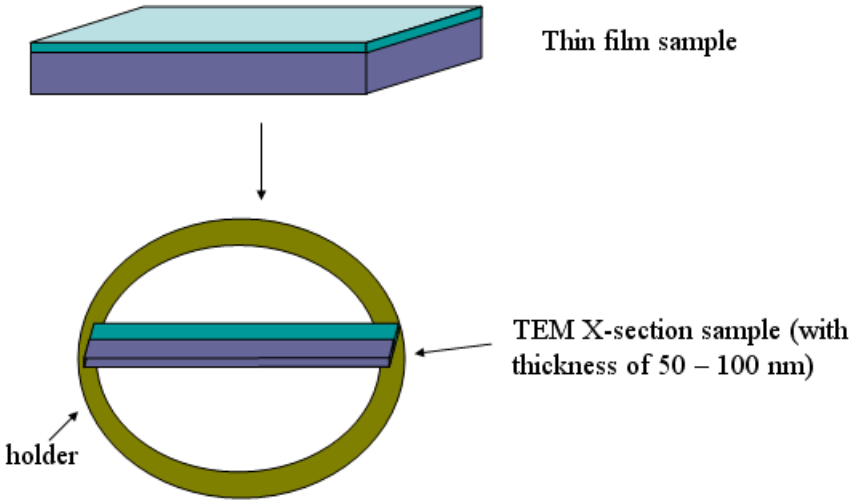

Fig. 3-6 Cross-sectional TEM sample preparation

3.2.7. X-ray photoelectron spectroscopy (XPS)

X-ray photoelectron spectroscopy (XPS) is a surface analysis tool for understanding the chemical bonding and composition of the solid material. In the current work VG ESCALAB 220I-XL system was used with 1486.7 eV Al Kα irradiation. The XPS was used to understanding the composition and bonding in Ta-Si-N thin films.

During the operation of XPS, the surface atoms of the studied material are irradiated by an X-ray beam. X-ray photoelectrons excited from the surface solid are collected by the analyzer. The count and kinetic energy of the electrons are recorded and it gives the XPS spectra. Ultra high vacuum (UHV) system is needed, around 10^{-9} mbar. The working principle of XPS can be explained by Fig. 3-7.

As the photoelectrons are generated from within the top 10-12 nm materials, XPS is a surface sensitive tool. The characteristic peaks of the binding energy indicate the electron configurations of the materials element, e.g. the chemical state of the element.

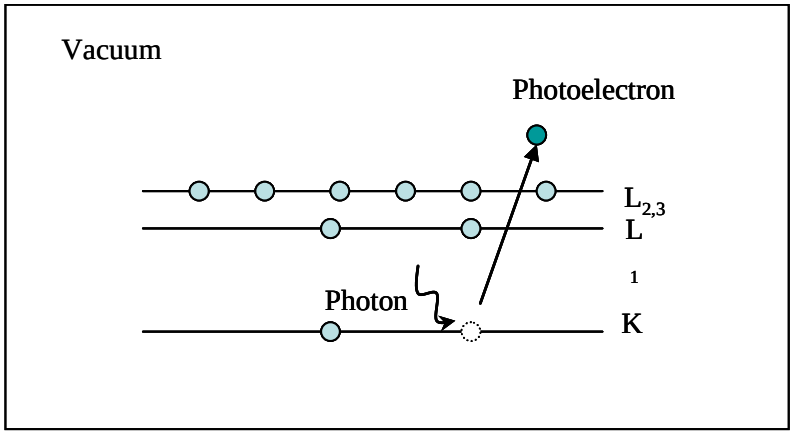

Fig. 3-7 Photoelectron generation of XPS

As the energy of the incident X-ray is fixed, the electron binding energy (BE) of the emitted electrons can be calculated by the equation:

$$E_{binding} = E_{photon} - (E_{kinetic} + \varphi) \tag{2.4}$$

where $E_{binding}$ refers to the binding energy of the electron, E_{photon} refers to the energy of the X-ray photons, $E_{kinetic}$ refers to the kinetic energy of the measured electron and ϕ refers to the work function of the spectrometer. The amount of the electrons for each peak is converted to the element composition of the material using "relative sensitive factor (RSF)". The XPS spectra was quantitatively analyzed using CASA-XPS package with the spectra calibrated to C 1s peak at 284.6 eV to account for the charging effect.

3.2.8. Time-of-flight secondary ion mass spectrometry (ToF-SIMS)

ToF-SIMS is a surface sensitive analytical method. During the operation, the atoms from the outermost monolayer of sample are removed by high energy pulsed ion beam.

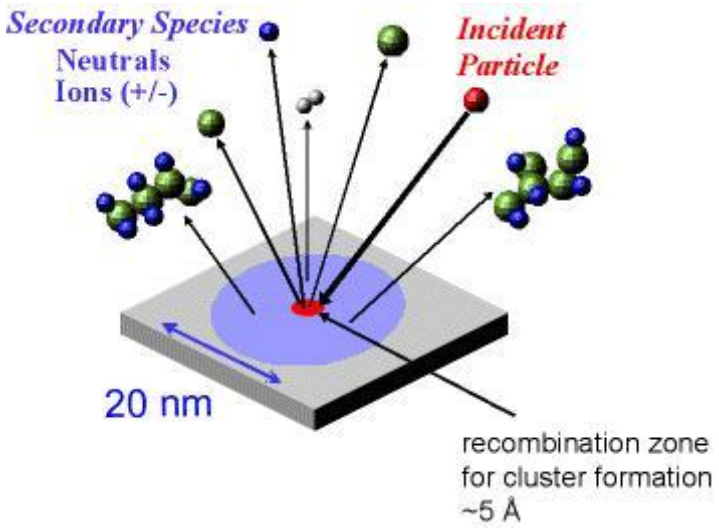

Fig. 3-8 Working principle of ToF-SIMS [On-line, serc.carleton.edu]

The generated secondary ions are accelerated inside a "flight tube". Due to the different atomic mass, the ions have different flight speed and thus arrive at the detector a different time, or so-called "time of flight". The atomic weights of the atoms are determined by time of flight. High accuracy can be achieved by ToF-SIMS, with mass resolution to 0.00x atomic mass unit. The working principle of ToF-SIMS is shown in Fig. 3-8.

An IONTOF® ToF-SIMS with impact energy of 1 keV Ar+ ion primary beam was used in this work. The depth profiles of the thin films were studied by ToF-SIMS by sequential sputtering of material surfaces, to understand the diffusion profile of each atom among each other after thermal annealing.

Chapter 4. Formation and Properties of Reactively Sputtered Ta-N and Ta-Si-N Thin Films on Si Substrate

Ta-N and Ta-Si-N have shown high stability in previous studies. However, the understanding of the high stability of these two films is lacking. In this work, we would like to study the film formation and the chemical bonding of Ta-N and Ta-Si-N, and to understand the relation between the chemical bonding and film properties such as electrical resistivity, microstructures, and thermal stability of Ta-N and Ta-Si-N. It will enhance the understanding of amorphous thin film formation.

4.1. Ta-N/Si

4.1.1. Composition and chemical state

Compositions of Ta-N thin films deposited at different N_2 flow are listed in Table 4-1. It should be pointed out that the deposited films have a certain percentage of oxygen. As to be discussed later, oxygen is commonly incorporated in Ta-based thin films. The source and effect of oxygen will be discussed in details in Chapter 7. To avoid confusion, it will not be included in the composition presented in Chapter 4 - Chapter 6. An increase of N percentage from 15.8 at% to 31.0 at% were obtained with N_2 flow ratio increasing from 13.0 % to 33.3 %, showing the success of depositing Ta-N thin films with wide composition range using reactive sputtering.

Table 4-1 Compositions of Ta-N films deposited with different N_2 gas flow

N_2 flow rate / N_2+Ar flow rate (sccm)	N_2 ratio (%)	Composition (at%)	Annotation
3/23	13.0	Ta: 84.2; N: 15.8	$Ta_{84}N_{16}$
7/27	25.9	Ta: 80.0; N: 20.0	$Ta_{80}N_{20}$
8.5/28.5	29.8	Ta: 73.7; N: 26.3	$Ta_{74}N_{26}$
10/30	33.3	Ta: 69.0; N: 31.0	$Ta_{69}N_{31}$

Further study of XPS photoelectron spectroscopy showed the bonding state change of all elements in Ta-N. Fig. 4-1 (a) shows the Ta4f peaks of Ta-N barriers. A pair of Ta4f doublets was observed in all films, while an extra hump was shown at lower energy in $Ta_{74}N_{26}$ and $Ta_{69}N_{31}$. The quantitative spectra fitting for $Ta_{84}N_{16}$ and $Ta_{69}N_{31}$ using CASA-XPS are shown in Fig. 4-1(b) and (c), respectively. As Ta4f doublet peaks consists of Ta4f7/2 and Ta4f5/2 with fixed difference of 1.9 eV-2.0 eV, only Ta4f7/2 is discussed here. The binding energy of Ta4f7/2 shows the different compound formed in the films. In $Ta_{84}N_{16}$, two bonding states of Ta7/2 were observed, including metallic Ta at 21.9 eV, and Ta_2O_5 at 25.7 eV. In $Ta_{69}N_{31}$, there was no metallic Ta bonding. Instead, Ta4f7/2 peaks at 24.2 eV and 26.0 eV were identified as Ta-ON bonding, showing the existence of $Ta(ON)_x$. It was reported that Ta4f7/2 peak is at 23.0eV in TaN and at 22.5 eV in Ta_2N [134]. In current investigation, there was no sign for TaN or TaN_2 formation. Therefore, we conclude that the as-deposited Ta-N forms were consisted of Ta, Ta_2O_5 and $Ta(ON)_x$.

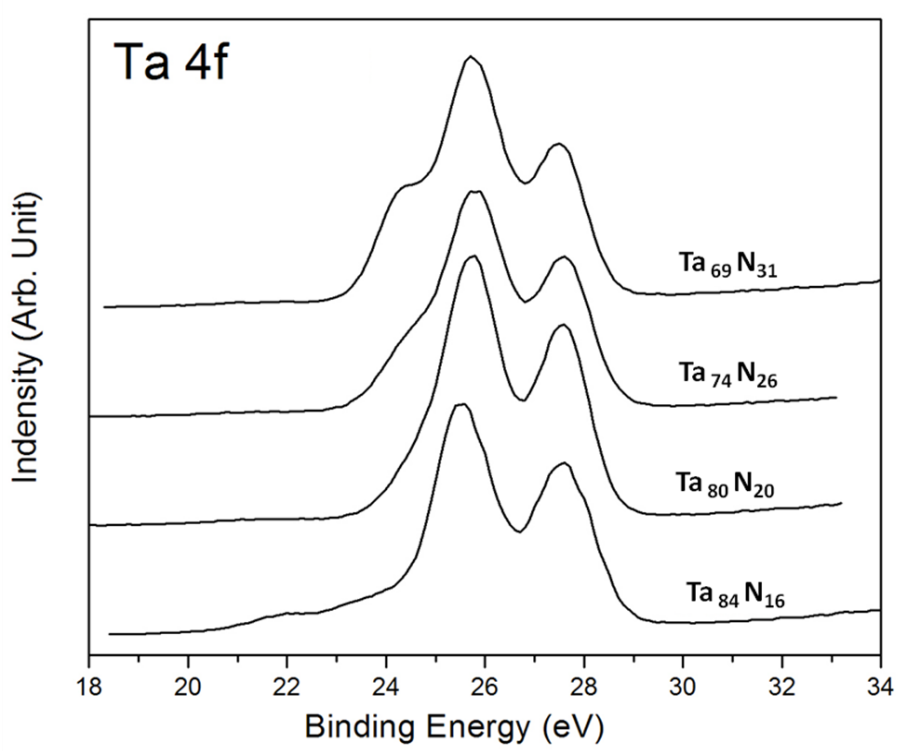
Ta 4f
Indensity (Arb. Unit)
Ta 69 N31
Ta 74 N26
Ta 80 N20
Ta 84 N16
18
20
22
24
26
28
30
32
34
Binding Energy (eV)

(a)

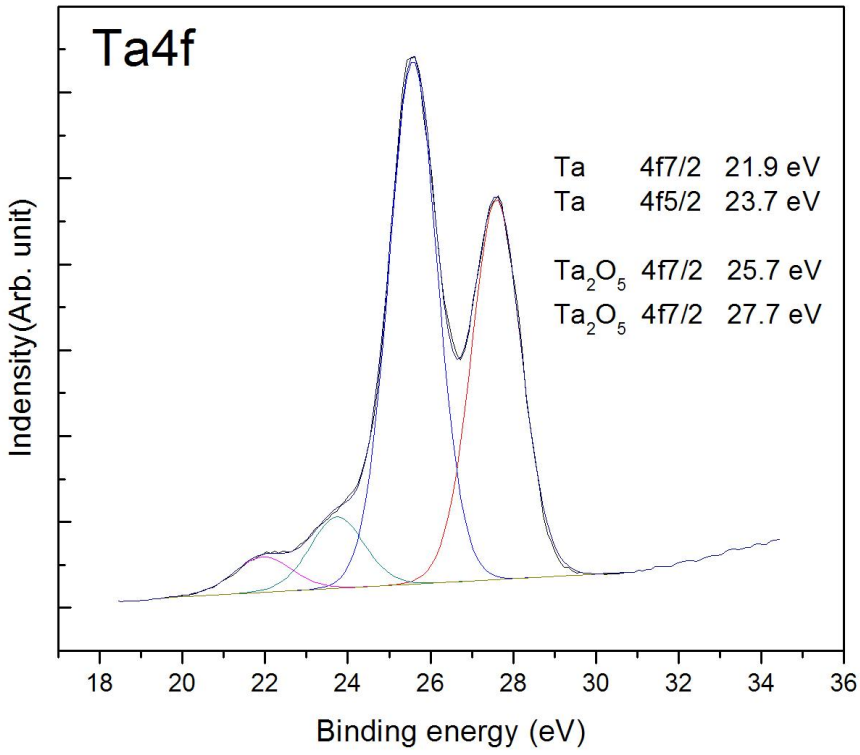
Ta4f
Indensity(Arb. unit)
Ta 4f7/2 21.9 eV
Ta 4f5/2 23.7 eV
Ta2O5 4f7/2 25.7 eV
Ta2O5 4f7/2 27.7 eV
18
20
22
24
26
28
30
32
34
36
Binding energy (eV)

(b)

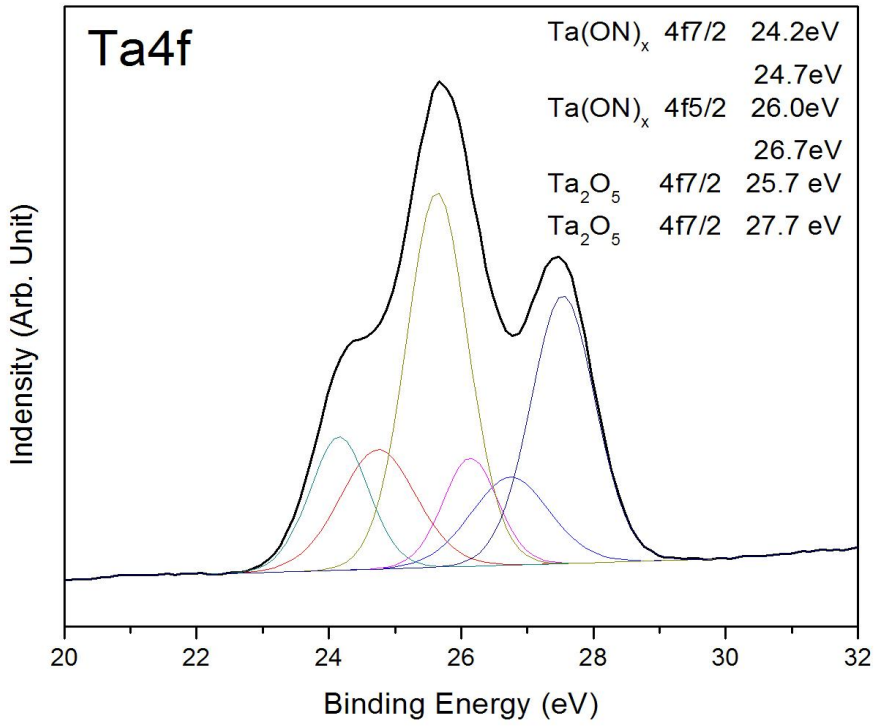

(c)

Fig. 4-1 XPS photoelectron spectroscopy of: (a) Ta 4f peak of all Ta-N barriers; (b) Ta 4f peak of $Ta_{74}N_{16}$ with spectra fitting showing Ta and Ta_2O_5 bonding; (c) Ta 4f peak of $Ta_{69}N_{31}$, with spectra fitting showing $Ta(ON)_x$ and Ta_2O_5 bonding;

4.1.2. Resistivity

The as-deposited resistivity was collected for 3 groups of Ta-N samples, as shown in Table 4-2. Resistivity of 627-679 μΩ·cm was measured, with a higher resistivity at increased N concentration. The correlation between resistivity and N concentration is consistent with Chung et al. [107]. The Ta-N resistivity has been reported with different range, such as 100 μΩ·cm to 500 μΩ·cm as reported by Aouadi and Debessai [135]. Current work is consistent with Chung et al.'s report that Ta-N barriers may possess resistivity from 210 μΩ·cm to higher than 1000 μΩ·cm [136]. Oku et al reported the Ta-N could have resistivity as high as 10^5 μΩ·cm [7], which is also not observed in our study. It might be due to the different film composition.

Table 4-2 Resistivity of as-deposited Ta-N with different composition

Film composition	Electrical resistivity (μΩ·cm)
$Ta_{80}N_{20}$	626.99
$Ta_{74}N_{26}$	642.40
$Ta_{69}N_{31}$	679.36

4.1.3. As-deposited microstructure

XRD diffraction pattern for as-deposited Ta-N is shown in Fig. 4-2. All films were amorphous. In $Ta_{84}N_{16,}$ a broad hump centering at 36.9 ° was identified as amorphous Ta, which tally with XPS result that showed metallic Ta in as-deposited $Ta_{84}N_{16}$ film. In films with higher N concentration, this amorphous Ta peak was not obvious.

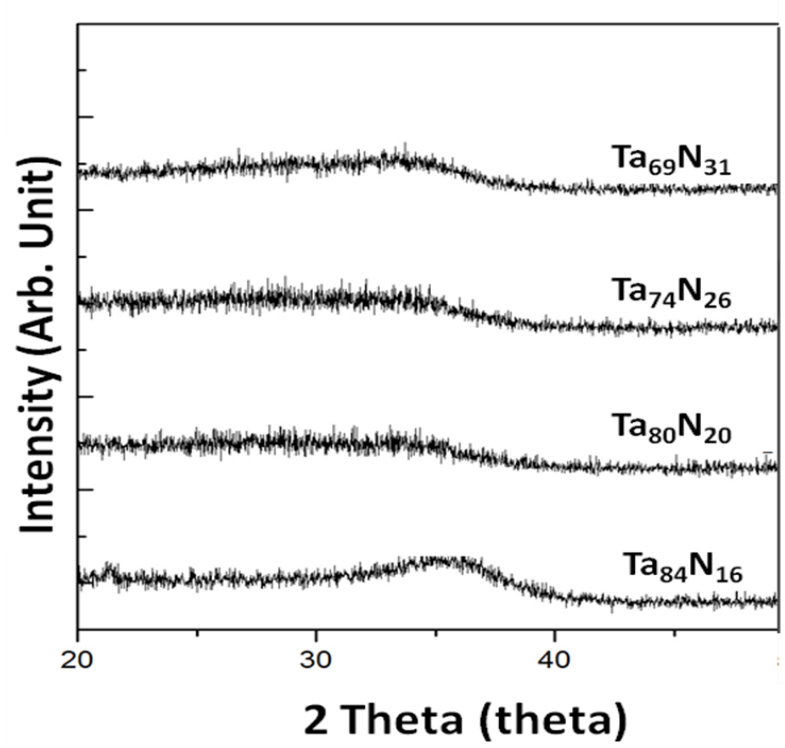

Fig. 4-2 XRD diffraction pattern of as-deposited Ta-N/Si samples

4.2. Thermal stability

Ta-N thin films were annealed in vacuum at temperatures from 400 °C to 1000 °C in order to evaluate the thermal stability. All films showed similar stability. XRD diffraction pattern evolution of $Ta_{74}N_{26}$ is shown in Fig. 4-3 as an example. At temperatures lower than 800 °C, the thin film showed amorphous structure similar to the as-deposited state. Crystallization started at 800 °C, as shown by sharp Ta_2O_5 peak at 22.9 °. The crystal peaks further grew at 1000 °C. No $TaSi_x$ was observed. This indicates that the crystallization occurred before Ta reacted with Si in substrate. This is different from the previous report that Ta-N barrier fails at 700 °C -750 °C with formation of $TaSi_x$ [58].

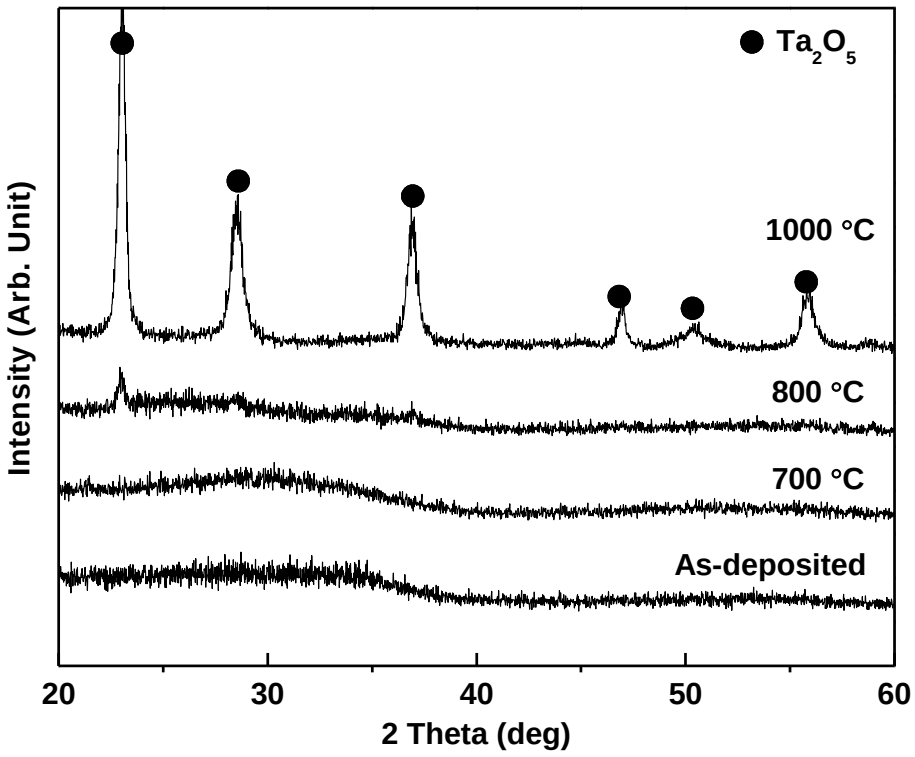

Fig. 4-3 XRD diffraction pattern of annealed $Ta_{74}N_{26}$

Table 4-3 Compositions of Ta-Si-N films deposited with different N_2 gas flow

N_2 flow rate /total gas flow rate (sccm)	N_2 ratio (%)	Composition (at%)	Anotation
3/23	13.0	Ta: 72.2; Si: 17.7; N: 10.1	$Ta_{72}Si_{18}N_{10}$
5/25	20.0	Ta: 73.1; Si: 14.4; N: 12.8	$Ta_{73}Si_{14}N_{13}$
7/27	25.9	Ta: 75.3; Si: 8.2; N: 16.5	$Ta_{75}Si_{8}N_{17}$
8.5/28.5	29.8	Ta: 77.2; Si: 8.9; N: 13.9	$Ta_{77}Si_{9}N_{14}$
10/30	33.3	Ta: 79.5; Si: 7.7; N: 12.8	$Ta_{79}Si_{8}N_{13}$

4.3. Ta-Si-N/Si

4.3.1. Composition and chemical state

Compositions of Ta-Si-N deposited at different N_2 flow are listed in Table 4-3. With increase of N_2 flow rate, atomic percentage of N increased first and then decreased, with maxima at N_2 flow ratio of 25.9 %. The observation of N concentration trend change was reported in studies of Ti-Si-N and Ti-B-N. Atomic percentage of Si showed fluctuation with different N_2 flow rate.

Different from Ta-N, three groups of Ta4f7 at 22.5-22.9 eV, 24.4-24.9 eV and 26.6-27.0 eV were extracted. Ta4f7 at 22.5-22.9 eV was identified as Ta-O-Si, showing the existence of $TaSi_xO_y$[137]. Another group of Ta 4f7 at 24.4-24.9 eV was attributed to TaO_x or TaN_x, such as 24.4 eV for Ta_3N_5 or 24.6 eV for TaN. The third peak was indentified as $TaSi_x$, verified by Si 2p peaks at 98.5-98.7 eV. Therefore the result shows the Ta-Si-N films were consisted of $TaSi_xO_y$, TaO_x, Ta_xN_y and $TaSi_x$. TaSix. The composition of films are listed in Table 4-5.

Table 4-4 Resistivity of as-deposited Ta-Si-N with different composition

Film composition	Resistivity (μΩ·cm)
$Ta_{72}Si_{18}N_{10}$	772.10
$Ta_{73}Si_{14}N_{13}$	1543.10
$Ta_{75}Si_{8}N_{17}$	122700.00
$Ta_{77}Si_{9}N_{14}$	19760.47
$Ta_{79}Si_{8}N_{13}$	2170.93

4.3.2. Resistivity

The as-deposited resistivity is shown in Table 4-4. Ta-Si-N barriers showed much higher resistivity than Ta-N barrier, with variation from 772 μΩ·cm to 122700 μΩ·cm. It was also observed that at high N concentration, the resistivity is much higher.

4.3.3. As-deposited microstructure

XRD diffraction pattern for as-deposited Ta-Si-N barriers are shown in Fig. 4-2. The high crystalline peaks were identified as Si (200) peak. Similar as Ta-N, All Ta-Si-N films showed amorphous structure.

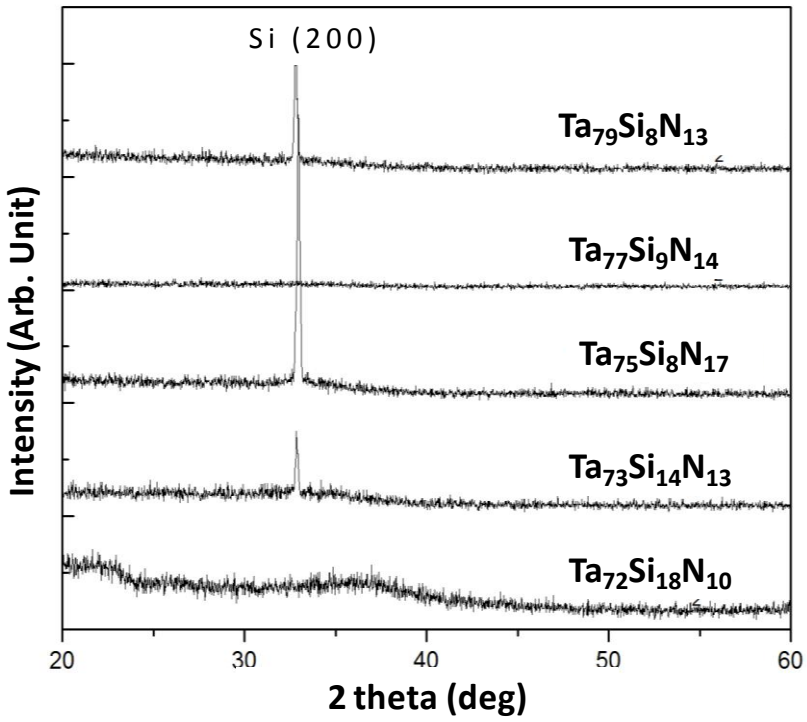

Fig. 4-4 XRD diffraction pattern of as-deposited Ta-Si-N /Si samples

4.3.4. Thermal stability

Samples of Ta-Si-N thin films were annealed at temperatures from 400 °C to 1000 °C. All films showed similar thermal stability. XRD diffraction patterns of $Ta_{77}Si_9N_{14}$/Si barrier of 8.5 sccm after annealing are shown in Fig. 4-5. At low temperature, all samples showed amorphous structure similar to the as-deposited state. The film lost the amorphous nature at 900 °C with the crystallization of Ta_2O_5. No $TaSi_x$ was observed. This indicates that the crystallization occurred before Ta reacted with Si in substrate, which is the same as in Ta-N films. As reported by most researchers Ta-Si-N barrier may fail by formation of nanocrystal [103] or Cu diffusion before crystallization [124].

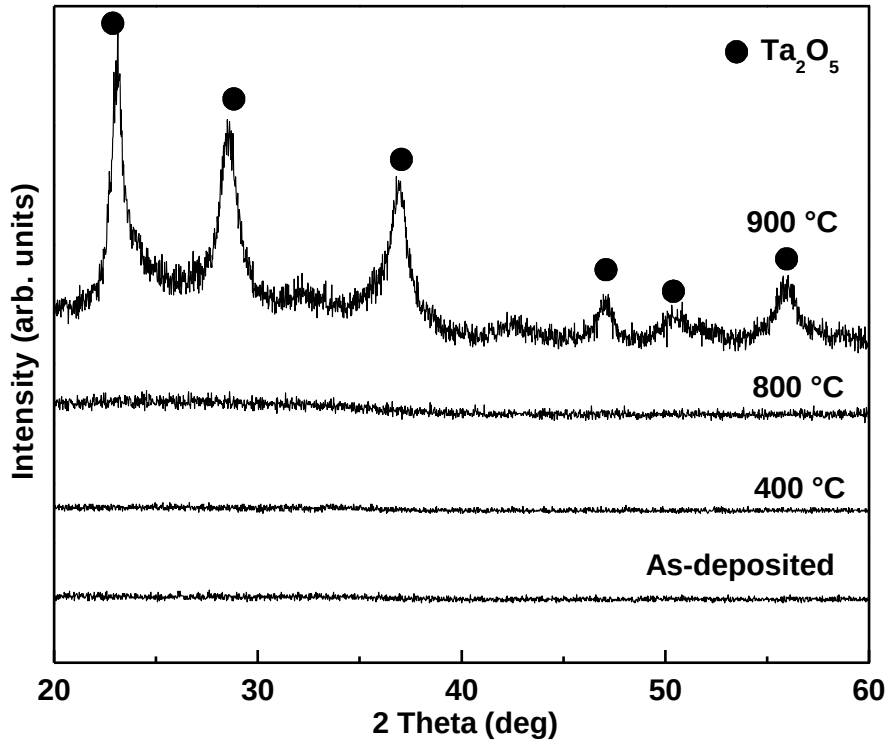

Fig. 4-5 XRD diffraction pattern of annealed $Ta_{77}Si_9N_{14}$

In order to further verify the formation of Ta_2O_5 nanocrystal, Ta-Si-N barrier annealed at 800 °C and 900 °C was observed under TEM (Fig. 4-6). It showed no observable nanocrystal at 800 °C and the existence of nanocrystalline (indicated by circle) at 900 °C. The crystallization temperature is lower than the reported 1100 °C [38] but still higher than Ta-N.

There have been a few studies discussing about the thermal stability of amorphous Ta-Si-N film. The high thermal stability was attributed to the co-existence of Ta-N, Si-N, and Si-N bonding. Some studies reported that the thermal stability of Ta-Si-N is higher with increased N concentration and Si/Ta ratio [99, 139]. Chung et al reported that Ta-Si-N formed at N_2 flow ratio lower than 10% showed amorphous phase while Ta-Si-N formed at N_2 flow higher than 20% showed polycrystalline phase. They attributed the amorphous structure to the distorted Ta-N and Ta-Si compound

embedded in amorphous Si-N compounds, and the crystalline structure to the TaN and Ta_2Si.

But it should be noted that these studies focused on the phenomena of the as-deposited film. The reason of the amorphous phase formation was either not explained or explained based on the XRD study, which only shows the crystalline phase formation. In our work we studied the chemical formation of Ta-Si-N, and reported the observation of Tantalum silicate Ta-Si-O [100]. The amorphous films were annealed up to the crystallization temperature. It is observed that higher amount of amorphous phase is maintained for films with higher Ta silicate concentration. Thus it is believed that the existence of Ta silicate is related to the high thermal stability. With existence of Ta silicate, higher activation energy is needed to decompose Ta-Si-O to form $TaSi_x$ and TaO_x. In the current work, the crystalline phases observed at high temperature are Ta_2O_5, which should be the product of Ta-Si-O decomposition.

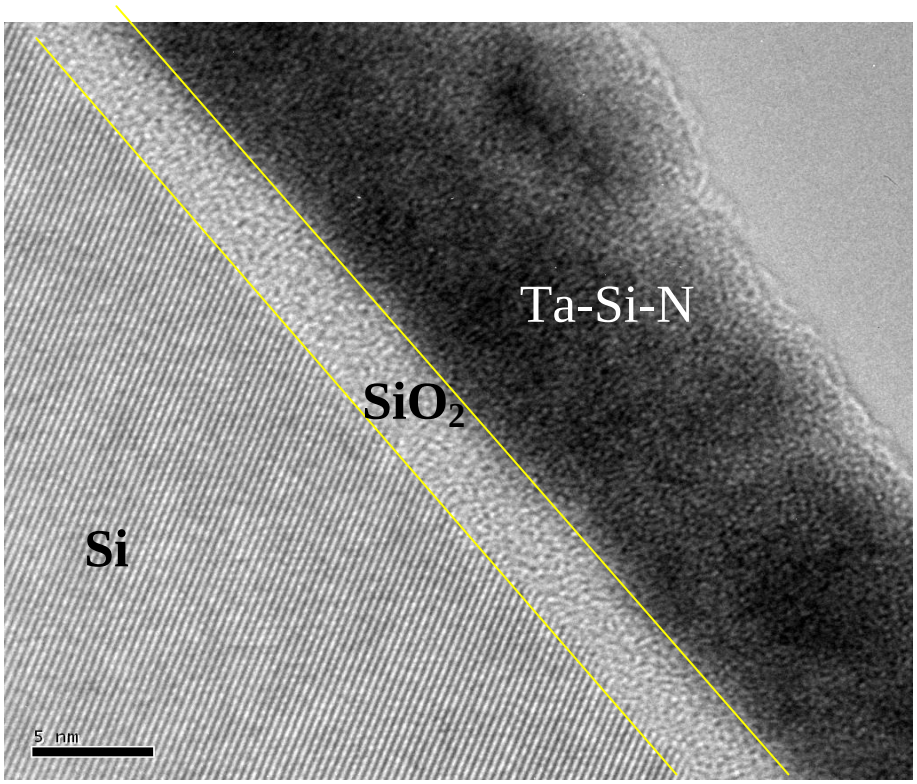

(a)

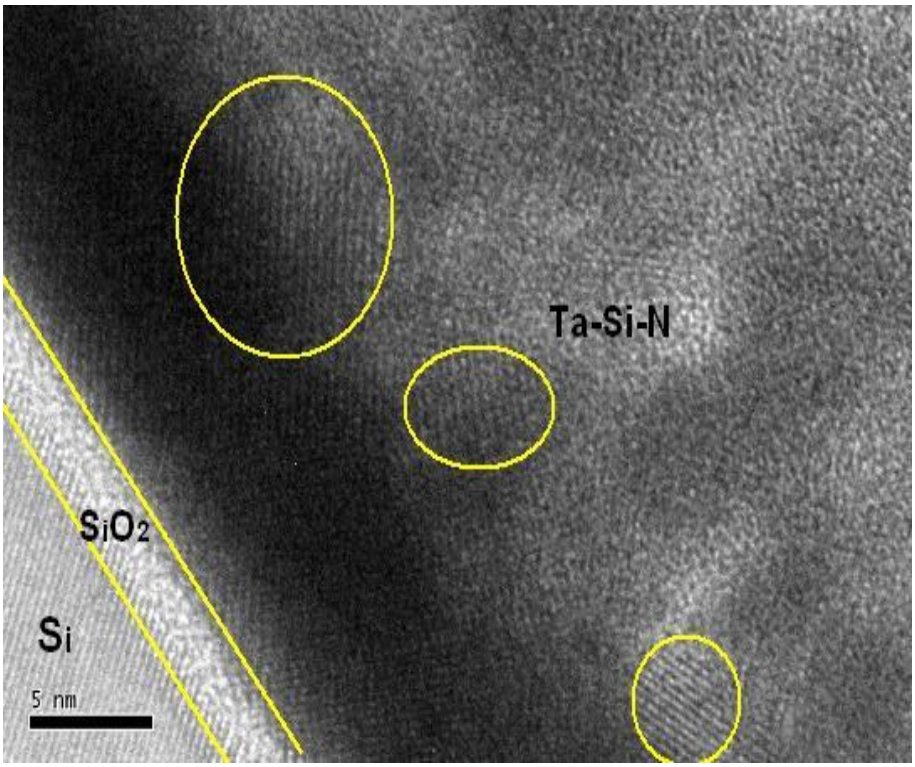

(b)

Fig. 4-6 HRTEM image for $Ta_{77}Si_9N_{14}$ barrier annealed in vacuum (a) at 800 °C, showing amorphous $Ta_{77}Si_9N_{14}$ film (b) at 900 °C, showing the Ta_2O_5 nanocrystals in $Ta_{77}Si_9N_{14}$ matrix.

4.4. Summary

Compositional, electrical, and microstructural properties of Ta-N and Ta-Si-N thin films are studied on as-deposited and annealed sample. Concentration of N and Si of thin films varied with deposition parameters. XPS study indicated the chemical formation of Ta, $Ta(ON)_x$ and Ta_2O_5 compounds in Ta-N thin films, and $TaSi_xO_y$, TaO_x, Ta_xN_y and $TaSi_x$ compounds in Ta-Si-N thin films. Ta-Si-N films have high resistivity and larger resistivity variation compared to Ta-N films. Both films showed as-deposited amorphous structure with high thermal stability. Ta-N films crystallized at 800 °C with Ta_2O_5 crystal growth. The temperature is higher than reported 600 °C to 700 °C [45]. Ta-Si-N films crystallized at 900 °C with Ta_2O_5 growth also, which is lower than the reported 1100 °C. The higher thermal stability of Ta-Si-N is attributed to the co-existence of multiple compounds.

In summary, amorphous Ta-N and Ta-Si-N thin film were formed by magnetron sputtering. Ta-Si-N showed higher thermal stability up to 900 °C, compared to 800 °C of Ta-N. Ta-Si-N also showed much higher electrical resistivity than Ta-N. It shows that the addition of non-metallic element in barrier system could enhance the thermal stability of the amorphous microstructure, with sacrifice of electrical conductivity. The barrier performance of Ta-N and Ta-Si-N systems will be studied in Chapter 6.

Chapter 5. Formation and Properties of Sputtered Ta-Ni, Ta-Cr, and Ta-Ti Thin Films on Si Substrate

During the exploration of Cu diffusion barriers, there have been many efforts to propose thin film barrier with good barrier performance and low electrical resistivity. As shown in Chapter 4, compounds films with higher complexity generally have better barrier performance, but with sacrifice of electrical resistivity. Compared to compound barriers, the binary metallic glass or amorphous alloy thin films are potentially better Cu diffusion barrier, because of their metallic nature with low resistivity and stable amorphous structure which is preferred as diffusion barrier.

In this part formation and properties of Ta based binary alloys (Ta-TM) are studied through theoretical and experimental methods. The glass formation ability of Ta-TM films is firstly estimated using size difference method and structural difference method. The prediction is then verified through experimental study on sputtered Ta-TM films on Si substrate. Three Ta-TM thin films, Ta-Ni, Ta-Cr, and Ta-Ti, will be studied.

5.1. Theoretical prediction of glass forming ability of Ta-TM alloys

Several empirical rules have been proposed to predict the glass forming ability (GFA) of binary metallic alloy system. Deep eutectic criterion, based on the equilibrium phase diagram, was developed by Tumbull's group [138]. It was widely used for the metallic glass formation prediction by liquid melt quenching. A simple and practical approach was proposed by Egami and Waseda, based on the atomic size difference of the alloying metals [139]. Liu et al. proposed the structural difference rule based on phase diagram, to predict the GFA and glass formation range (GFR) [140] . A

thermodynamic approach considering the formation enthalpy and formation energy, was also developed by Miedema [141].

It should be noted that, as the kinetic nature of alloy formation plays important roles in the glass forming tendency, these empirical rules may not be suitable in certain formation methods. Among these empirical rules, the atomic size difference rule and structural difference rule, which were developed based on experimental understanding from fast quenching and ion beam mixing, are therefore more relevant in understanding the thin film alloy formed by sputtering. Thus these two methods are applied to predict the GFA of the Ta-TM systems.

5.1.1. Size difference methods

As suggested by the Hume-Rothery rule, the critical concentration for a binary metal system A-B to form metallic glass could be estimated based on their atomic radii. Egami and Waseda examined more than 80 known binary metallic glass system, mostly produced by fast quenching from the melt, and concluded that the minimum concentration of metal B in matrix A, $C_B^{\min}$, following an empirical rule, as described by Equation 5.1 and 5.2 below [142]:

$$\frac{\Delta v}{v_A} = \frac{v_B - v_A}{v_A} = \left(\frac{r_B}{r_A}\right)^3 - 1 \qquad (4.1)$$

So that

$$\left|\lambda_0\right| = C_B^{\min}\left|\frac{\Delta v}{v_A}\right| \approx 0.1 \qquad (4.2)$$

Table 5-1 GFR predicted by size difference rule for Ta-Ni, Ta-Cr and Ta-Ti (atomic radii taken from Egami and Waseda's work [142]

System	Atomic radius (Å)	GFR
Ta-Ni	Ta: 1.49	27.3 at% - 82.3 at% (Ni)
	Ni: 1.28	
Ta-Cr	Ta: 1.49	29.8 at% - 80.2 at% (Cr)
	Cr: 1.30	
Ta-Ti	Ta: 1.49	No GFR
	Ti: 1.46	

where r_A and r_B are the atomic radius of A and B, V_A and V_B are the atomic volume of A and B， Δv is the volume difference， $C_B^{\min}$ is the minimum atomic concentration of B in A, and λ_0 is the size factor. It reveals the empirical rule, that a minimum total volume mismatch of ~10% is necessary for binary metallic glass formation. Based on this rule, $C_A^{\min}$ and $C_B^{\min}$ could be estimated based on atomic radius of A and B as in equation 5.3 and equation 5.4:

$$C_A^{\min} = \frac{0.1R_B^3}{\left|R_A^3 - R_B^3\right|} \tag{4.3}$$

$$C_B^{\min} = \frac{0.1R_A^3}{\left|R_A^3 - R_B^3\right|} \tag{4.4}$$

They provide a guideline for calculation of the glass GFR for A-B alloy. It should be noted that the atomic radii of metals are dependent on the composition of the alloys. The atomic radii used in Egami and Waseda's work were calculated from metallic closed packed structure, so is current study. The GFR of Ta-Ni, Ta-Cr, and Ta-Ti can

be estimated as in Table 5-1. It is noted that Ta-Ni and Ta-Cr have a broad GFR. However, the Ta-Ti shows unrealistic GFR.

5.1.2. Structural difference method

The structure difference rule, as proposed by Liu et al. [141], indicates that the binary alloys with constitute metals of different structures are more likely to form amorphous alloy, with the composition at the midpoint of the two-phase region. They also proposed a maximum possible amorphous range (MPAR) for such system (Fig. 5-1).

As shown in the phase diagram (Fig. 5-2), multiple intermetallic compounds exist for Ta-Ni system. It indicates that Ta and Ni have a broad range of MPAR. Similarly, for Ta-Cr, the calculated phase diagram shows that two phase region exists in a large atomic composition. It suggests that Ta-Ni and Ta-Cr may possess good GFA. However, for Ta-Ti, as seen from phase diagram, there is no formation of intermetallic compounds between Ta and Ti. Instead, they form two distinct crystalline phases.

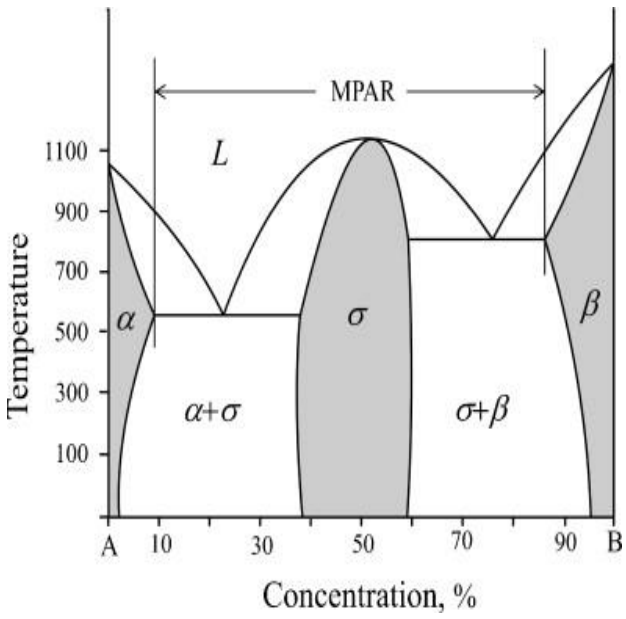

Fig. 5-1 Definition of the maximum possible amorphorization range (MPAR).[143]

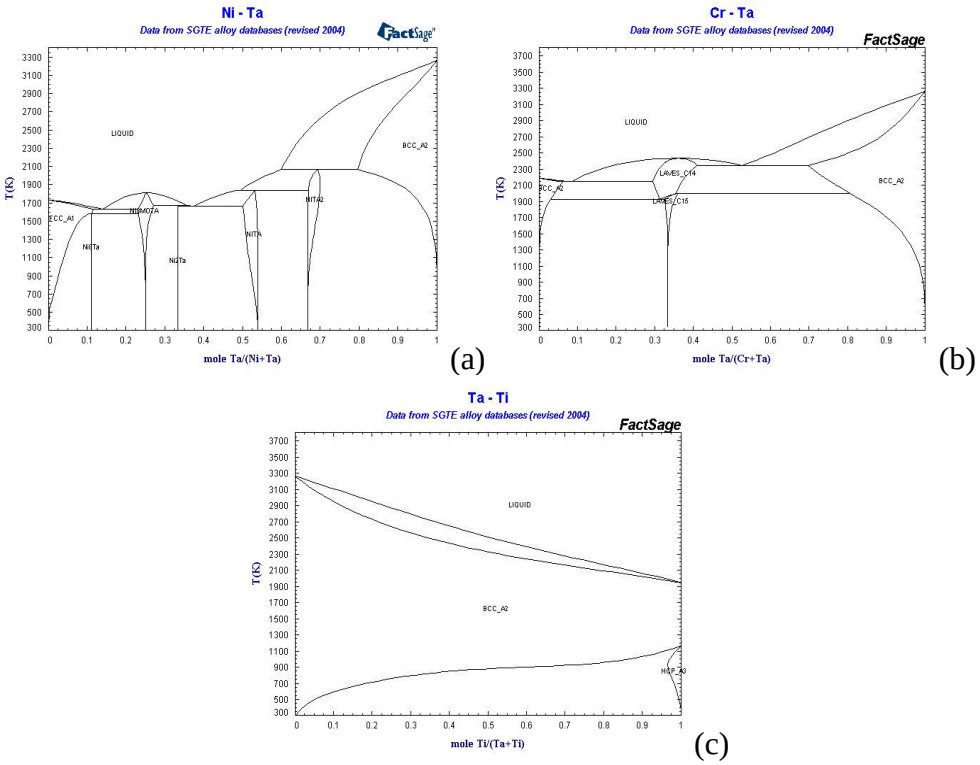

Fig. 5-2 Phase diagram of (a) Ni-Ta; (b) Cr-Ta; and (c) Ti-Ta

5.1.3. Summary

As discussed above, both size difference method and structural difference method suggests that, Ta-Ni and Ta-Cr are good glass forming alloys, but Ta-Ti does not possess good GFA.

Therefore in the following part, Ta-Ni, Ta-Cr, and Ta-Ti thin films will be studied to understand the properties, especially the amorphous film formation ability and the stability.

5.2. Experimental study of Ta-TM thin films on Si substrate

5.2.1. Ta-Ni/Si

5.2.1.1. Effect of process control on the composition and properties of Ta-Ni film

Table 5-2 shows the composition, the electrical resistance, and the deposition rate of the films at different sputtering power setting for Ta and Ni. The atomic compositions of the films were dependent on the power supply type and the power setting. DC power shows higher efficiency compared to RF power. The highest Ta content of 93 at% was obtained when Ta target of 200 W DC and Ni target of 200 W RF were applied while the highest Ni content of 60.01 at% was obtained when Ta target of 200 W RF and Ni target of 150 W DC were applied. Increase of the power on one target will result in higher atomic percentage of this metal, such as in case of $Ta_{51}Ni_{49}$ and $Ta_{40}Ni_{60}$. It shows that, by changing the power type and adjusting the power setting of this RF/DC magnetron sputtering system, binary alloy thin films with a relatively large composition range can be deposited, and thus can be applied in other works requiring a wide composition range. It needs to be mentioned that a certain amount of O was also observed in the films, and will be discussed in details in Chapter 7, thus it is not included in the discussion of this part.

Table 5-2 Composition, electrical resistance and deposition rate at different sputtering power of Ta and Ni

Ta power (W)	Ni power (W)	Composition (at%)	Electrical resistivity (μΩ·cm)	Deposition rate (nm/sec)	Annotation
200 W DC	200 W RF	Ta: 92.53 Ni: 7.47	447.76	14.72	$Ta_{93}Ni_7$
300 W RF	50 W DC	Ta: 68.09, Ni: 31.91	225.60	12.67	$Ta_{68}Ni_{32}$
200 W RF	100 W DC	Ta: 51.02, NI: 48.98	193.20	14.98	$Ta_{51}Ni_{49}$
200 W RF	150 W DC	Ta: 39.90 Ni: 60.01	164.51	17.31	$Ta_{40}Ni_{60}$

In the studied composition range, the electrical resistivity of Ta-Ni films ranged from 164.51 μΩ·cm to 447.76 μΩ·cm (Table 5-2). The resistivity was dependent on Ta and Ni composition. It showed a linear relationship with respect to the film composition. When the Ni concentration increased, the electrical resistance reduced. The resistivity is higher than that of Ta (15-60 μΩ.cm for α phase and 170-210 μΩ·cm for β phase [145]) and Ni (69.3 μΩ·cm). As it was known that the sputtered Ta film usually has β phase, it is not surprised to see Ta-Ni resistivity in range of hundreds μΩ·cm. The higher electrical resistivity of Ta-Ni compared to Ta and Ni is mainly attributed to the amorphous microstructure of the as-deposited film, while the existence of O in the film may further increase the resistivity. Oxygen also increases the electrical resistivity, as will be discussed later.

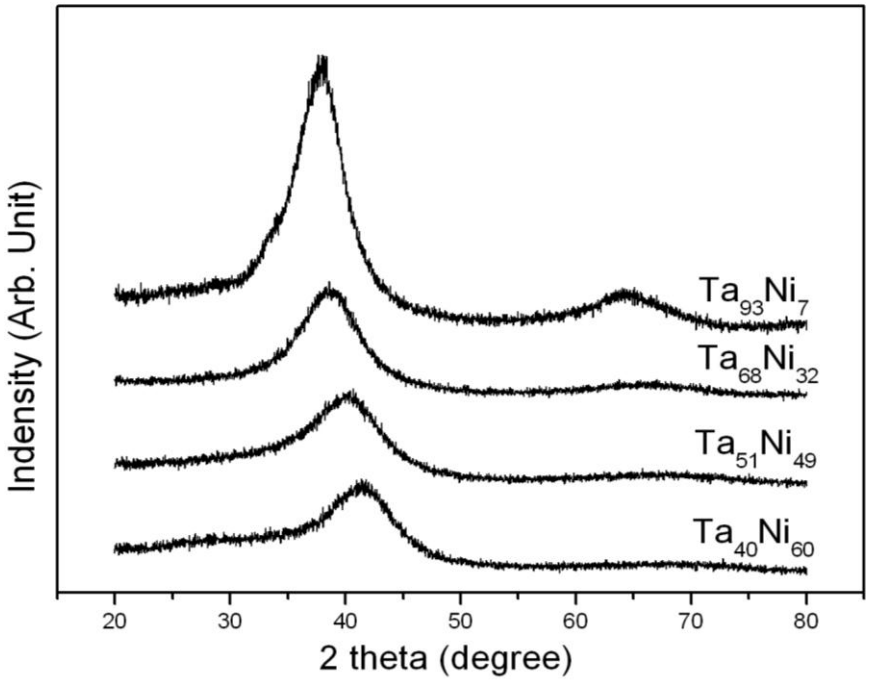

Fig. 5-3 XRD diffraction pattern of as-deposited Ta-Ni films with different composition

It should be pointed out that compared to the resistivity of Ta-N and Ta-Si-N, the resistivity of Ta-Ni films is relatively lower. The low resistivity enables Ta-Ni to be used in semiconductor process without significant increase of RC delay.

The as-deposited microstructures of Ta-Ni films were studied using XRD and shown in Fig. 5-3. A broad amorphous peak was observed for all films. Generally, as proposed by Inoue, binary metallic alloys do not have high glass forming ability (GFA) [144]. In order to form amorphous phase for binary alloy, a very fast quenching rate at 10^{14} degree/second needs to be achieved. In the case of PVD deposition, the fast adsorption process can be regarded as a very fast quenching process from gas precursor to solid phase transition. As the atoms are adsorbed on substrate at room

temperature, the kinetic energy of sputtering atomic is so low that movement of atoms in favor of crystalline phase formation is largely suppressed.

It was also noted that the peak of the amorphous peak shifted from 38.2° to 42.2° as the Ni percentage increased. As the amorphous peak represents the first order inter-atomic distance in the amorphous system, it is believed that the shift to right shows the reducing of average inter-atomic spacing in the amorphous system. It is expected as Ni shows small atomic size compared to Ta, thus higher percentage of Ni results in smaller first order inter-atomic spacing.

As a summary, amorphous phase was obtained for Ta-Ni thin films deposited by co-sputtering methods in a relatively large composition range. The average inter-atomic spacing of the amorphous system became smaller as Ni concentration increases. The films showed low resistivity compared to Ta-N films.

5.2.1.2. Thermal stability of Ta-Ni films

XRD scanning showed that all films remained amorphous after annealing at 700 °C for 30 min (Fig. 5-5). It shows higher stability than the previous report on Ta/Si by Min et al that Ta and Si react at 650 to form $TaSi_2$ [58]. It might be due to different deposition situation.

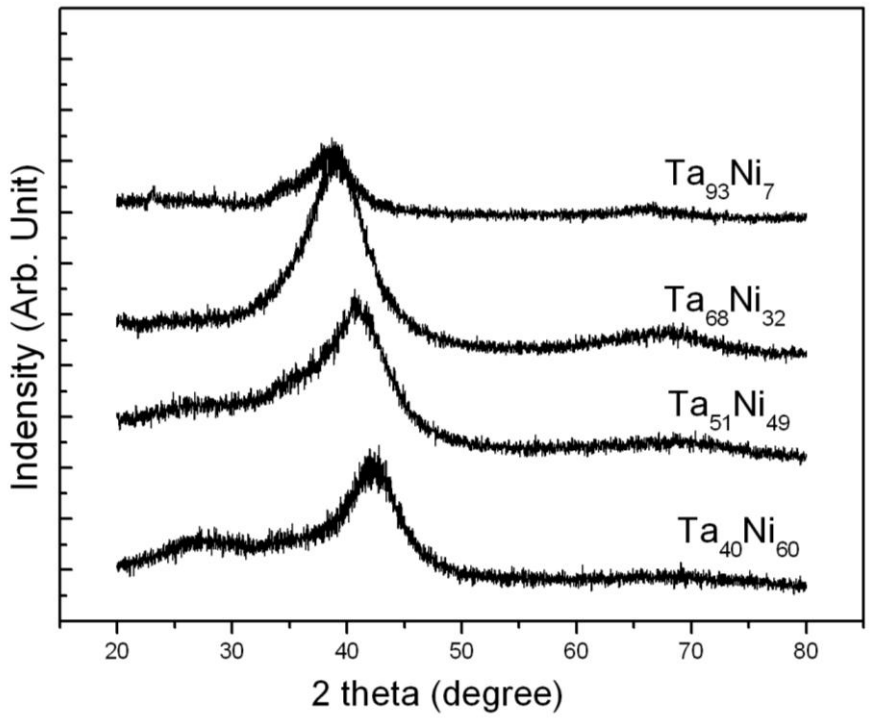

Fig. 5-5 XRD diffraction pattern of Ta-Ni/Si films annealed in vacuum at 700 °C

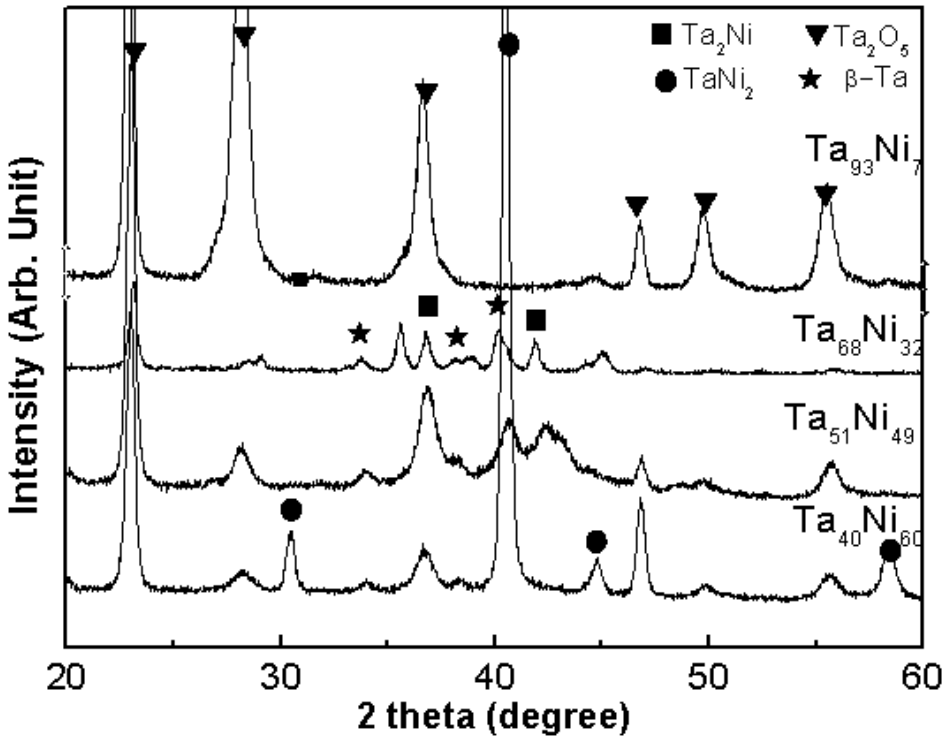

Fig. 5-4 XRD diffraction pattern of Ta-Ni films annealed in vacuum at 800 °C

Fig. 5-4 shows the XRD plot of all films annealed at 800 °C. Multiple crystalline phases appear for all the films as indicated. β-Ta were found in all films except $Ta_{93}Ni_7$ probably due to the large amount of Ta_2O_5 in $Ta_{93}Ni_7$. Two Ta-Ni phases, Ta_2Ni and $TaNi_2$, were identified. It seems that the stoichiometry of the Ta-Ni phase is dependent on the atomic ratio. In $Ta_{68}Ni_{32}$ and $Ta_{51}Ni_{49}$, Ta_2Ni and β-Ta were present, while in $Ta_{40}Ni_{60}$, $TaNi_2$ and β-Ta were identified. In $Ta_{93}Ni_7$, relatively large amount of Ta_2O_5 was observed, which shows severe reaction between Ta and O. The fast reaction is due to the fact that Ta is an oxygen getter, which has high formation of energy of -2045.98 kJ/mol. There was also Ta_2O_5 with lower percentage in other three films. There was no reaction at barrier and Si interface when crystallization started, indicating a high interface stability. It is noted that in current work there was no silicide formation when the Ta-Ni films crystallized. It shows high interface stability between barrier and Si

5.2.1.3. Summary

Ta-Ni films with a large composition range were deposited on Si substrate. All films are amorphous, with smaller first-order inter-atomic spacing for higher Ni concentration. The electrical resistivity showed small variation with composition, and it reduced as Ni concentration increased. The films remained amorphous until annealed in vacuum at 800 °C for 30 min. Multiple crystalline phases such as Ta_2O_5, β-Ta, Ta_2Ni and $TaNi_2$ appeared at 800 °C, showing stability similar as Ta-N thin films. No interface reaction between Si and Ta-Ni films were observable when crystallization started.

Table 5-3 Composition and electrical resistivity of Ta-Cr films deposited at different targets power

Ta power (W), RF	Cr power (W), DC	Composition	Electrical resistivity (μΩ·cm)	Annotation
200	100	Ta: 61.70 at% Cr: 38.30 at%	232.74	$Ta_{62}Cr_{38}$
200	80	Ta: 67.40 at% Cr: 32.60 at%	285.16	$Ta_{67}Cr_{33}$
200	50	Ta: 76.07 at%, Cr: 23.93 at%	222.95	$Ta_{76}Cr_{24}$
200	30	Ta: 90.62 at% Cr: 9.38 at%	317.46	$Ta_{91}Cr_{9}$

5.3. Ta-Cr/Si

5.3.1.1. Effect of process control on the composition and properties of Ta-Cr film

As shown in Table 5-3, when the power applied on Ta and Cr power changed, Ta-Cr films with Cr of 9.38 at% to 38.30 at% were deposited, with resistivity from 222.95 μΩ·cm to 317.46 μΩ·cm. The resistivity range is comparable with that of Ta-Ni. Similar as Ta-Ni, the effect of power type and power setting on the film composition was observed. Different from Ta-Ni, there is no obvious correlation between the composition and resistivity.

Fig. 5-6 shows the XRD plot of all the deposited films. Similar as Ta-Ni films, all deposited Ta-Cr films are amorphous. All films showed amorphous peak centering at 39.0°, which is close to the amorphous peak of α-Ta. It is different from the finding in

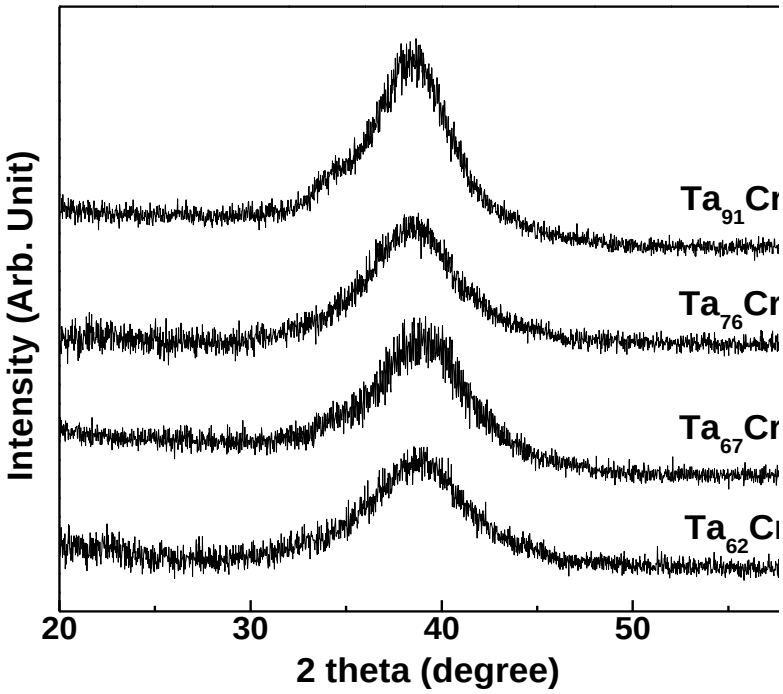

Fig. 5-6 XRD diffraction pattern of as-deposited Ta-Cr films with different compositions

Ta-Ni study, that an amorphous peak shift to right was observed with the increase of Ni content.

5.3.1.2. Thermal stability of Ta-Cr films

The Ta-Cr films were annealed in vacuum for 30 min at 600 °C, 700 °C and 800 °C respectively before they were scanned through XRD. The XRD plot shows that the films remained amorphous at 700 °C (Fig. 5-7). Fig. 5-8 shows that crystallization started for all films at 800 °C with formation of Ta_2O_5 crystalline phase. For $Ta_{91}Cr_9$, α-Ta (110) was observed at 800 °C. The observation of α-Ta (110) is attributed to the high percentage of Ta in $Ta_{91}Cr_9$ film. There was no reaction at Ta-Cr and Si interface, which shows same finding as in Ta-Ni study.

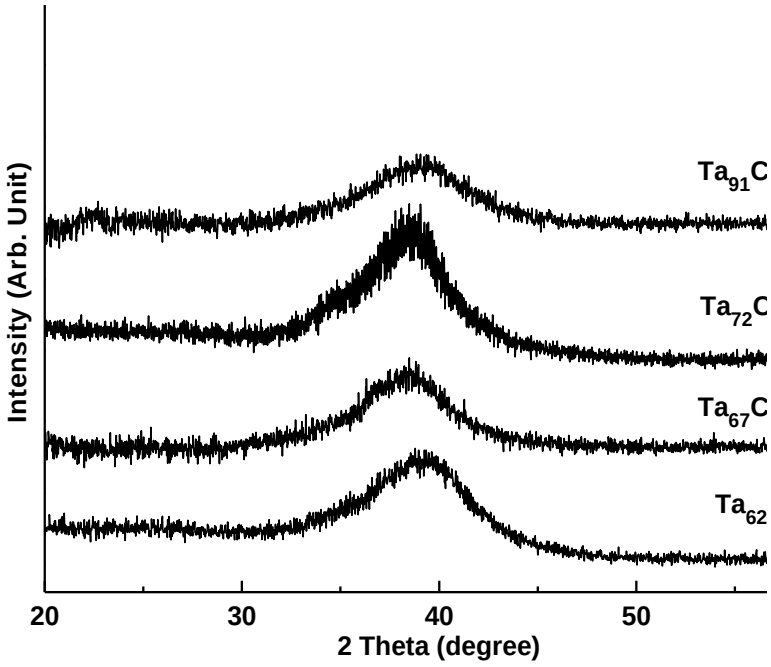

Fig. 5-7 XRD diffraction pattern of Ta-Cr/Si films annealed in vacuum at 700 °C

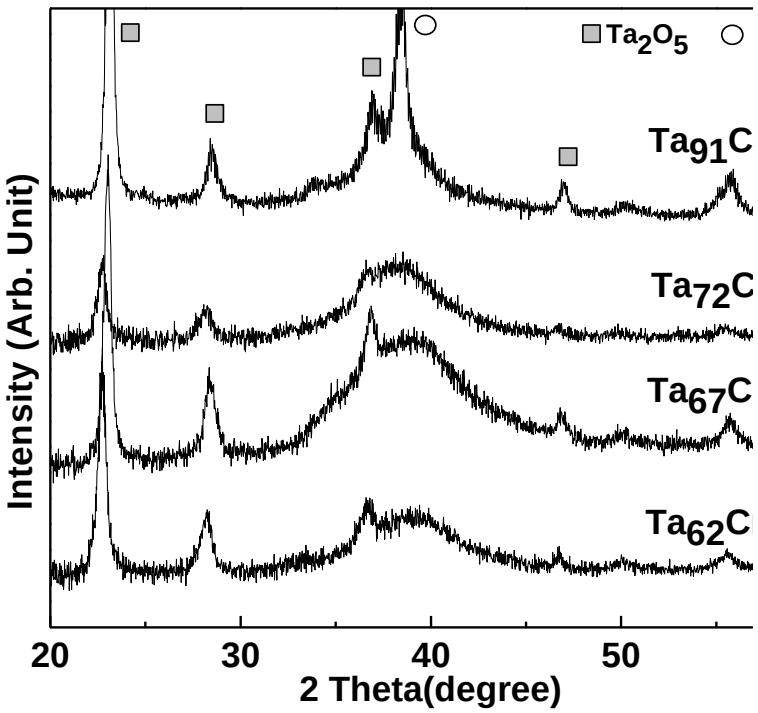

Fig. 5-8 XRD diffraction pattern of Ta-Cr films annealed in vacuum at 800 °

Table 5-4 Film composition and electrical resistivity for Ta-Ti/Si

Ta power RF (W)	Ti power DC (W)	composition	Electrical resistivity (μΩ·cm)	Annotation
200	30	Ta: 93.7 at% Ti: 6.3 at%	445.5	$Ta_{94}Ti_6$
200	50	Ta: 86.7 at% Ti: 13.3 at%	407.8	$Ta_{87}Ti_{13}$
200	80	Ta: 78.4 at% Ti: 21.6 at%	438.9	$Ta_{78}Ti_{22}$
200	100	Ta: 75.2 at% Ti: 24.8 at%	505.3	$Ta_{75}Ti_{25}$

5.3.1.3. Summary

Ta-Cr films deposited by sputtering showed stable amorphous phase at all studied compositions. Crystallization occurred for all films after they were annealed at 800 °C for 30 min. It shows that Ta-Cr films formed by sputtering could result in stable amorphous thin films.

5.3.2. Ta-Ti/Si

Ta and Ti have been widely used in semiconductor industry. Ta and Ta-N are used as Cu diffusion barrier, while Ti and Ti-N have been applied as Al diffusion barrier in Al metallization and W diffusion barrier in Cu metallization. Thus a study of Ta-Ti alloy thin film as Cu diffusion barrier is attractive. To our disappointment, Ta-Ti seems have poor GFA as predicted from both size difference rule and structural difference rule.

But it is still important to study the Ta-Ti films, in order to verify the theoretical prediction, and to provide a reference for future study..

5.3.2.1. Effect of process control on the composition and film properties of Ta-Ti film

As shown by Table 5-4, the films with Ti concentration ranging from 6.3 at% to 24.8 at% were deposited with the change of power supply. Apparently, the Ti concentration increases as the Ti power increases. Compared to that of Ta-Ni and Ta-Cr, it should be noted that even at the same power setting, the atomic concentration of the films are different. It is attributed to the different sputtering yield for Ta, Ni, Cr and Ti.

The XRD graphs of all films are shown in Fig. 5-9. Different from Ta-Ni and Ta-Cr films, all Ta-Ti films showed two nanocrystalline peaks. The peak positions are close to (002) peak of β-Ta and (110) peak of α-Ta which are usually observed for sputtered Ta film. As discussed in section 4.1, the atomic size difference between Ta and Ti is not sufficient to promote amorphous phase formation. Therefore they will form distinct crystalline phase instead of amorphous phase. Because Ti (002) peak and α-Ta (110) peak are both close to 28.0 °, it is difficult to distinguish the two.

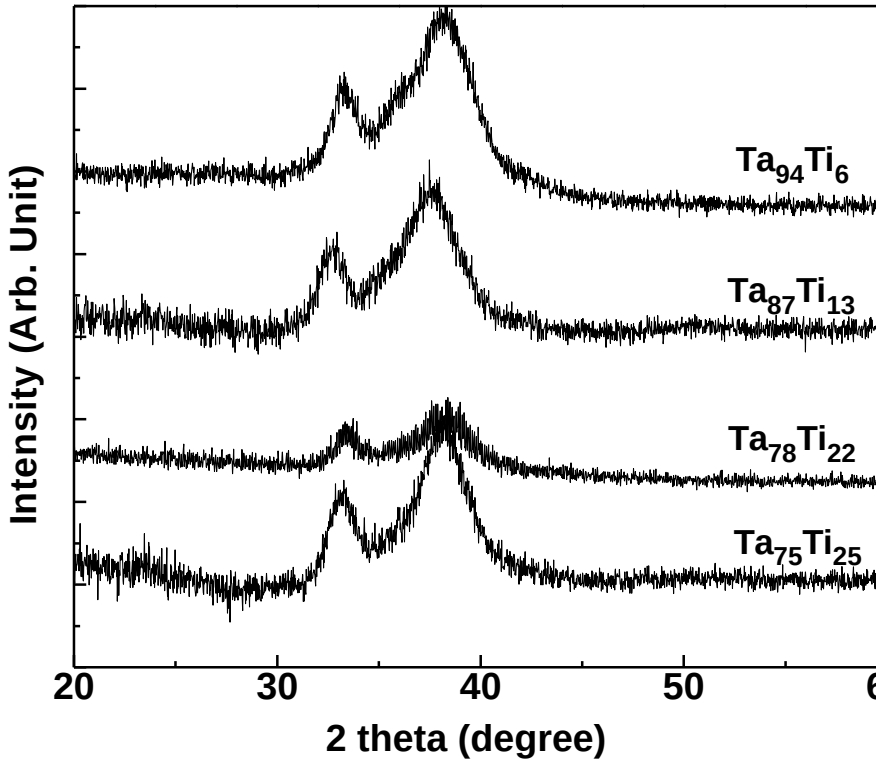

Fig. 5-9 XRD diffraction pattern of as-deposited Ta-Ti films with different composition

5.3.2.2. Thermal stability of Ta-Ti films

XRD diffraction patterns of the films annealed are shown in Fig. 5-10. For all the films, an amorphous peak replacing Ta and Ti peaks were observed after 600 °C annealing, indicating the occurrence of a solid amorphization. The formation of the amorphous phase is an intermediate stage with the phase transformation from beta-Ta to alpha-Ta at 600 °C. At 700 °C, Ta-rich $Ta_{94}Ti_6$ and $Ta_{87}Ti_{13}$ remained amorphous, while $Ta_xTi_{1-x}O_2$ crystalline peaks appeared for $Ta_{78}Ti_{22}$ and $Ta_{75}Ti_{25}$. At 800 °C, Ta_2O_5 peaks grew in $Ta_{94}Ti_6$, and $Ta_xTi_{1-x}O_2$ peaks grew in $Ta_{87}Ti_{13}$. For $Ta_{78}Ti_{22}$ and $Ta_{75}Ti_{25}$, $Ta_xTi_{1-x}O_2$ peak remained. It shows that with higher Ti content, the formation of $Ta_xTi_{1-x}O_2$ is triggered at a lower temperature. While for Ta-rich $Ta_{94}Ti_6$ and

$Ta_{87}Ti_{13}$, the crystallization is at a higher temperature. Thus in order to maintain the amorphous structure with higher temperature, the composition of Ta-Ti has to be carefully controlled.

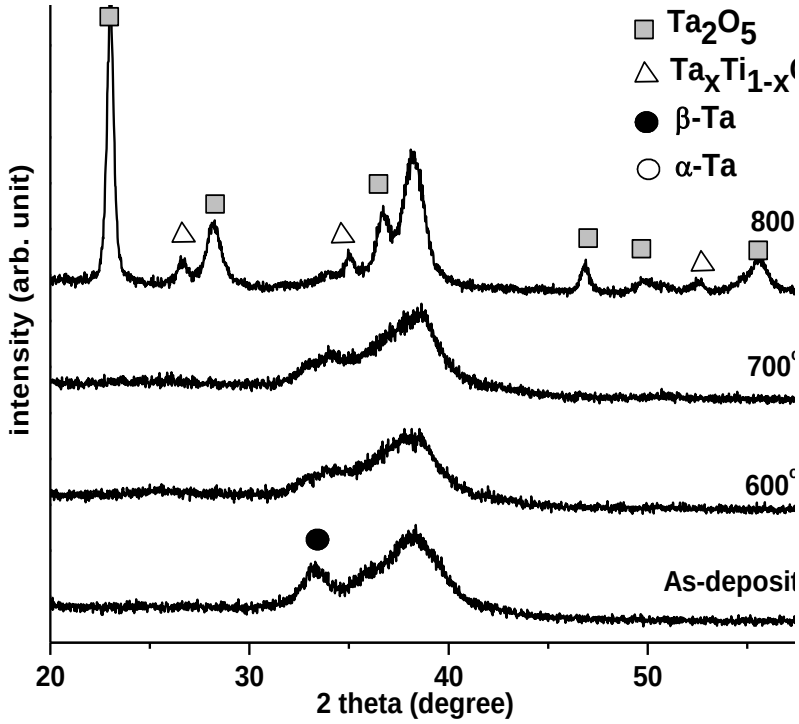

(a)

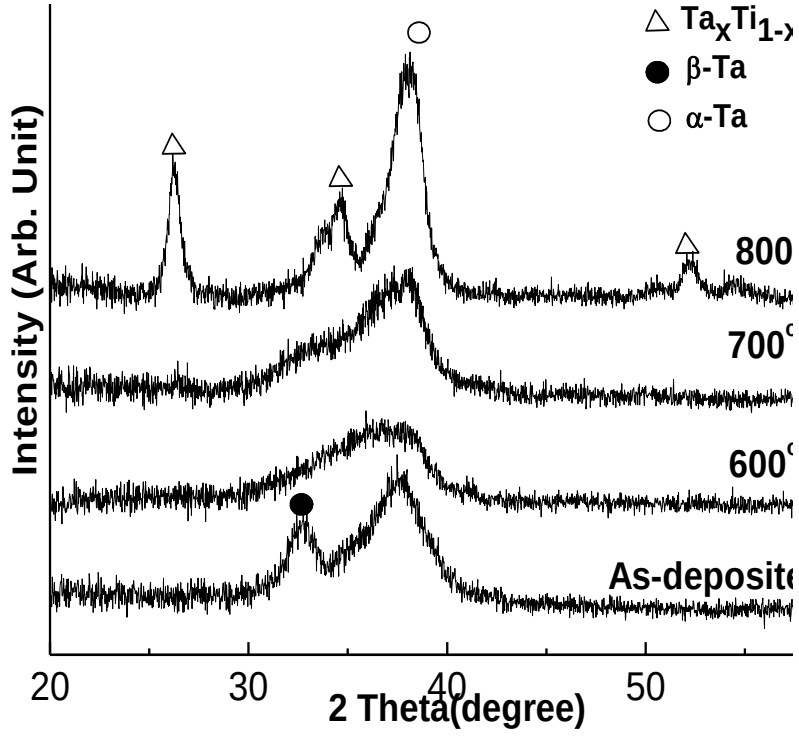

(b)

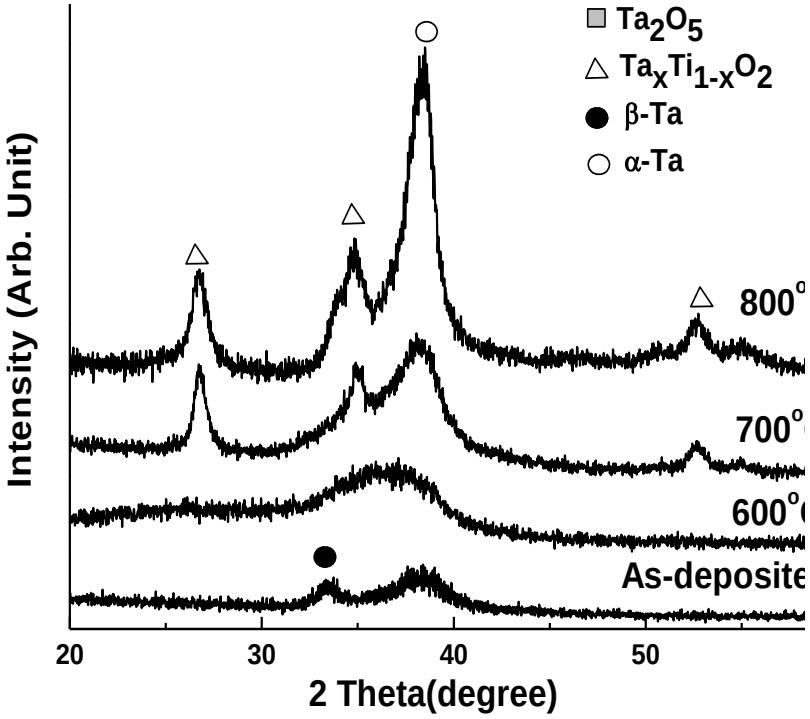

(c)

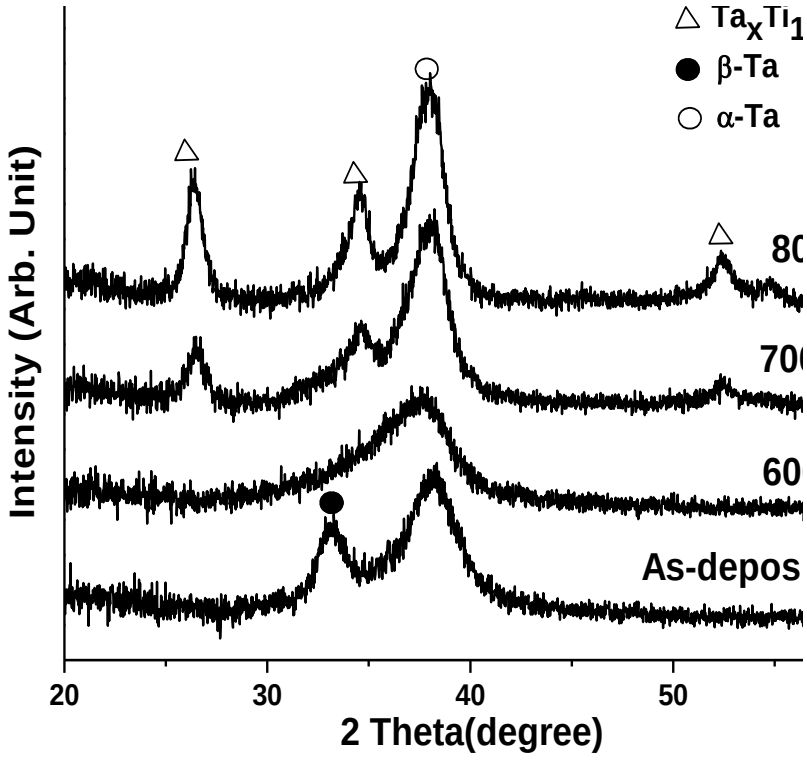

(d)

Fig. 5-10 XRD diffraction pattern of Ta-Ti films with different composition annealed in vacuum at 600 °C to 800 °C: (a) $Ta_{94}Ti_{6;}$ (b) $Ta_{87}Ti_{13}$; (c) $Ta_{78}Ti_{22;}$ (d) $Ta_{75}Ti_{25}$

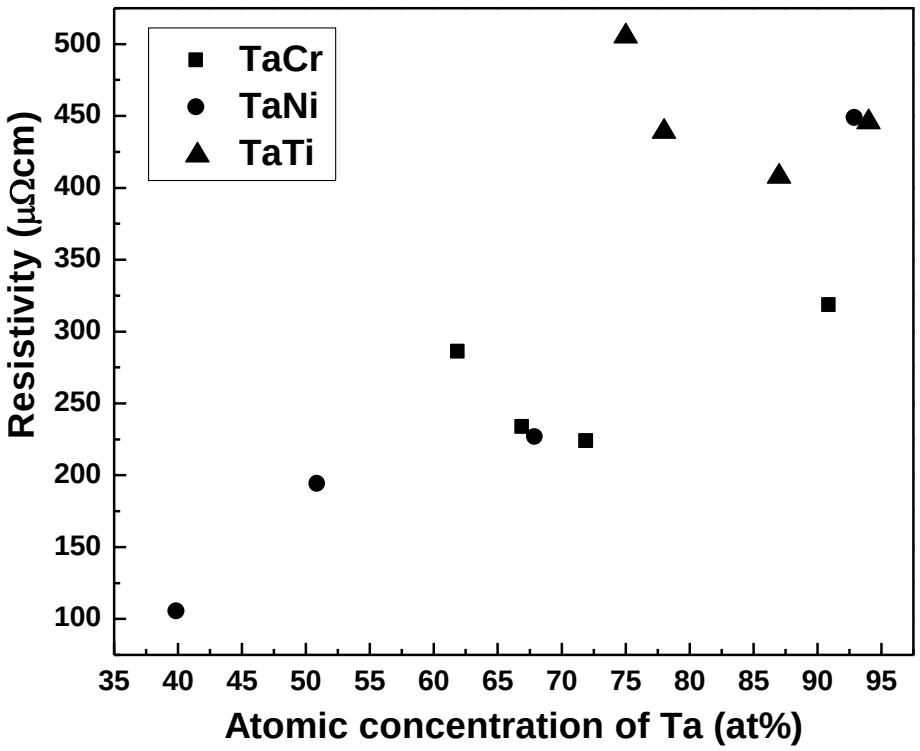

Fig. 5-11 Electrical resistivity of Ta-Ni, Ta-Cr and Ta-Ti thin films

5.3.3. Discussion

5.3.3.1. Electrical resistance and thermal stability of amorphous binary Ta-TM thin films

As-deposited electrical resistivity of the films with different composition is shown in Fig. 5-11. Ta-Ti and Ta-Cr films have a smaller variation compared to Ta-Ni films, which shows broader range of resistivity. As shown by the phase diagram, while Ta and Ni have a few intermetallic compounds, Ta and Cr only form intermetallic compound with narrow composition range, and Ta and Ti form distinct crystalline phases.. Therefore, the electron distribution in Ta-Cr and Ta-Ti does not show much change when the composition changes, while chemical bonding in Ta-Ni is strongly dependent on the composition changes, which results in resistivity change.

Resistivity in Ta-TM films are relatively low compared to Ta-N and Ta-Si-N. When the composition changes, the resistivity change is in a small range. It is smaller than the sputtered Ta-N which shows resistivity from 132 to 1.4 × 10^5 μΩ·cm [14], and Ta-Si-N which shows resistivity from 772 to 19760 μΩ·cm as studied in Chapter 4. Therefore, the composition window of Ta-TM films is larger compared to the other two barriers. In the current composition range for Ta-Cr and Ta-Ti, the resistively shows a decreasing trend first, and followed by an increasing trend with the increase of Ta composition. This is because the density of Ta structure is low when it is in as-deposited state. At higher percent of Cr or Ti percentage, the metallic atoms filled in the grain boundaries and vacancies. It will make the electron motion easier, and it further reduces the film resistivity.

5.3.3.2. Mechanism of amorphous Ta-TM alloy formation with different alloying elements

From the theoretical and experimental study, Ta-Ni and Ta-Cr were found to have a broad glass forming range, while Ta-Ti showed crystalline phase for the as-deposited state. The amorphization effect of Ni and Cr are more obvious with higher Ni and Cr concentration, as in the Ta-rich $Ta_{91}Ni_9$ and $Ta_{86}Cr_{14}$, the tiny humps of α-Ta and β-Ta were still observable, while in all films with higher Ni and Cr concentration, only one amorphous hump were observed. The good GFA of Ta-Ni and Ta-Cr is attributed to the different atomic size and different microstructure of the elements. On the other hand, for Ta-Ti film, the as-deposited films showed two crystalline phases belonging to Ta and Ti. Interestingly, amorphization is observed in Ta-Ti after annealing at 600 °C when the metastable β-Ta transfers to stable α-Ta. It further proves the importance of the structural difference for forming amorphous binary alloy.

The amorphous films formed by sputtering are meta-stable, because the amorphization is mainly caused by the hindering effect of the alloying element. With existence of alloying element, higher energy is required for the system to crystallize, as the energy barrier for crystallization has increased. The mechanism is illustrated in Fig. 5-12. The activation energy for crystallization is much higher than Ta because of the existence of the alloying element. Thus for as-deposited film, Ta films usually show crystalline phase as the kinetic energy of Ta atoms are high enough to overcome the barrier to crystallize, while the Ta-TM films show amorphous phase as the activation energy to crystallize is much higher than the kinetic energy of the atoms. The amorphization of the alloying elements is a result of kinetic factor rather than thermodynamic effect. When the films go through high temperature annealing, the atoms gain enough kinetic energy to overcome the energy barrier, and transform into thermodynamically more stable crystalline phase.

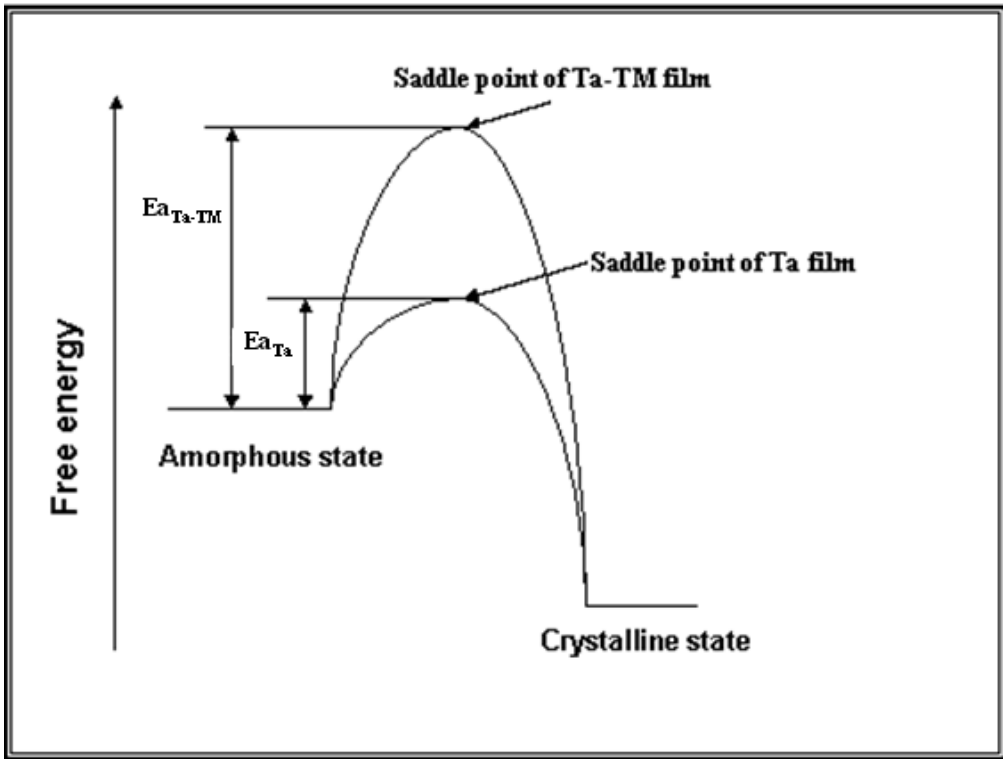

Fig. 5-12 Mechanism of metallic glass formation of Ta-TM alloy

It is also noted that the crystallization behaves differently when the film composition changes. During crystallization, multiple crystalline peaks appeared simultaneously. It shows the formation of one crystalline phase could be triggered by other crystalline phase formation.

5.4. Summary

This chapter studies the properties of Ta-TM films formed by sputtering of Ta and transition metal (Ni, Cr, and Ti) targets with different compositions. Based on the size difference method and structural difference method, it was predicted that Ta-Ni and Ta-Cr are good glass forming alloys, while Ta-Ti is not. The prediction was confirmed by experiments. Ta-Ni and Ta-Cr had amorphous structures with large composition

range before annealing. It is due to the kinetic effect of Cr and Ni that hinders Ta crystallization. These amorphous films were stable up to 800 °C with the crystallization of Ta_2O_5, $TaNi_x$ and β-Ta for Ta-Ni and α-Ta and Ta_2O_5 for Ta-Cr. For Ta-Ti, distinct Ta and Ti phases are observed. Solid phase amorphization was observed for Ta-Ti at 600 °C when the β-Ta transforms to α-Ta. In Ta-Ti with high Ti concentration, the amorphous films crystallize at 700 °C with $TaTiO_2$ phase observed. In Ta-Ti film with low Ti concentration, the crystallization occurred at 800 °C with formation of Ta_2O_5 and $TaTiO_2$ crystalline phases.

As a summary, sputtered Ta-Ni, Ta-Cr and Ta-Ti thin films have low resistivity compared to Ta-N and Ta-Si-N. Ta-Ni and Ta-Cr are amorphous film with high thermal stability, thus potentially good Cu diffusion barrier. Ta-Ti is crystalline when deposited, but a thermal treatment at 600 °C transfers it to amorphous phase thus it is worth studying as Cu diffusion barrier. In order to form binary amorphous alloy, the constituent elements need to have different atomic size and different microstructures.

Chapter 6. Cu Diffusion Barrier Performance of Ta-based thin films

As reviewed in Chapter 2, Ta based thin films are expected to be good Cu diffusion barriers. It is because material with high melting point like Ta is expected to be a good barrier for Cu diffusion. In Chapter 3 and Chapter 4, we have studied the formation and properties of Ta-based compounds such as Ta-N and Ta-Si-N and binary alloys such as Ta-Ni, Ta-Cr and Ta-Ti, respectively. Most of the sputtered films have shown good glass forming ability (except Ta-Ti) and low electrical resistivity (except Ta-Si-N). These films with amorphous structure are thus expected to have enhanced Cu diffusion barrier performance, as they practically eliminate grain boundaries which exist in poly-crystalline barriers and act as fast Cu diffusion path.

Therefore, to evaluate the Cu diffusion barrier performance of these films, experiments were carried out to study the Cu diffusion in these films and the failure mechanism of the barriers at elevated temperature. The studied barriers include Ta, Ta-N, Ta-Si-N, Ta-Ni, Ta-Cr, and Ta-Ti film.

6.1. Diffusion barrier performance of Ta, Ta-N and Ta-Si-N on Si substrate

Ta/Ta-N bi-layer is not a new barrier candidate, as it has been applied in industrial production as a successful Cu diffusion barrier. It should be pointed out that while Ta-N has shown promising barrier performance, Ta itself is not a good Cu diffusion barrier, due to its tendency to form polycrystalline phase. It has been reported that a 25 nm Ta barrier remains effective Cu barrier on P^+-N Si junction up to 550 °C, while a

25 nm Ta-N can sustain up to 700 °C [57]. Therefore in industrial application, Ta/Ta-N bi-layer barrier is generally used, with Ta-N as the Cu barrier and Ta as the adhesive layer between dielectric and Ta-N. On the other hand, Ta-Si-N has also been studied as Cu diffusion barrier, and showed ability to retard Cu diffusion up to 850 °C. However, these works were conducted with different deposition method, film thickness, and characterization methods. Thus a direct comparison among the barriers is difficult. Therefore, it is important to do a systematic study on the barrier performance of Ta, Ta-N, and Ta-Si-N. It will also provide a good reference for the Ta-TM barriers to be studied in later part.

Three barriers were prepared as described in Chapter 3 as Ta, $Ta_{72}N_{28}$, and $Ta_{55}Si_{21}N_{23}$ from the composition identified by EDX. It should be noted that the oxygen was detected by EDX, but will be discussed in Chapter 7 instead of this chapter. The Cu/Ta/Si, Cu/$Ta_{72}N_{28}$/Si and Cu/$Ta_{55}Si_{21}N_{23}$/Si samples were annealed in vacuum and then analyzed using XRD and TEM to study the barrier failure at high temperature.

6.1.1. XRD and TEM study

Fig. 6-1 - Fig. 6-3 show XRD patterns of the Cu/Ta/Si, Cu/$Ta_{72}N_{28}$/Si and Cu/ $Ta_{55}Si_{21}N_{23}$ /Si stacks after annealing. The failures of the barriers are indicated by the growth of Cu_3Si. The as-deposited Cu/Ta/Si stack showed a sharp Cu (111) peak, a broadened α-Ta (110) amorphous peak, and a barely observable β-Ta (002) peak. The low β-Ta (002) peak is because of the weak signal compared to Cu peak, as Ta film deposited on Si has shown observable α-Ta (110) and β-Ta (002) peak [146]. After 500 ºC annealing, a low $TaSi_2$ peak appeared, showing the reaction between Ta and Si. After 600 °C annealing, a low Cu_3Si peak was observable, indicating the diffusion of

Cu through the Ta barrier and reaction between Cu and Si. At 700 °C, the Cu_3Si peaks were significant, showing a catastrophic failure of Ta barrier.

For the Cu/$Ta_{72}N_{28}$/Si sample, a weak Cu_3Si peak appeared at 700 °C, indicating Cu reaction with Si (Fig. 6-2). A low Ta_2O_5 peak grew at 700 °C also. At 750 °C, Both Cu_3Si and Ta_2O_5 peaks became more intense.

Cross-sectional TEM pictures for Cu/Ta/Si and Cu/$Ta_{72}N_{28}$/Si annealed at 700 °C show (Fig. 6-4) very different breakdown phenomena. For Cu/Ta/Si, the continuous Cu_3Si layer at Si/Ta interface and the void at Cu/Si interface were observable. For Cu/$Ta_{72}N_{28}$/Si, only nano-grained Cu_3Si at Si/Ta-N interface with grain size smaller than 5nm was observable.

On the other hand, failure of $Ta_{55}Si_{21}N_{23}$ occurred at 750 °C, as shown by the low Cu_3Si peak growth at 750 °C (Fig. 6-3). Significant growth of Cu_3Si occurred at 800 °C. No other peaks were observable when the failure occurred, showing the failure is caused by Cu diffusion through the barrier.

Different failure mechanisms were observed for these three barriers. For Ta, interfacial reaction between Ta and Si occurred before barrier breakdown. For $Ta_{72}N_{28}$, crystallization of Ta_2O_5 occurred together with barrier breakdown. Differently, no $TaSi_2$ or Ta_2O_5 peaks were observable for $Ta_{55}Si_{21}N_{23}$ even during strong Cu_3Si peak growth at 800 °C. It shows the different failure mechanism of the three barriers. For Ta barrier, the barrier breakdown is because of Cu diffusion through crystalline Ta barrier. For Ta-N barrier, the barrier breakdown is because of the crystallization of Ta-N at elevated temperature, which reduces the activation energy and increases Cu diffusivity.

For Ta-Si-N, it is because of Cu diffusion at a higher temperature through amorphous barrier.

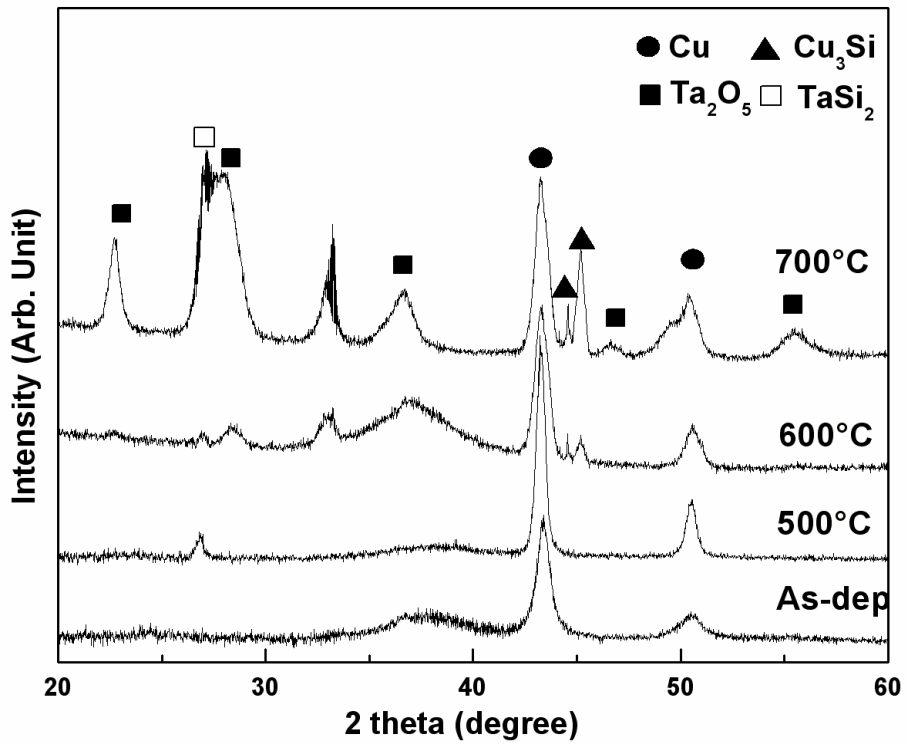

Fig. 6-1 XRD diffraction pattern of Cu/Ta/Si annealed in vacuum at 500 °C to 700 °C

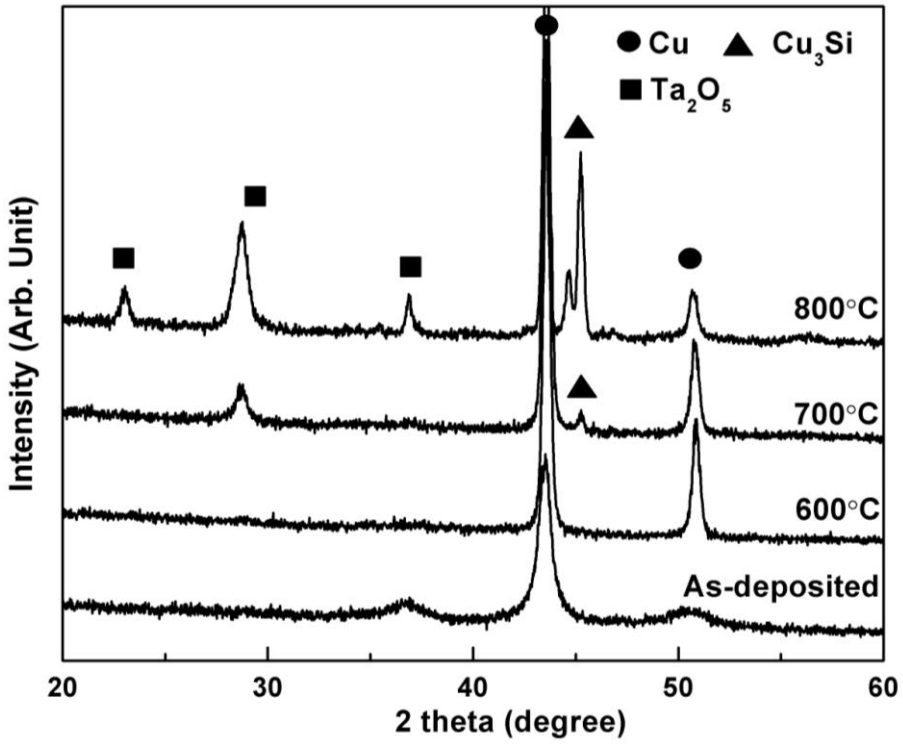

Fig. 6-2 XRD diffraction pattern of $Cu/Ta_{72}N_{28}/Si$ annealed in vacuum at 600 °C to 800 °C

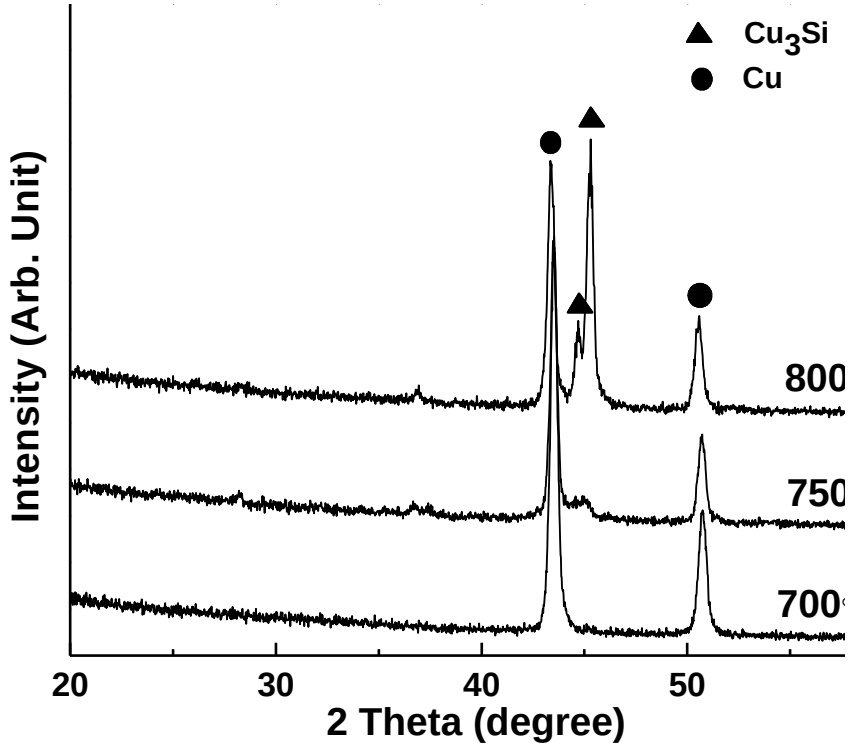

Fig. 6-3 XRD diffraction pattern of $Cu/Ta_{55}Si_{21}N_{23}/Si$ annealed in vacuum at 700 °C to 800 °C

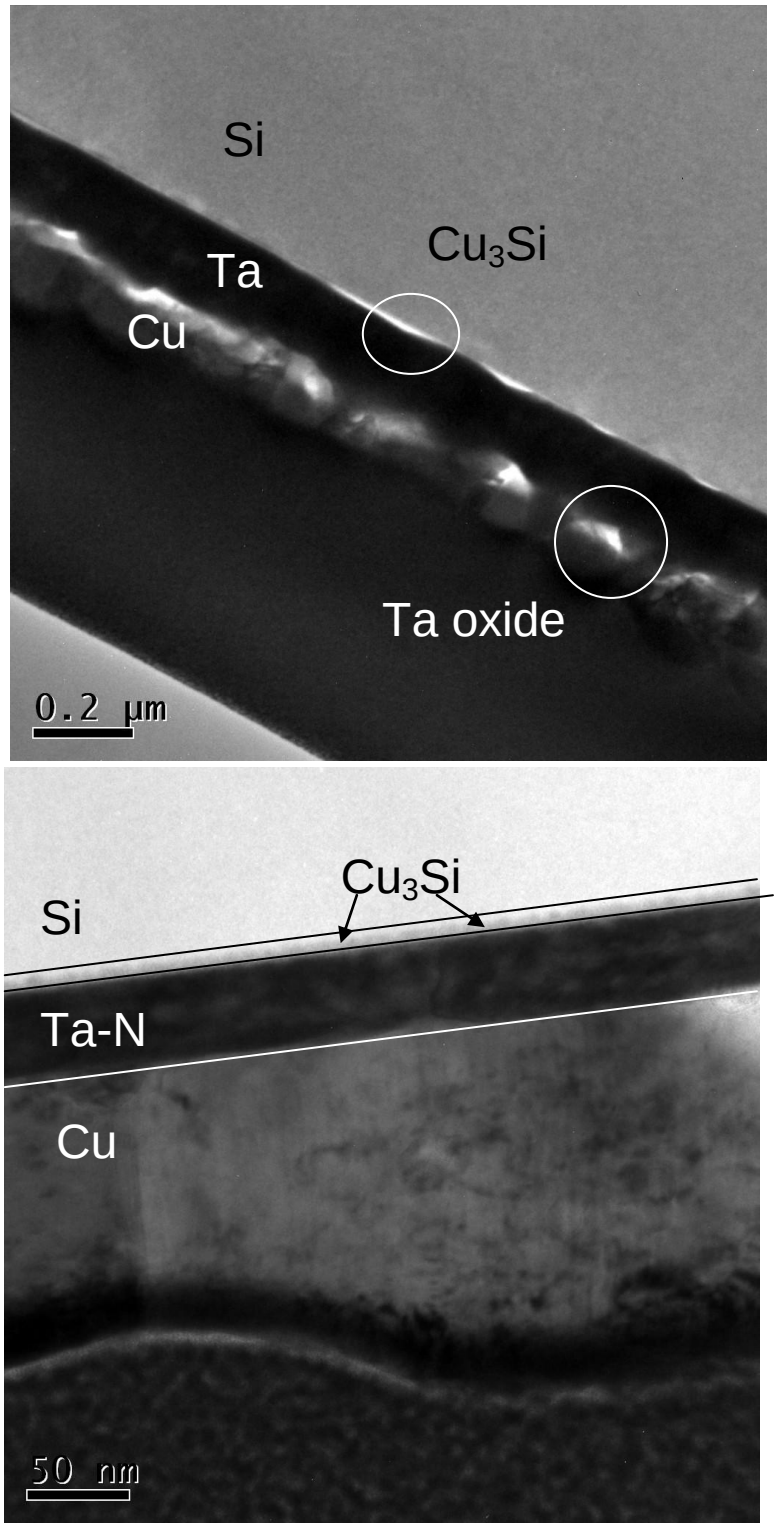

Fig. 6-4 TEM image of (a) Cu/Ta/Si and (b) Cu/$Ta_{72}N_{28}$/Si annealed in vacuum upon failure

6.1.2. Discussion

The barrier performance of Ta, Ta-N and Ta-Si-N are summarized in Table 6-1. The failures of the barriers are indicated by the observation of Cu_3Si. The failure of Ta, Ta-N and Ta-Si-N barrier occurs at 600 °C, 700 °C and 750 °C, respectively. It clearly shows that the barrier performance is getting better with more complex system.

Upon failure, $TaSi_2$, which was not found for Ta-N and Ta-Si-N, was observed for Cu/Ta/Si barrier before Cu_3Si was detectable. On the other hand, Ta_2O_5 peaks were observed for Ta and Ta-N barrier, while there was no crystalline peak for Ta-Si-N. It shows that Cu diffusion through crystalline barrier (Ta) is the fastest among the three barriers. For Ta-N barrier, Cu diffusion happens when barrier crystallizes at 700 °C. For Ta-Si-N barrier, the barrier breakdown is a result of Cu diffusion through the amorphous films. The highly stable amorphous Ta-Si-N thus shows best barrier performance compared to other two.

Table 6-1 Growth temperature of various compounds during failure of Ta, Ta-N and Ta-Si-N Cu diffusion barrier

	Ta	Ta-N	Ta-Si-N
Failure temperature (Observation of Cu_3Si peaks)	600 °C	700 °C	750 °C
Observation of Ta_2O_5 peaks	500 °C	700 °C	--
Observation of $TaSi_x$ peaks	600 °C	--	--

6.2. Diffusion barrier performance of Ta-Ni, Ta-Cr and Ta-Ti on Si substrate

6.2.1. Cu/Ta-Ni/Si

Ta-Ni barrier with composition of $Ta_{70}Ni_{30}$ were deposited as described in Chapter 3. Fig. 6-5 shows the XRD plot of the Cu/ $Ta_{70}Ni_{30}$/Si samples annealed in vacuum at 600 °C to 800 °C. For as-deposited samples, no crystalline peaks was present in the Ta-Ni film. Only Cu (111) and Cu (200) peaks were present. The top-view SEM picture (Fig. 6-6(a)) shows that the sputtered Cu grains size of 50 - 100 nm. As reported by Yang et al., Cu (111) and Cu (200) peaks are present for Cu deposited on Ta-N substrate, while Cu (111) is preferred for Cu deposited on Ta substrate [147]. The lack of Cu (200) structure on Ta substrate was attributed to the strong interaction between Ta and Cu which promotes Cu (111) orientation. The existance of Cu (200) peak in the current system suggests that Cu/Ta-Ni interfacial interaction is similar to Ta-N, rather than Ta.

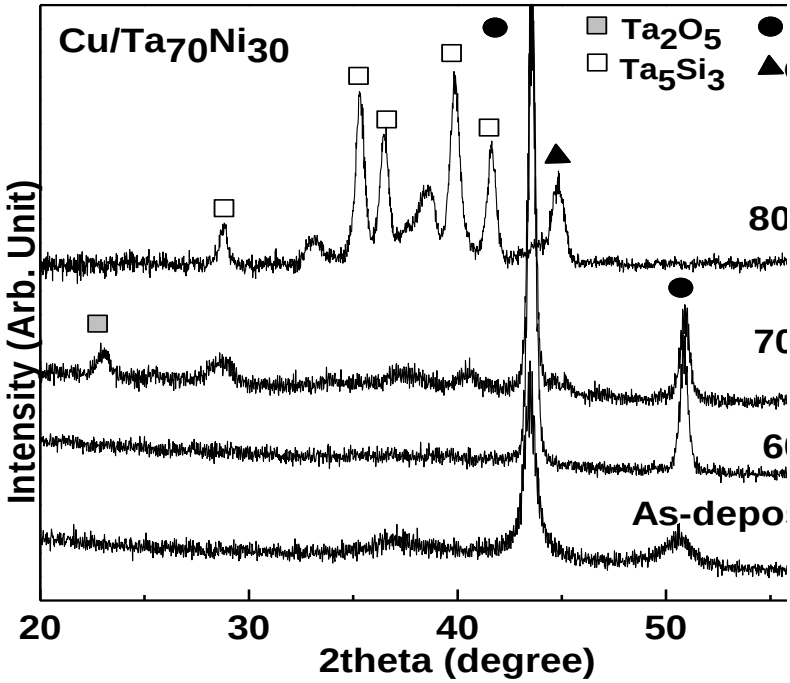

Fig. 6-5 XRD diffraction pattern of $Cu/Ta_{70}Ni_{30}/Si$ film annealed in vacuum at 600 °C to 800 °C

After the film stack was annealed at 600 °C for 30 min, no chemical reaction(s) occurred except the growth of Cu crystals. The top-view SEM picture (Fig. 6-6(b)) shows Cu grain growth and surface roughness reduction, which agrees with the XRD observation. The cross sectional TEM pictures (Fig. 6-7(a) and (b)) show there is no crystallization or interfacial reaction. Therefore, the Ta-Ni barrier remains stable at 600 °C. Compared to the Ta barrier which breaks down at 600 ºC by formation of Cu_3Si, Ta-Ni film shows better barrier performance.

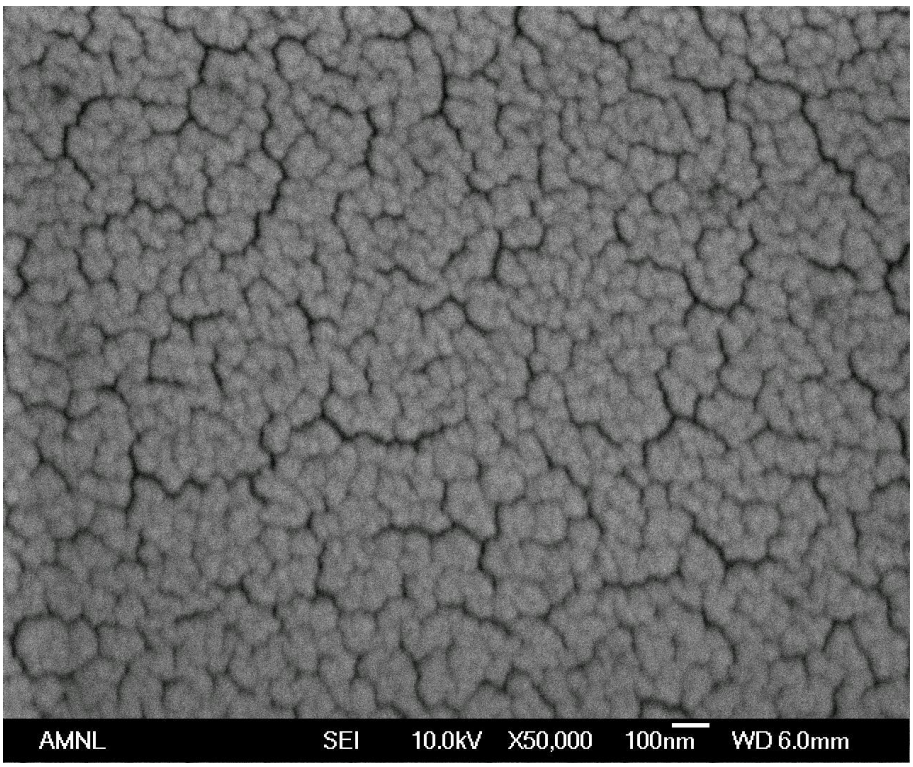
AMNL SEI 10.0kV X50,000 100nm WD 6.0mm

(a)

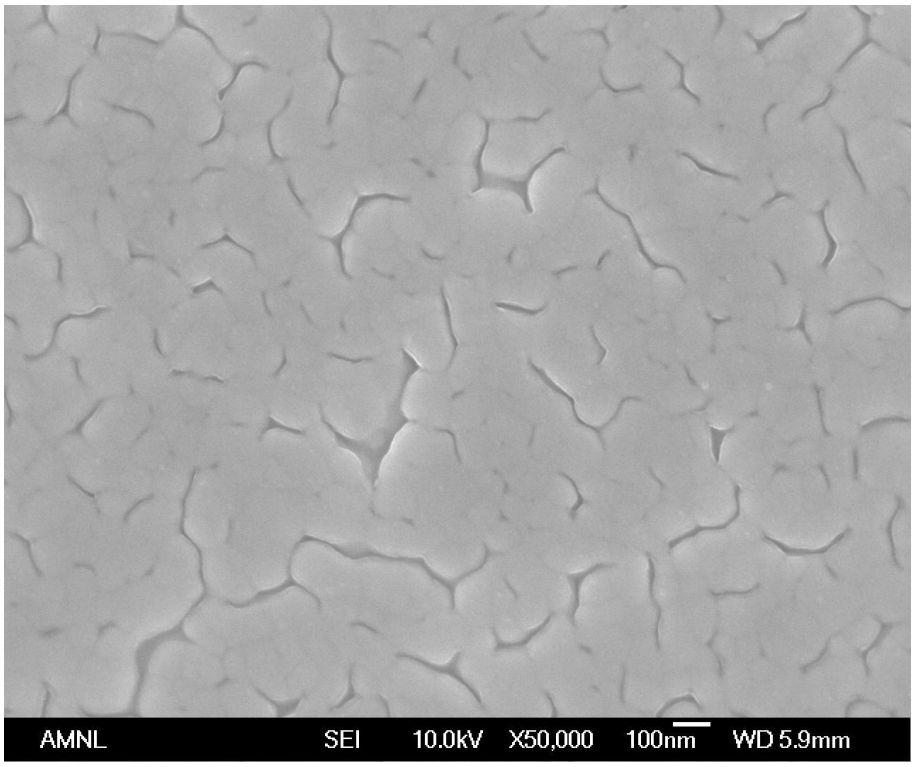
AMNL SEI 10.0kV X50,000 100nm WD 5.9mm

(b)

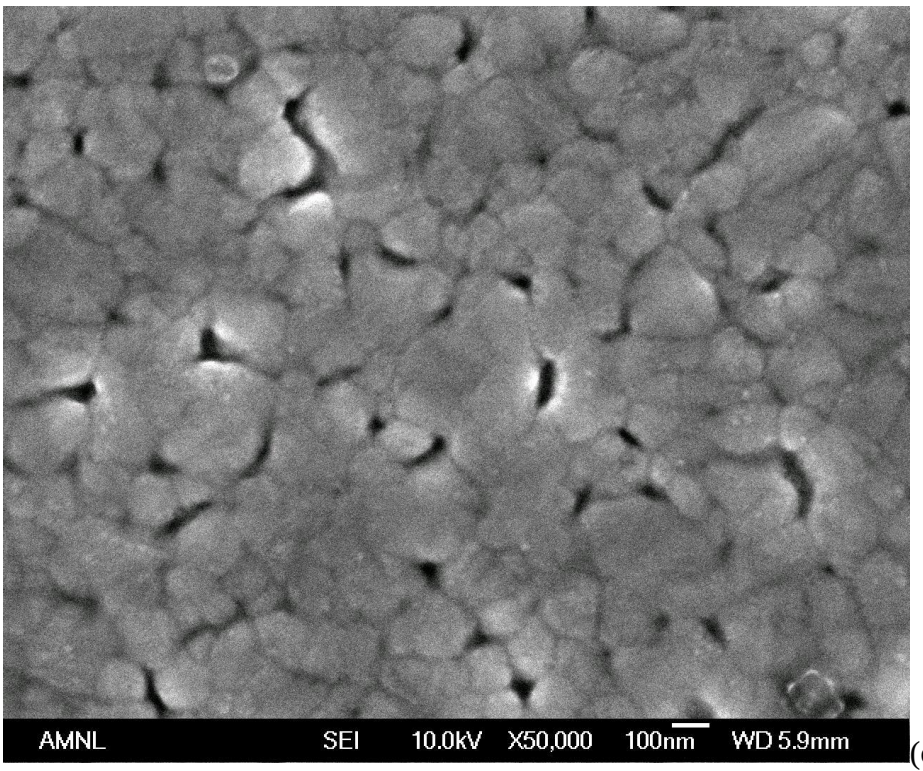

(c)

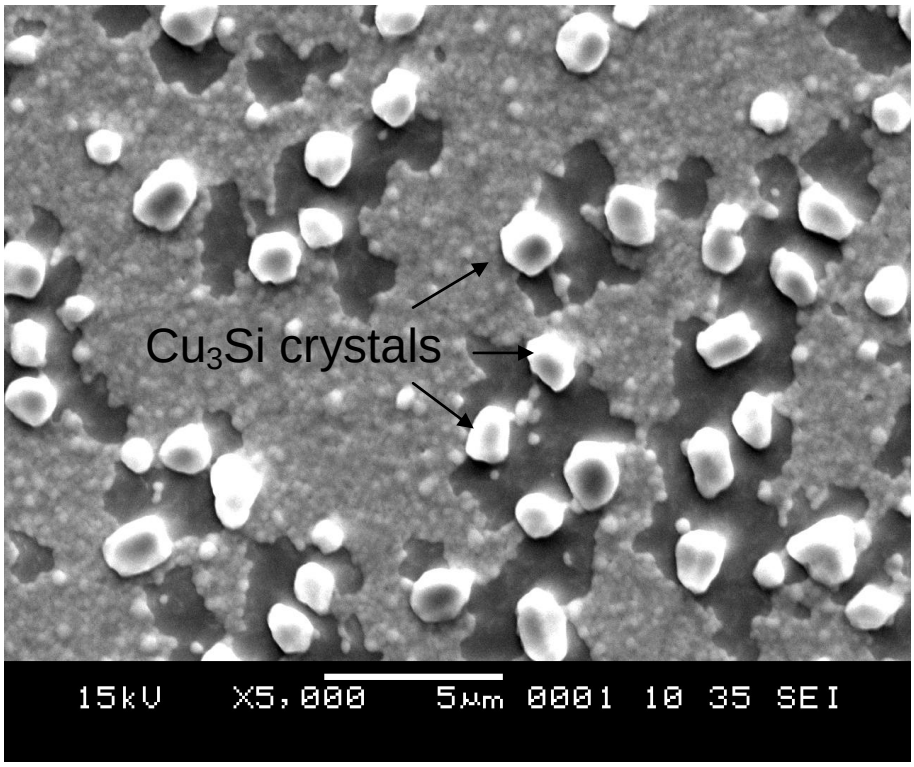

(d)

Fig. 6-6 Top-view FESEM picture of Cu/$Ta_{70}Ni_{30}$/Si (a) at as-deposited state; (b) annealed at 600 °C; (c) annealed at 700 °C; (d) annealed at 800 °C

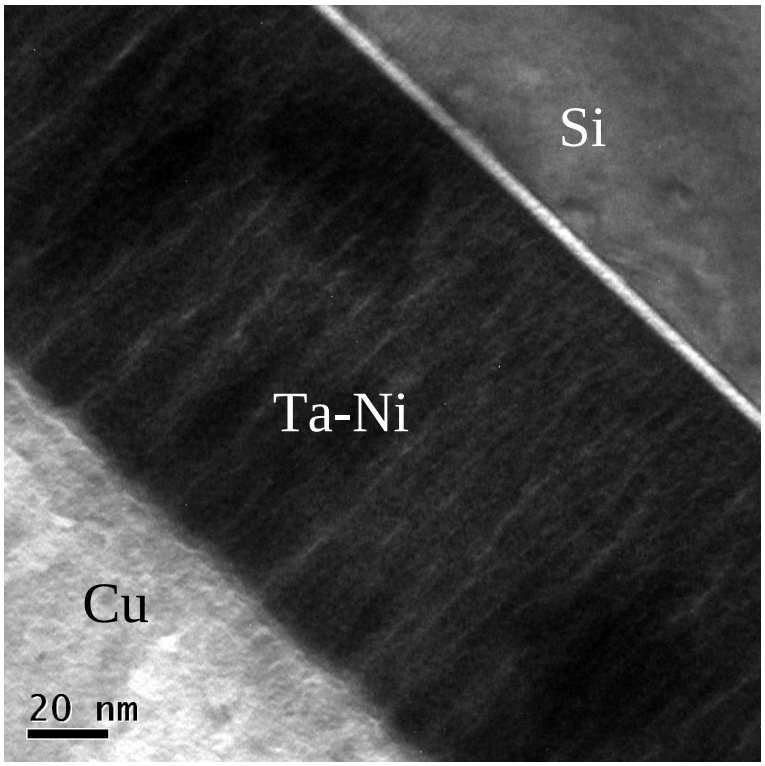

(a)

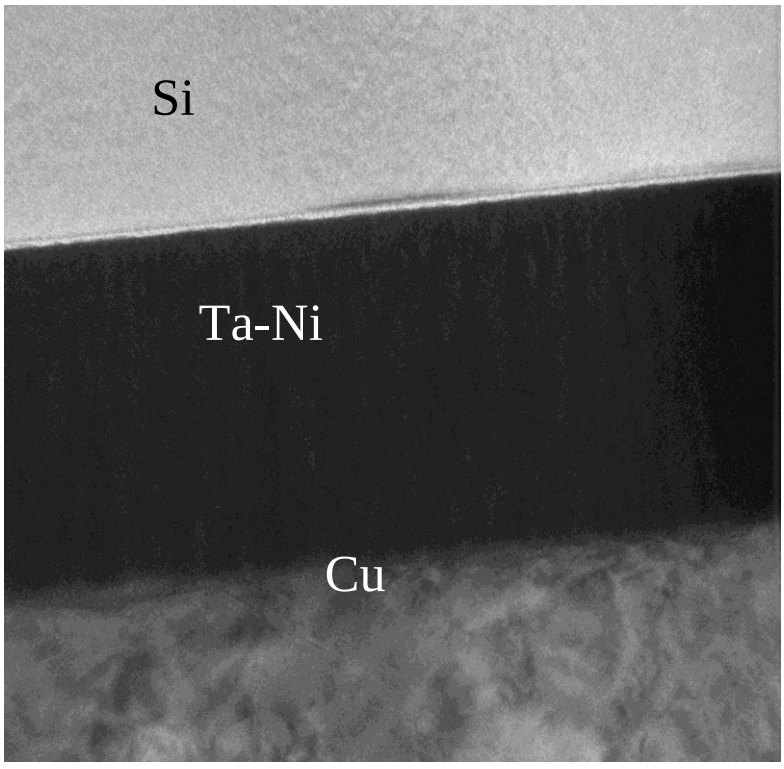

(b)

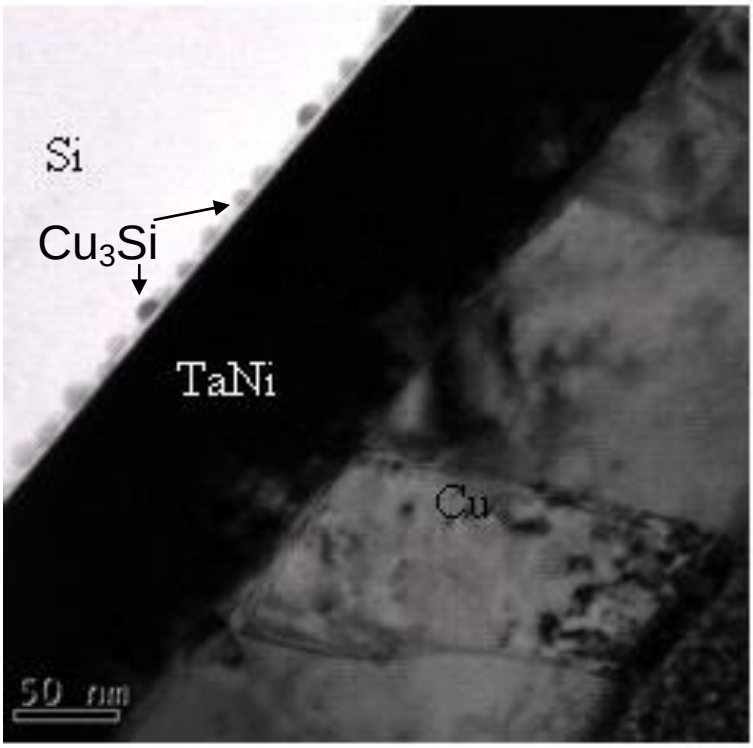

(c)

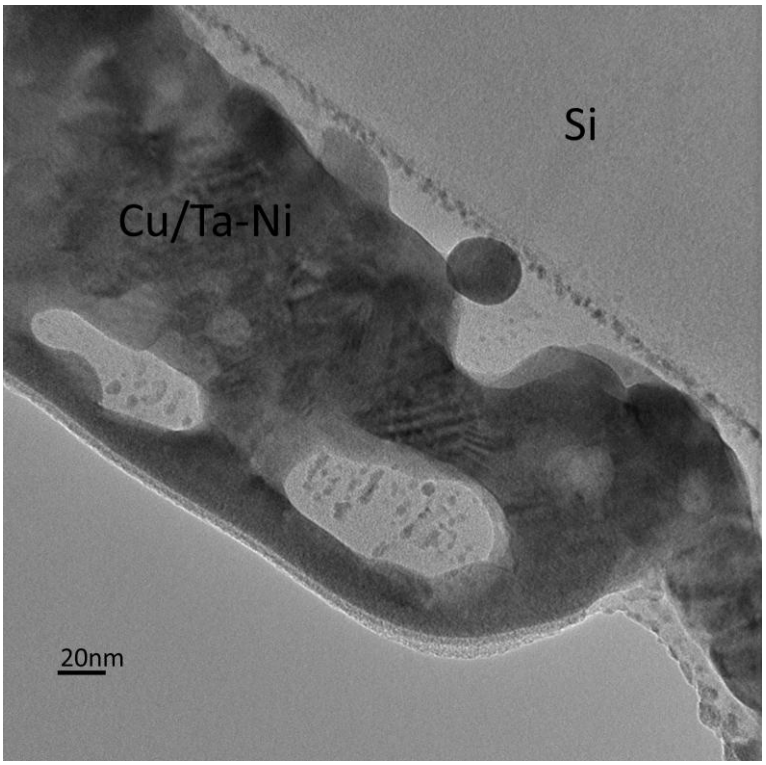

(d)

Fig. 6-7 Cross-sectional TEM image of Cu/$Ta_{70}Ni_{30}$/Si (a) at as-deposited state; (b) annealed at 600 °C; (c) annealed at 700 °C; (d) annealed at 800 °C

At 700 °C, multiple crystalline peaks were observed in Fig. 6-5. The crystalline peaks at 22.9° and 28.4° indicate the growth of Ta_2O_5 crystals. TEM picture (Fig. 6-7(c)) also shows a thin layer of Ta_2O_5 at the interface of $Ta_{70}Ni_{30}$ and Cu. It is noted that the oxide formation is at a lower temperature compared to Ta-Ni/Si without Cu layer. The latter only shows Ta_2O_5 at 800 °C, as studied in Chapter 5. The formation of Ta_2O_5 at Ta/Cu interface was reported in the study of Ta barrier [148]. Li reported various Ta_2O_5 formations for barrier/Si and Cu/barrier/Si stack were attributed to the tensile stress resulted from the CTE mismatch between copper and barrier [149]. The effect of Ta_2O_5 thin layer on the barrier properties is not systematically investigated in this work. It was reported that the amorphous Ta_2O_5 formed by ALD failed as Cu diffusion barrier at 700 °C. Thus it is expected that if a continuous Ta_2O_5 line can be formed at the interface, the Ta_2O_5 could behave as extra barrier to prevent Cu diffusion. SEM picture (Fig. 6-7(c)) shows a continuous surface of Cu, thus no severe reaction occurred at 700 °C. However TEM image in Fig. 6-7(c)) shows a small amount of nano Cu_3Si grain growth at the $Ta_{70}Ni_{30}$/Si interface. As shown in Fig. 6-5, small peaks at 44°-45° were observed in the XRD plot, indicating Cu_3Si formation. The formation of Cu_3Si is a sign of Cu in-diffusion through the Ta-Ni barrier. The finding is largely in agreement with what have been reported by Fang that $Ta_{50}Ni_{50}$ can prevent Cu diffusion into Si at temperature up to 700 °C [150].

After 800 ºC annealing, XRD, TEM and SEM all showed severe reaction among Cu, $Ta_{70}Ni_{30}$, and Si. Multiple crystalline peaks of Ta_5Si_3 appeared in the XRD scan, including a high Cu_3Si peak at 44º (Fig. 6-5). As reported by Yuan et al., Ta_2O_5 reacts with Si at 750 ºC – 850 ºC to form Ta_5Si_3 and SiO_2 [151]. This explains the decline of Ta_2O_5 peaks and growth of Ta_5Si_3 peaks. The top view SEM in Fig. 6-6(d) indicates the loss of Cu integrity and growth of Cu_3Si crystal with size of sub-micron size on the

surface. As observed in TEM (Fig. 6-7(d)), the barrier has been detached from the Si substrate, and mixed with Cu and Ta-Ni. Further EDX studies showed high Si and Cu signal in the originally barrier layer. This shows that Ta-Ni barrier has failed catastrophically at 800 ºC.

In conclusion, SEM, TEM and XRD studies showed the failure of $Ta_{70}Ni_{30}$ barrier at the temperature between 700-800 ºC. At 700 ºC, weak Cu_3Si crystalline peaks were observed together with the observation of Ta_2O_5 at $Ta_{70}Ni_{30}$/Cu interface. Subsequently at 800ºC, catastrophic failure was observed. The films lost the integrity, with the formation of $TaSi_x$ and Cu_3Si.

The study shows that the barrier performance of Ta-Ni is better than Ta. At 700 °C, severe amount of Cu_3Si grows at Ta/Si interface for Ta barrier, while only small amount of Cu_3Si grows at Ta-Ni/Si interface for Ta-Ni barrier. It is apparent that the existence of Ni improved the barrier stability and performance. In Ta barrier, the failure of barrier is initiated by the formation of $TaSi_2$, which causes the fast diffusion of Cu into the Si substrate. In Ta-Ni barrier, the existence of Ni inhibits the reaction between Ta and Si, and slows down the diffusion of Cu through barrier.

6.2.2. Cu/Ta-Cr/Si

$Ta_{67}Cr_{33}$ was deposited as Cu diffusion barrier in this part. As shown in section 3.2, the amorphous Ta-Cr film showed similar thermal stability as Ta-Ni films. The crystallization of Ta-Cr occurs at 800ºC, with the formation of multiple Ta-based and Cr-based compounds.

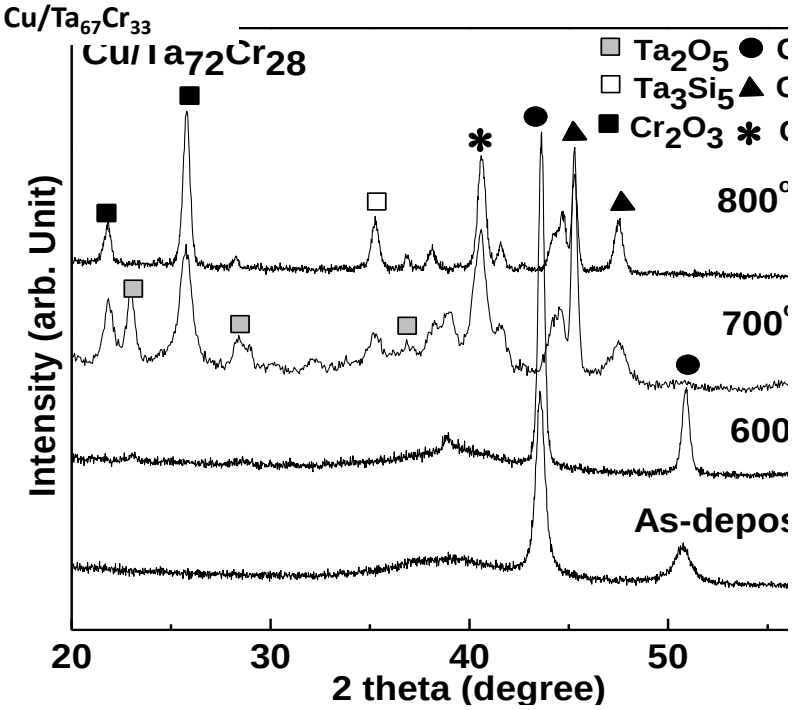

Fig. 6-8 XRD diffraction pattern of Cu/ $Ta_{67}Cr_{33}$/Si film annealed in vacuum at 600 °C – 800 °C

Fig. 6-8 shows the XRD evolution of Cu/$Ta_{67}Cr_{33}$/Si annealed at 600ºC to 800ºC. As-deposited $Ta_{67}Cr_{33}$ was amorphous, similar Ta-Ni. At 600 ºC, the amorphous phase was largely maintained. At 700ºC, multiple crystalline phases appeared, including Ta_2O_5, $TaSi_2$, $CrSi_2$, Cr_2O_3 and Cu_3Si. It was observed that the Cu peaks disappeared at 800ºC, showing complete reaction between Cu and Si. Different from the Ta-Ni barrier, where Cu_3Si peaks were barely observable at 700ºC, high-intensity Cu_3Si peaks were observed for $Ta_{67}Cr_{33}$ barrier at 700ºC, showing more severe reaction than Ta-Ni. All Cu has been consumed at 700ºC, as the Cu (111) peaks completely disappeared after the annealing. The failure of Ta-Cr apparently occurs earlier than Ta-Ni barrier, which can be attributed to the formation of Cr_2O_3 and $CrSi_2$. As the formation of Cr related structure accelerated the interface reaction, fast diffusion of Cu through $Ta_{67}Cr_{33}$

barrier occurred. It is also noted that the interface between $Ta_{67}Cr_{33}$ and Cu has lost integrity at 700 ºC. EDX showed large amount of O in this region. Intensive reaction between Cr and Si/O also accelerated the failure of the $Ta_{67}Cr_{33}$ barrier and promoted the reaction between Cu and Si.

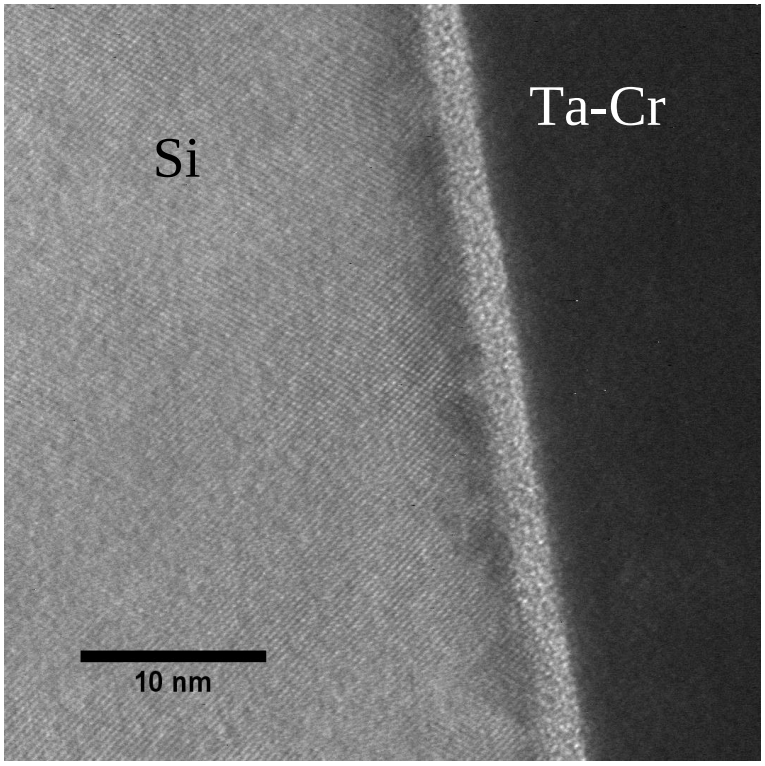

(a)

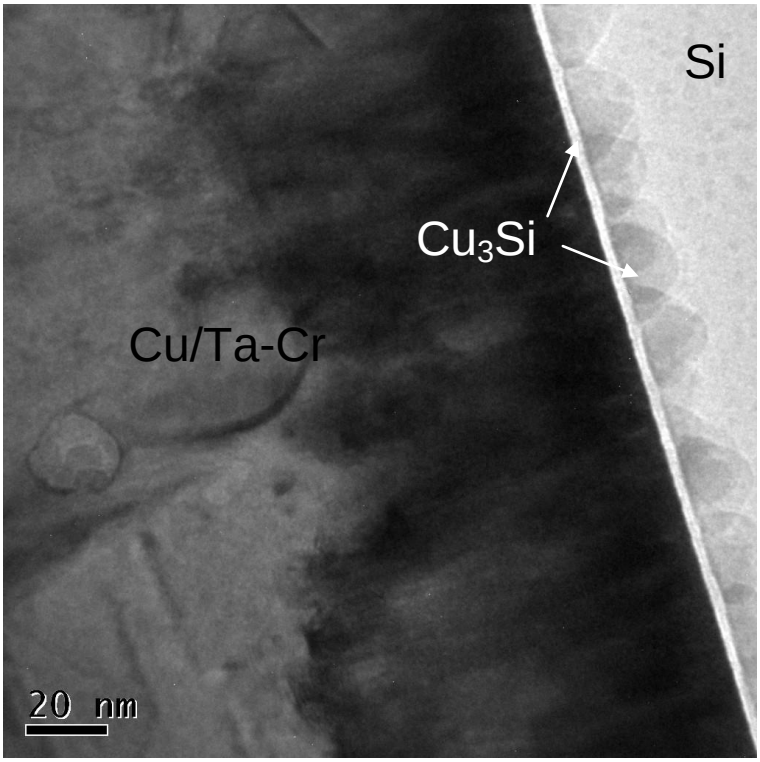

(b)

Fig. 6-9 Cross-sectional TEM image of $Cu/Ta_{67}Cr_{33}/Si$ thin film annealed in vacuum at (a) 600 °C and (b) 700 °C

6.2.3. Cu/Ta-Ti/Si

A $Ta_{78}Ti_{22}$ barrier was studied in this part. As studied in section 3.3, at as-deposited state, the films show combination of Ta and Ti phases. At 600 ºC, β-Ta transformed to α-Ta with an intermediate amorphous state formed. The Cu and Ta/Ti phases were observed in in $Cu/Ta_{78}Ti_{22}/Si$ film before annealing. Upon 600 °C annealing, the Ti peaks was not observable. It shows the amorphization has taken place (Fig. 6-10). At 700 °C, Ta_2O_5 and Ta_5Si_3 peaks was found. Cu_3Si, which indicates the barrier breakdown, was also observed. For Ta-Cr and Ta-Ni barrier, there is no Ta silicide formation when Cu_3Si are formed at 700 °C. The observation of Ta_5Si_3 in $Ta_{78}Ti_{22}$ apparently suggests a less stable Ta-Ti/Si interface. At 800 °C, high $TaSi_2$ peaks growth were observed, which shows that the barrier integrity has lost.

As observable from the TEM picture in Fig. 6-11, tiny grains grew at interface between barrier and Si substrate at 600 °C. However, EDX shows only Si at the location. It is related to local strain caused by the Cu in-diffusion. Cu_3Si grains with size of 10-20 nm were presented between the interface of substrate and barrier at 700 °C, which is confirmed by EDX scan. EDX measurement showed mixture of Cu, Ta and Ti in the barrier films. It shows the failure of barrier is caused by Cu in-diffusion through the barrier.

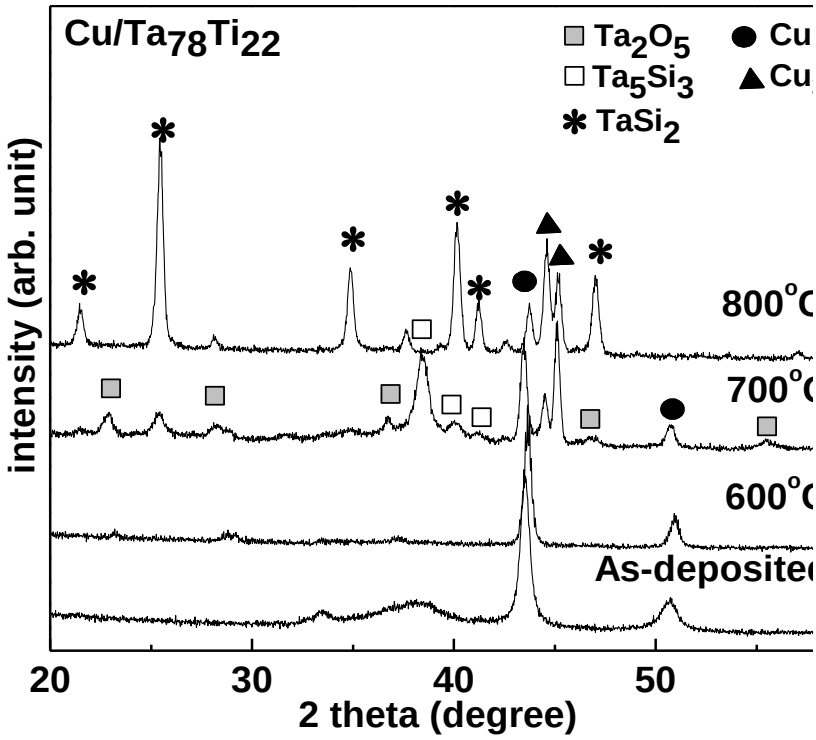

Fig. 6-10 XRD diffraction pattern of $Cu/Ta_{78}Ti_{22}/Si$ thin film annealed in vacuum at 600 °C to 800 °C

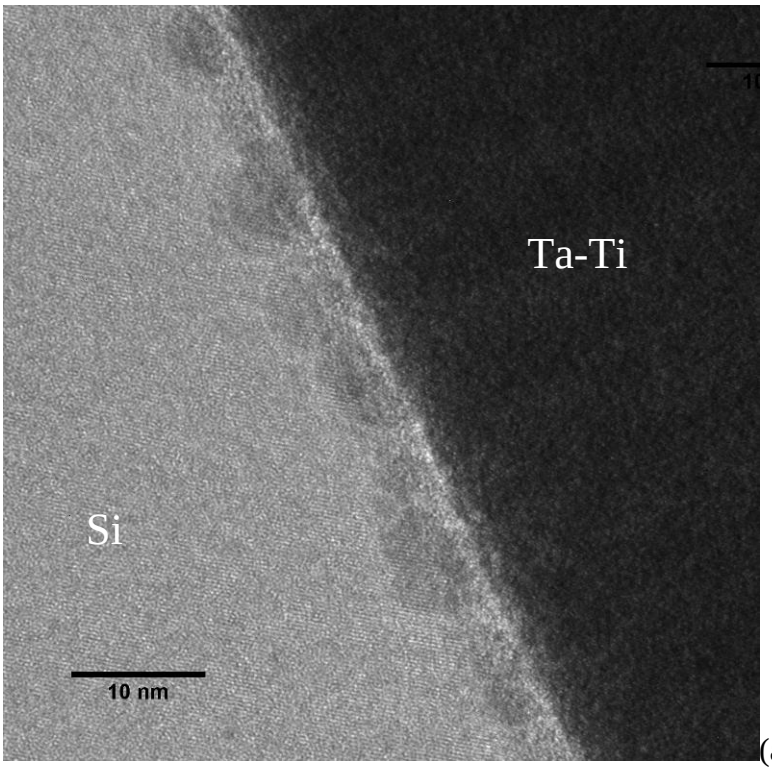

(a)

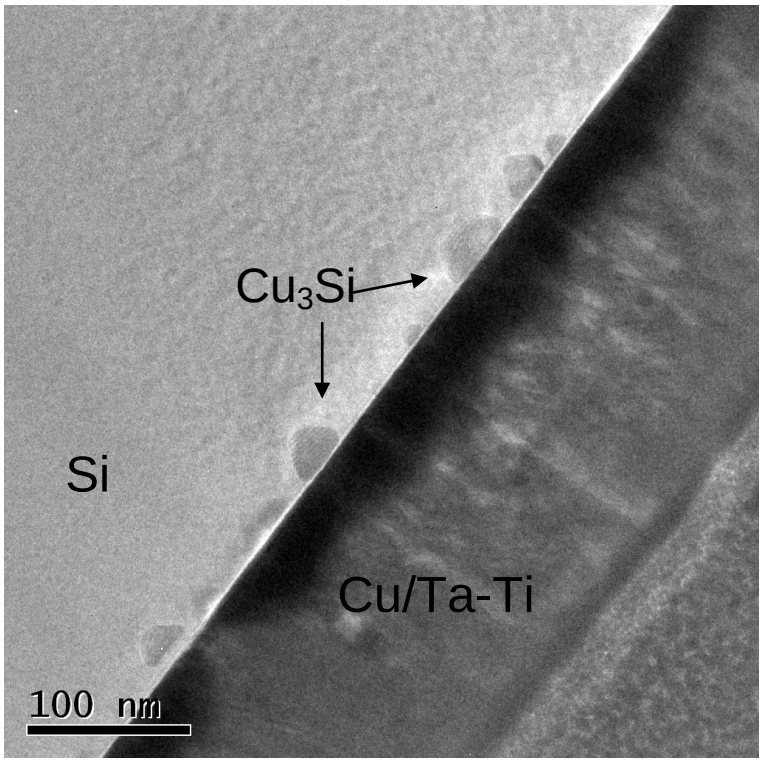

(b)

Fig. 6-11 Cross-sectional TEM image of Cu/ $Ta_{78}Ti_{22}$/Si thin film after annealed at (a) 600 °C and (b) 700 °C

6.2.4. Discussion

As shown in section 6.1, the barrier performance of the binary Ta-TM is better than Ta and comparable with Ta-N. Among the studied Ta-TM barriers, the performance seems to follow the same order of their GFA, viz.

Ta-Ni > Ta-Cr > Ta-Ti > Ta

Diffusion of Cu through Ta-Ni barrier was observed at 700 °C as studied by TEM, XRD, and SIMS. Small amount of nano-crystalline Cu_3Si was detected as the indication of barrier failure. For Ta-Cr barrier, besides the formation of Cu_3Si, $CrSi_2$ crystalline phase was also observed in XRD at 700 °C. More intensive Cu_3Si peaks indicate more severe Cu diffusion in Ta-Cr than in Ta-Ni. Ta-Ti barrier also failed after 700 °C annealing with intensive Cu_3Si peaks in XRD. It is noted that for all three groups of barriers, Ta_2O_5 forms at 700 °C.

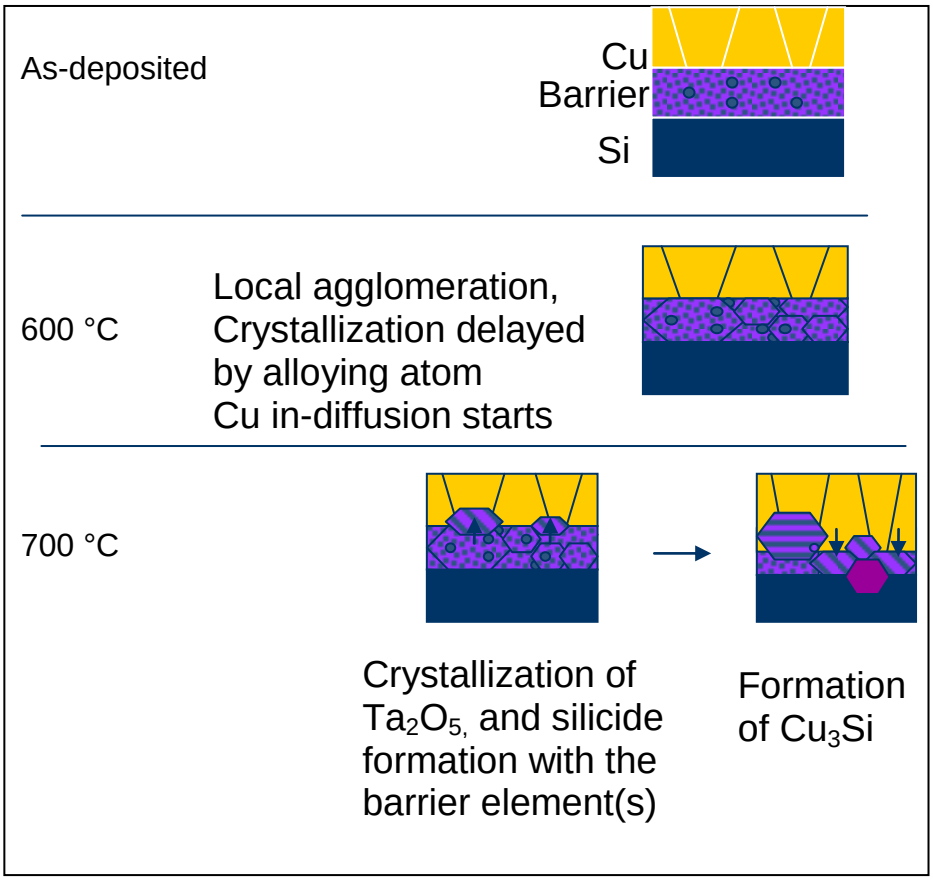

Fig. 6-12 Mechanism of Ta-TM barrier breakdown as Cu diffusion barrier on Si substrate

Fig. 6-12 shows the failure mechanism of the Ta-TM barriers. It suggests that the higher stability of Ta-TM barrier is attributed to the alloy effect of Ni, Cr and Ti atoms. The crystallization of the amorphous barrier is delayed due to the alloy elements. The crystallization of barrier is caused by the oxidation of Ta, followed by the in-diffusion of Cu through the grain boundaries. Comparing the different alloying element, it is obvious that the performance of the Ta-TM barrier is affected by the stability of the Ta-TM alloy. More stable Ta-TM alloy shows better barrier performance.

6.3. Depth profile of diffused Cu in Ta-Ni barrier

Fig. 6-13 shows the depth profile Cu/Ta-Ni/Si at different temperatures measured by ToF-SIMS. For the as-deposited state, a relatively sharp interface for each layer is distinguishable. As discussed in Chapter 3, O is observed in Ta-Ni layer and Cu layer, due to the O residue in the sputtering chamber. While it is inevitable that O will be incorporated into the film during sputtering process, such incorporation of O actually enhances the thermal stability of the Ta-Ni layer. The effect of O on barrier performance of Ta-Ni films will be separately studied in Chapter 7At 500 °C and 600 °C, change of Cu gradient showed the in-diffusion of Cu to Ta-Ni. Comparing the two SIMS profiles, it is clear that certain amount of Cu has diffused into Ta-Ni at the elevated temperatures. The Si profile remained almost the same up to 700 °C, showing no significant diffusion.

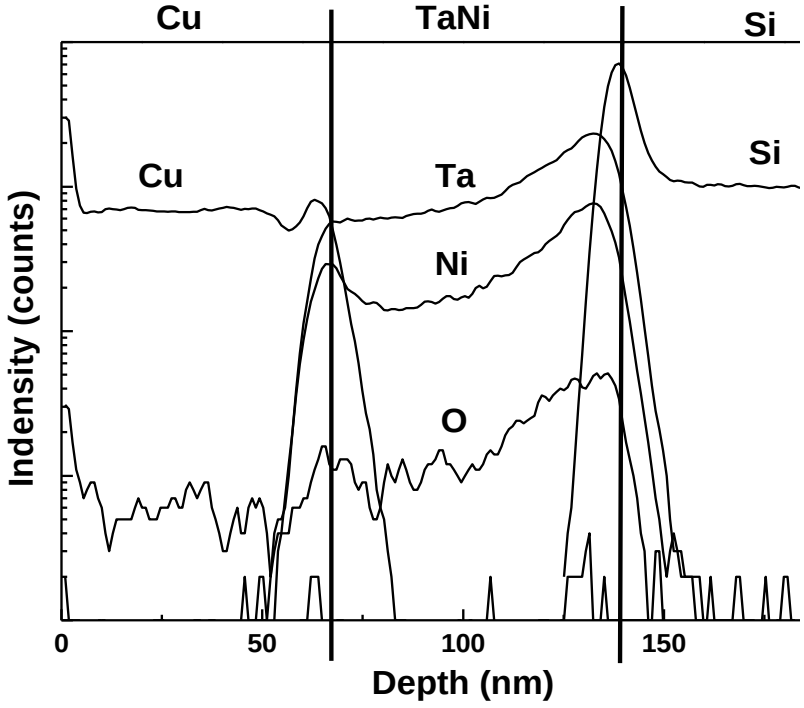

(a)

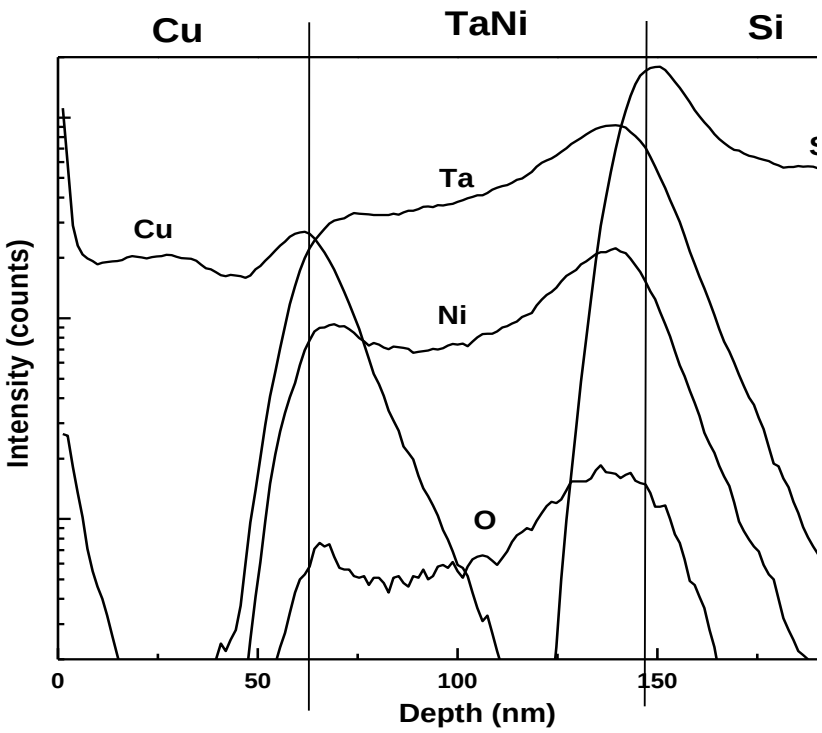
Cu
TaNi
Si
Ta
Cu
Ni
O
Intensity (counts)
0
50
100
150
Depth (nm)

(b)

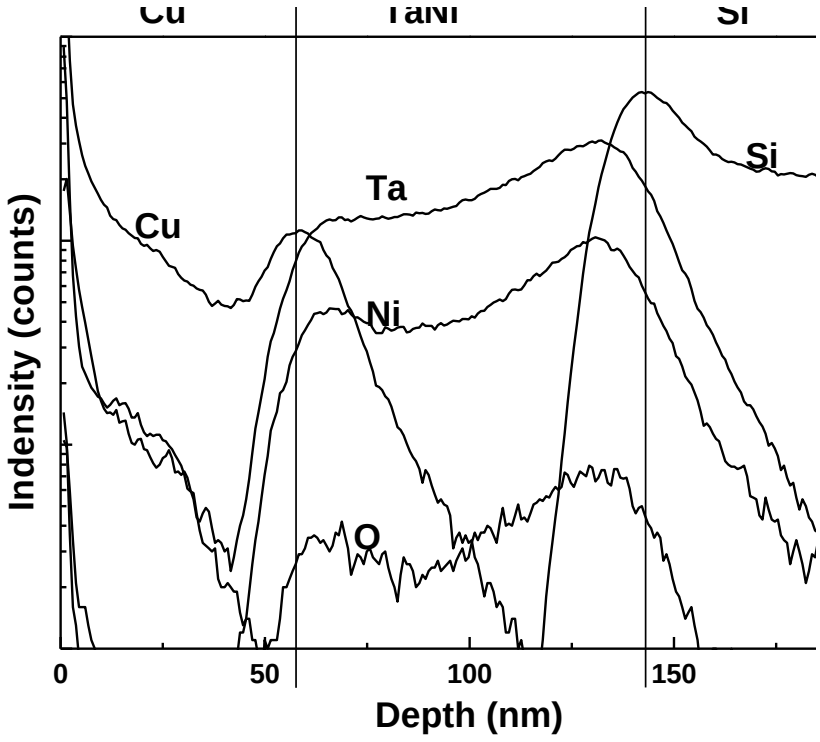
Cu
TaNi
Si
Ta
Cu
Ni
O
Indensity (counts)
0
50
100
150
Depth (nm)

(c)

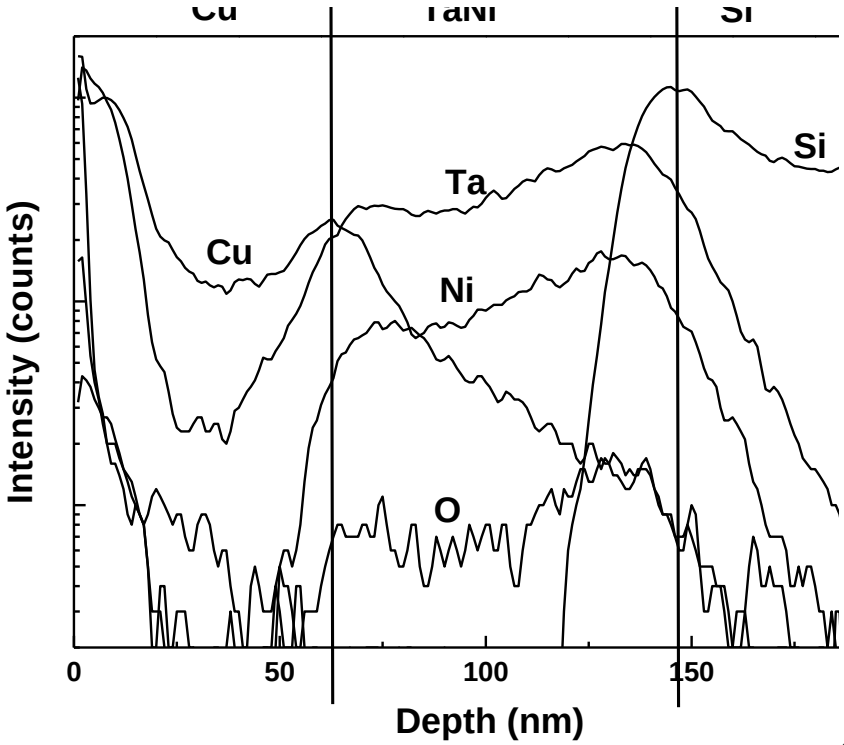

(d)

Fig. 6-13 ToF-SIMS depth profile of elements Cu, Ta, Ni O, Si of Cu/Ta-Ni/Si (a) at as-deposited state (b) annealed at 500 °C; (c) annealed at 600 °C; (d) annealed at 700 °C.

As the diffusivity is calculated as:

$$D = D_0 exp\left(-Ea/kT\right) \tag{6.1}$$

Based on the diffusion profiles, the diffusivity of Cu in Ta-Ni can be estimated using equation (6-2) at temperature of 500 °C, 600 °C and 700 °C

$$l = \sqrt{4Dt} \tag{6.2}$$

where l is the diffusion distance, D is diffusivity, and t is diffusion time. The diffusivity constant is summarized in Table 6-2. Because of the failure of Ta-Ni barrier at 700 °C, Ea and D_0 cannot be calculated using the diffusivity at 700 °C. A more

Table 6-2 Diffusion rate of Cu in Ta-Ni thin film at different temperature

Temperature (°C)	Diffusivity (cm^2/s)
500	2.00E-15
600	2.43E-15
700	2.94E-14

precise measurement of diffusivity at lower temperature needs to be carried out to understand the Cu diffusion in Ta-Ni barrier at lower temperature.

6.4. Discussion

6.4.1. Barrier performance comparison

Comparisons of the studied films are provided in Table 6-3 for the studied barriers. Based on the breakdown temperature, the performance is ranked in the sequence of:

Ta-Si-N > Ta-N and Ta-Ni > Ta-Cr > Ta-Ti > Ta

However, in terms of electrical resistivity, they are ranked as:

Ta < Ta-Ni, Ta-Ti, Ta-Cr < Ta-N<Ta-Si-N

Compared to the other barriers, Ta-Si-N shows the best barrier performance, but with highest electrical resistivity. On the other hand, Ta has the lowest electrical resistivity, but the barrier performance is the worst. Therefore they are not good candidate as Cu diffusion barriers. Comparing Ta-N and Ta-TM, Ta-TM generally showed lower electrical resistance, which important especially for advanced technology when RC delay is getting more critical. The small resistivity variation with composition change also allows a larger process window. For the barrier performance, Ta-Ni shows

comparable barrier performance with Ta-N, while Ta-Ti and Ta-Cr shows worse performance. It is noted that the failure of Ta-Cr and Ta-Ti barrier was at same temperature of Ta-N and Ta-Ni, but with more severe integrity loss. Ta-Cr fails because of the reaction between Cr and Si which accelerates the failure of the barrier, while Ta-Ti fails because of the poor glass formation between the two elements. It shows binary amorphous barrier still can be further explored to study more alloy combination, with the consideration of good amorphous formation ability and high stability with Si substrate.

Based on the comparison, Ta-Ni is apparently the best candidate as Cu diffusion barrier among all the studied candidates, even compared to the industrial proven Ta-N. More exploration is needed to extend the study to more purposely formed binary amorphous alloy.

Table 6-3 Comparison of Ta, Ta-N, Ta-Si-N, Ta-Ni, Ta-Cr and Ta-Ti thin film properties and their barrier performance

	Ta	Ta-N	Ta-Si-N	Ta-Ni	Ta-Cr	Ta-Ti
As-deposited resistivity (umcm)	2.67	627-679	771-122700	165-448	223-317	408-505
As-deposited phase	α-Ta, β-Ta	Amorphous	Amorphous	Amorphous	Amorphous	α-Ta, β-Ta/Ti crystalline
Crystallization temperature	--	800 °C	900 °C	800 °C	800 °C	Solid-phase amorphourization occurs at 600 °C. Crystallization occurs at 800 °C
Cu_3Si formation temperature	600 °C	700 °C	750 °C	700 °C	700 °C	700 °C
Phase formed upon failure	$TaSi_2$ Ta_2O_5	Ta_2O_5	No other phase	$TaSi_2$ Ta_2O_5	$TaSi_2$ Cr_2Si_3	$TaSi_2$
Lost of integrity upon failure?	No	No	No	No	Yes	Yes

6.4.2. Guidelines for forming good thin film barriers

As summarized from this study, a few guidelines are summarized to form effective thin film barriers.

a) Film with stable amorphous structure provides better barrier performance than crystalline counterpart. The barrier performance improves with more thermal stable amorphous system.

Among all the studied barriers, Ta-Si-N shows most stable amorphous structure, which crystallizes at 900 °C, compared to 800 °C for Ta-N, Ta-Cr, Ta-Ni and Ta-Ti. It also shows best barrier performance in terms of the Cu_3Si formation temperature. In this case, the high thermal stability of Ta-Si-N makes it the best Cu diffusion barrier among all candidates.

Comparing Ta barrier with Ta-N and Ta-TM, the crystalline Ta barrier fails at lower temperature compared to amorphous Ta-N and Ta-TM barriers.

Therefore, it can be concluded that the performance of Cu diffusion barrier is largely affected by the microstructure of barrier film. The amorphous film could behave as a better barrier compared to crystalline film. For as-deposited amorphous barriers, the Cu diffusion is triggered by the crystallization of barriers for Ta-N and Ta-TM. While for Ta-Si-N, the barrier failure is triggered by Cu diffusion through the amorphous barrier, which is at higher temperature (750 °C) compared to Ta which is crystalline (600 °C) or Ta-N and Ta-TM which crystallizes when annealed (700 °C). Thus Ta-Si-N with stable amorphous phase is able to retard Cu diffusion at higher temperature compared to other barriers.

It was also noticed that, barrier/Si reaction was observed for Ta-TM and Ta barrier, but not for Ta-N and Ta-Si-N. It could be due to the chemical stability of Ta-N and Ta-Si-N. In order to understand that, the heat of formation of $TaSi_2$, TaN and Ta_2O_5 are compared in Table 6-4. Compared to $TaSi_2$, TaN has higher heat of formation, and thus more stable. It prevents the reaction between barrier and Si substrate when barrier crystallization and Cu diffusion happens.

Table 6-4 Heat of formation of Ta compounds

Compounds	Heat of formation, ΔH, kJ/mol
$TaSi_2$	-46.0
Ta_2O_5	-2046.0
TaN	251.1

b) The non-reactivity between barrier and substrate is critical. Barrier which does not react with Si provides better barrier performance than barrier with potential reaction with Si.

Among all the studied films, Ta-Cr showed similar crystallization temperature as Ta-N and Ta-Ti, but it shows severe loss of interface integrity during breakdown compared with the other two barriers. The fact that $CrSi_x$ forms during Ta-Cr barrier breakdown indicates the influence of the reactivity between the barrier and the substrate materials. In contrast, there was no reaction between the barriers and substrates for the other two candidates.

6.5. Summary

This Chapter studies the barrier performance of the two groups of Ta-based thin films, namely, compound barriers and binary alloy barriers. Ta-Si-N provides the best barrier performance, but with a sacrifice in electrical resistivity. The good barrier performance of Ta-Si-N was because of the amorphous structure and high thermal stability. In spite

of the good barrier performance, the high electrical resistance makes it not suitable for practical barrier application.

On the other hand, Ta-TM shows comparable barrier performance with Ta-N, with lower electrical resistance. As a comparison among Ta-Ni, Ta-Cr and Ta-Ti, the performance of Ta-Ni as Cu diffusion barrier is the best. It is attributed to the highly stable amorphous structure of Ta-Ni. On the other hand, Cr reacts with Si to form $CrSi_x$. Ti has no effect to amorphorize Ta because of the small atomic size difference. Thus as a result, Ta-Cr and Ta-Ti show early breakdown compared to Ta-Ni. A general trend is observed, that the higher glass forming ability will result in better Cu diffusion barrier performance.

As summarized from the current work, a good candidate for thin film diffusion barrier needs to fulfill a few criteria: 1) The barrier needs to be amorphous thin film. 2) The barrier elements need to be inert with the substrate element to maintain interface integrity.

Chapter 7. Effect of Oxygen on Thin Film Properties and Barrier Performance

As observed in Chapter 4- Chapter 6, O was observed in most of the films at as-deposited state. As reported in previous works, O is commonly incorporated in thin films deposition. However, the source of the O is still under debate. The effect of oxygen in the thin films properties and barrier performance is not reported either. Therefore, in this chapter, Ta-Ni films containing different O concentrations are intentionally formed to study the source of the O and its effect on thermal stabilities as well as Cu diffusion barrier performances of Ta-Ni films.

7.1. Effect of O on the properties Ta-Ni thin films

7.1.1. Change of Ta-Ni composition with substrate bias applied during film deposition

The composition of all deposited films is summarized in Table 7-1. Oxygen of around 5 at% was observed in film without substrate bias. The observation of O has been discussed during studies of Ta-Si-N and Ta-N. The reason is Ta has high affinity with O. But the sources of O remains unknown, thus worth further exploration. With RF power applied on the substrate during Ta-Ni deposition, the O concentration reduced drastically to around 1 at% at 50 W, with no further significant change in O concentration at 75W and 100W. The reason of the O concentration change will be discussed later.

Table 7-1 Composition and electrical resistivity of Ta-Ni films with different substrate RF power

Bias Power (W)	Composition (at%)	Electrical resistivity (μΩ·cm)	Ta: Ni ratio	Sample annotation
0	Ta 66.33, Ni 28.42, O 5.25	410.4 ± 26.4	2.33	$Ta_{66.33}Ni_{28.42}O_{5.25}$
25	Ta 68.28, Ni 26.83, O 4.89	217.3 ± 4.8	2.54	$Ta_{68.28}Ni_{26.83}O_{4.89}$
50	Ta 72.58, Ni 26.47, O 0.95	238.8± 4.2	2.74	$Ta_{72.58}Ni_{26.47}O_{0.95}$
75	Ta 71.97, Ni 26.42, O 1.61	211.5 ± 1.8	2.72	$Ta_{71.97}Ni_{26.42}O_{1.61}$
100	Ta 72.02, Ni 26.89, O 1.09	217.6 ± 2.5	2.68	$Ta_{72.02}Ni_{26.89}O_{1.09}$

Besides the change of O concentration, a variation of Ta: Ni ratio was also observed when the substrate bias changed, as in Table 7-1. When the substrate power increased from 0 W to 50 W, Ta to Ni ratio increased from 2.33 to 2.74. At substrate power of 50 W and higher, the Ta to Ni ratio stabilized. The variation of Ta to Ni ratio could be due to the etching effect when the substrate is biased during sputtering. Similar as that for O atom, substrate bias applied results in etching effect of Ta and Ni atoms deposited on Si substrate. Two competitive processes coexist during the deposition process, the adsorption of Ta and Ni atoms on substrate as in sputtering deposition, and the sputter etching of Ta and Ni from substrate due to the substrate bias. Due to the difference in atomic weight, the sputter etching rate of Ta and Ni is different. At a certain RF power, the sputtering rate of Ni is faster than that of Ta, because Ni has lower atomic size and weight. At higher substrate RF power, Ni removal rate increases faster than Ta removal rate. It results in higher Ta to Ni ratio at higher substrate bias. However, it was observed that the effect shows no further improvement at 50 W and above, with stabilization of the Ta to Ni ratio.

The depth profile of the two Cu/Ta-Ni/Si stacks with 0 W and 100W substrate bias were measured by SIMS, as shown in Fig. 7-1. A different O peak in the Ta-Ni layer was observed for the two samples. While oxygen intensity in Ta-Ni deposited with substrate bias was negligible, the oxygen intensity in Ta-Ni deposited without substrate bias was relatively high. This clearly shows that the difference of oxygen measured by EDX is due to the different oxygen concentration in Ta-Ni layer. It is obviously due to the different RF bias applied on substrate during thin film deposition. Because of the Cu protective layer, it is believed there is no in-diffusion of oxygen after film formation. Thus the only possible source of oxygen is the oxygen residue in the sputtering chamber.

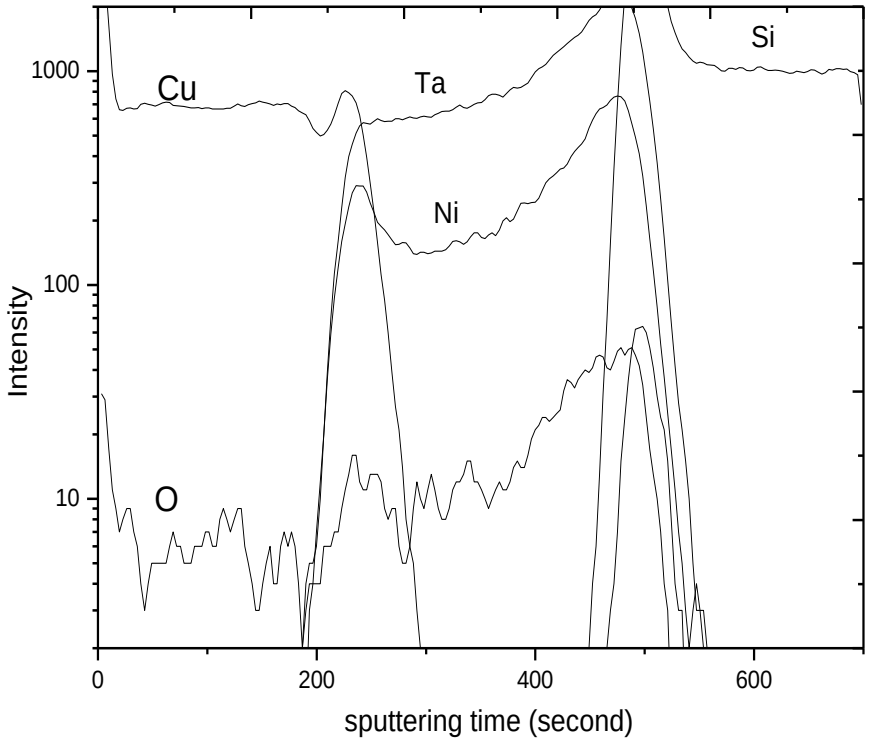

(a)

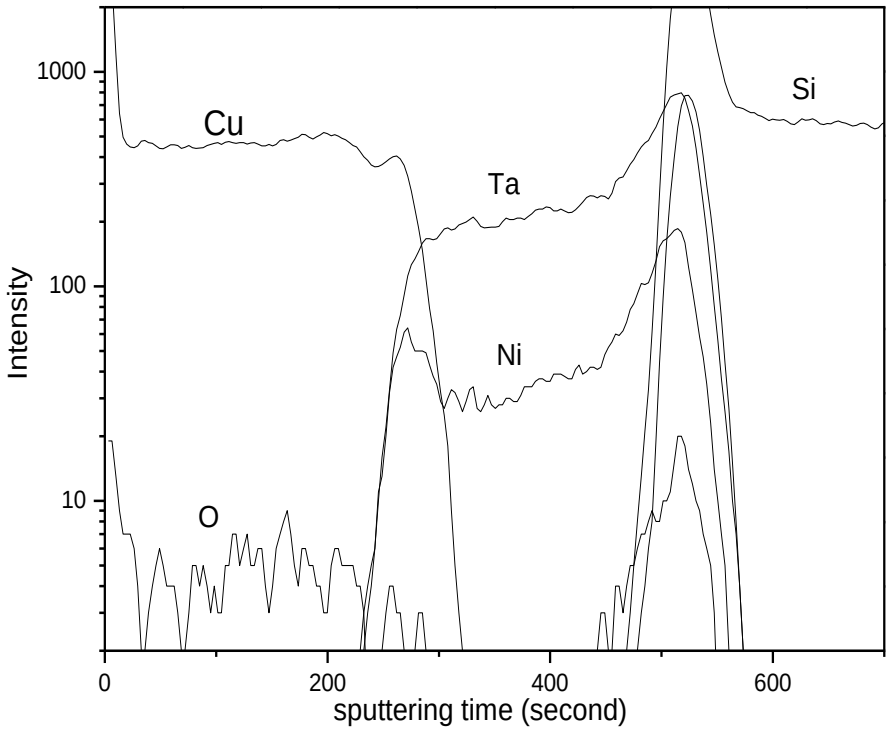

(b)

Fig. 7-1 ToF-SIMS depth profile of elements Cu, Ta, Ni, O and Si of the as-deposited Cu/Ta-Ni/Si stacks with substrate bias of (a) 0W; (b) 100W.

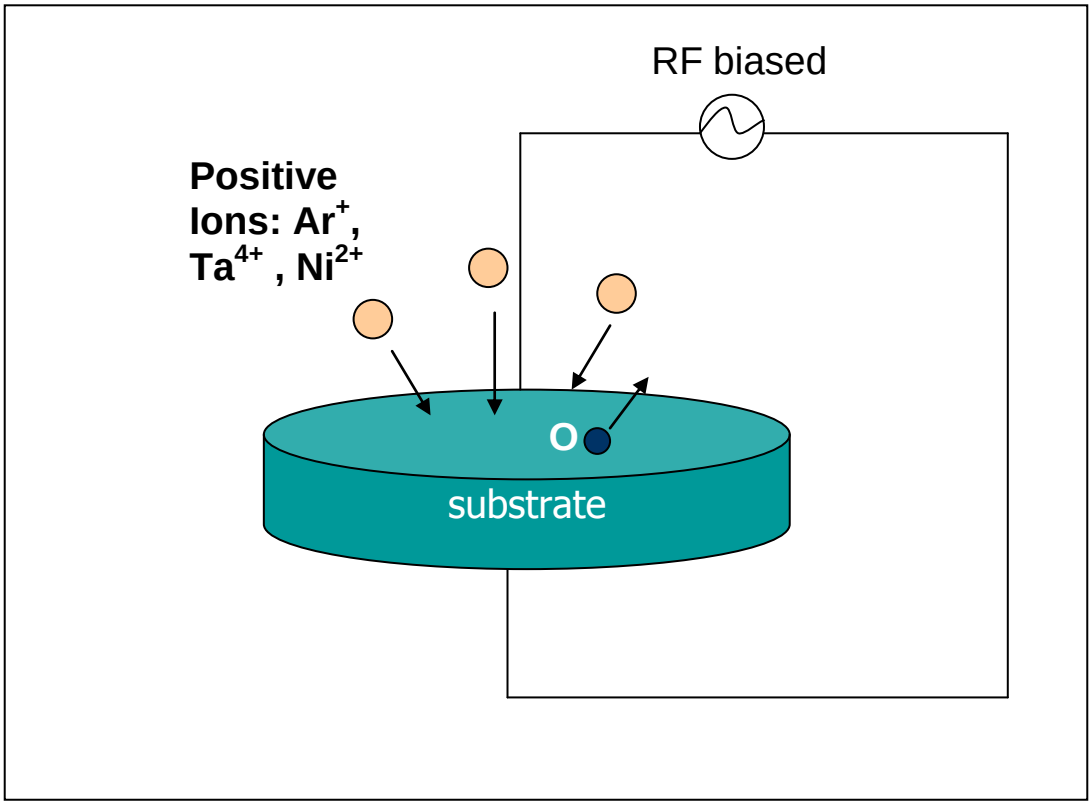

Fig. 7-2 Oxygen depletion mechanism with substrate RF bias applied during Ta-Ni film deposition

The oxygen depletion mechanism under substrate RF bias is explained by Fig. 7-2. During Ta-Ni film deposition, in spite of the high vacuum, there is still small amount of oxygen residue. When the high energy plasma is ignited, the oxygen residue will be active by the plasma, and adsorbed on substrate surface together with Ta and Ni atoms. It will result in the incorporation of oxygen into the Ta-Ni films. However, when a substrate RF bias is applied, the light weight species such as oxygen will be sputtered off from the Si substrate as a result of low energy bombardment, which reduces the oxygen concentration in Ta-Ni. As a result, Ta-Ni film with low oxygen concentration is obtained when substrate bias is applied during Ta-Ni deposition.

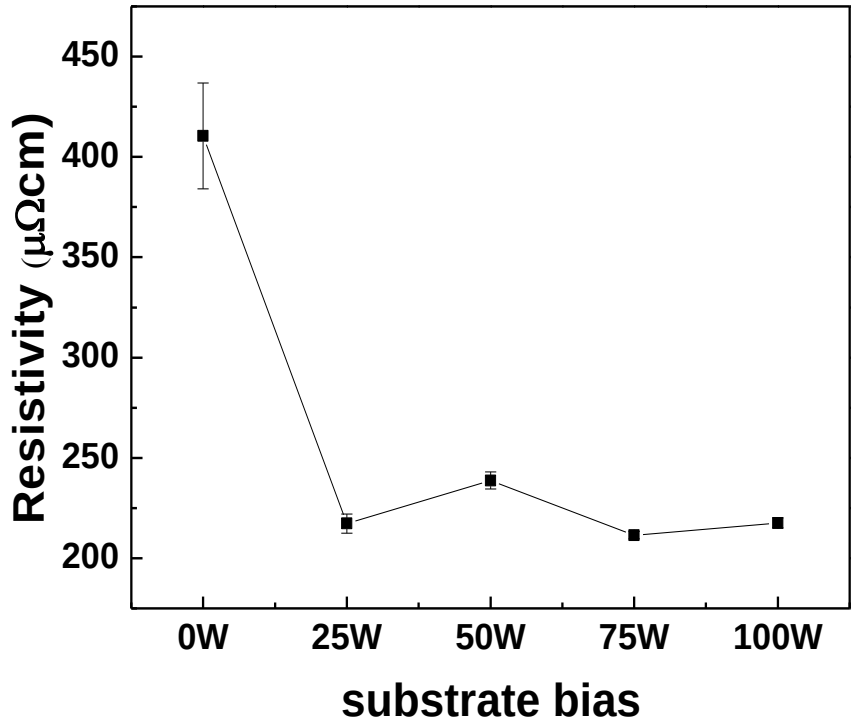

Fig. 7-3 Resistivity of as-deposited Ta-Ni thin films with substrate bias change

7.1.2. Effect of oxygen concentration on Ta-Ni film properties

7.1.2.1. Effect of oxygen concentration on electrical resistance of the Ta-Ni/Si

Fig. 7-3 shows the change of electrical resistivity with substrate bias. There was a reduction of resistivity from 410.4 μΩ·cm to 211.5 μΩ·cm as substrate bias increased from 0 W to 50 W. The change of resistivity is largely affected by the substrate bias. It could be the result of densification of the film and the change of oxygen concentration. When the oxygen concentration was lower than ~1 at% at substrate bias of 50 W and higher, the change of resistivity was insignificant. This concludes that the electrical resistivity is proportional to the oxygen concentration, and higher oxygen

concentration leads to higher resistivity. This can be explained by that high oxygen concentration reduces the free electron movement in alloy thin films and increases resistivity. It was also noticed that at 25W bias, the resistivity of the film is similar as the films deposited at 50 - 100 W, in spite that the film has higher oxygen concentration. It is attributed to the light ion bombardment which results in denser thin film and reduces the resistivity. Further investigation is needed for more understanding.

XRD patterns of Ta-Ni films formed with different substrate RF bias are shown in Fig. 7-4 . Similar to the previously discussed Ta-TM film, films studied in this chapter also showed amorphous phase, as indicated by the broad amorphous peaks at 39.2°. No shift of amorphous peaks was observed for the films. It shows the concentration of oxygen does not affect the average first-order inter-atomic spacing for the amorphous Ta-Ni films. It is because of the small atomic size of oxygen and also the low oxygen concentration in the films.

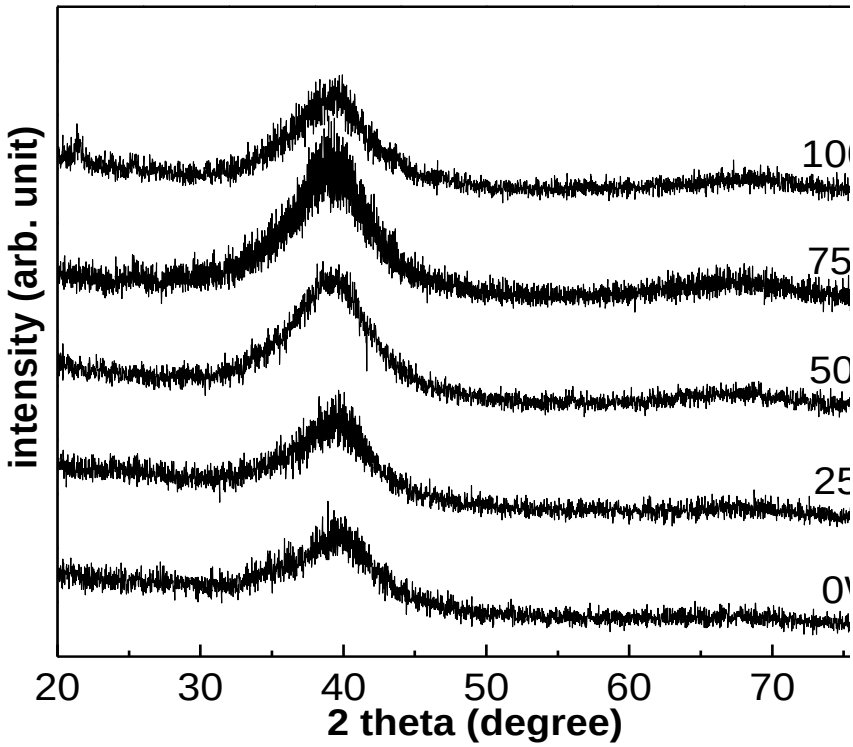

Fig. 7-4 XRD diffraction patterns of the as-deposited Ta-Ni thin films with substrate bias at 0 W to 100 W

7.1.2.2. Effect of oxygen concentration on the microstructure evolution and the interfacial stability of the Ta-Ni/Si structure

In order to study the effect of oxygen concentration on the microstructures and stabilities of the Ta-Ni films, 3 groups of Ta-Ni/Si were studied with different oxygen concentration, including 0.95 at%, 4.89 at% and 5.25 at%. They were annotated by the composition, i.e. $Ta_{72.58}Ni_{26.47}O_{0.95}$, $Ta_{68.28}Ni_{26.83}O_{4.89}$ and $Ta_{66.33}Ni_{28.42}O_{5.25}$, in the discussion below. The films were annealed in vacuum at temperatures of 700 °C, 750 °C to 800 °C.

The XRD plots of Ta-Ni/Si films after annealing are shown in Fig. 7-5. All films remained amorphous at 700 °C. At 750 ˚C, multiple Ta phases from 33.5˚ to 42.5˚ were observable in all films. In low-oxygen $Ta_{72.58}Ni_{26.47}O_{0.95}$, $TaSi_2$ peaks at 21.5° and 25.4° were observed, while in oxygen-rich $Ta_{68.28}Ni_{26.83}O_{4.89}$ and $Ta_{66.33}Ni_{28.42}O_{5.25}$, there was no $TaSi_x$ observed. In $Ta_{68.28}Ni_{26.83}O_{4.89,}$ Ta_2O_5 peaks were observable at 23.1° and 28.3°. In $Ta_{66.33}Ni_{28.42}O_{5.25,}$ no other crystalline phase was observed besides the Ta phases. Comparing the different behavior of oxygen-rich and oxygen-lean Ta-Ni films, it is noted that oxygen possesses positive effect stabilizing the interface between Ta-Ni and Si substrate. The retardation could be attributed to the "stuffing" effect of oxygen. No Ta_2O_5 peaks were present in $Ta_{68.28}Ni_{26.83}O_{4.89}$ sample annealed at 800 °C. It indicates that $TaSi_2$ is more stable at 800 °C above compared to Ta_2O_5, which was formed at 750 ºC and vanished at 800 °C. On the other hand, Ta_2O_5 peaks were only observed at 800 °C in $Ta_{66.33}Ni_{28.42}O_{5.25}$. $NiSi_2$ was also observed in $Ta_{66.33}Ni_{28.42}O_{5.25}$ and $Ta_{68.28}Ni_{26.83}O_{4.89}$ after 800 °C annealing.

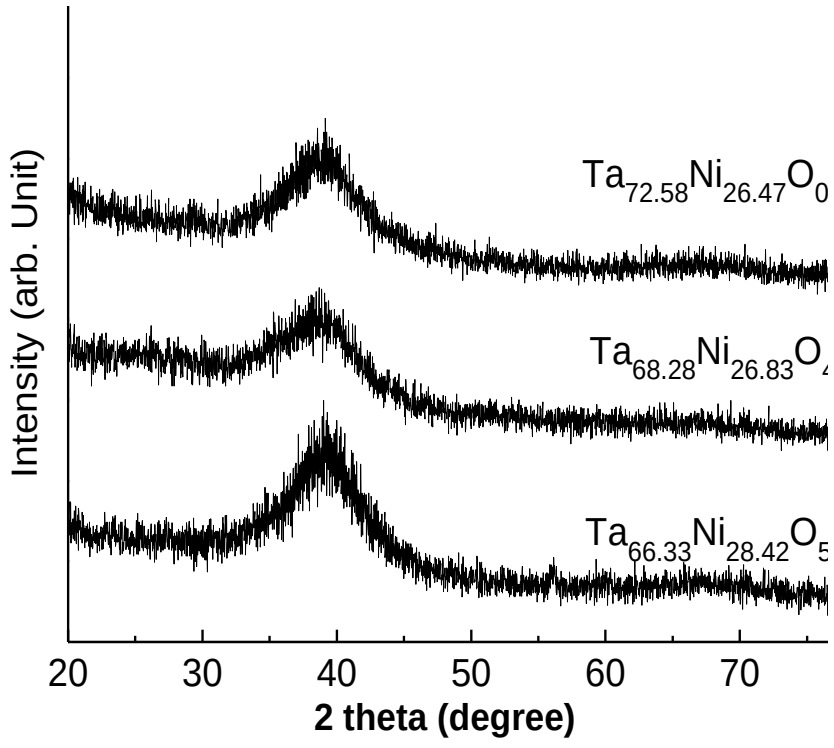

(a)

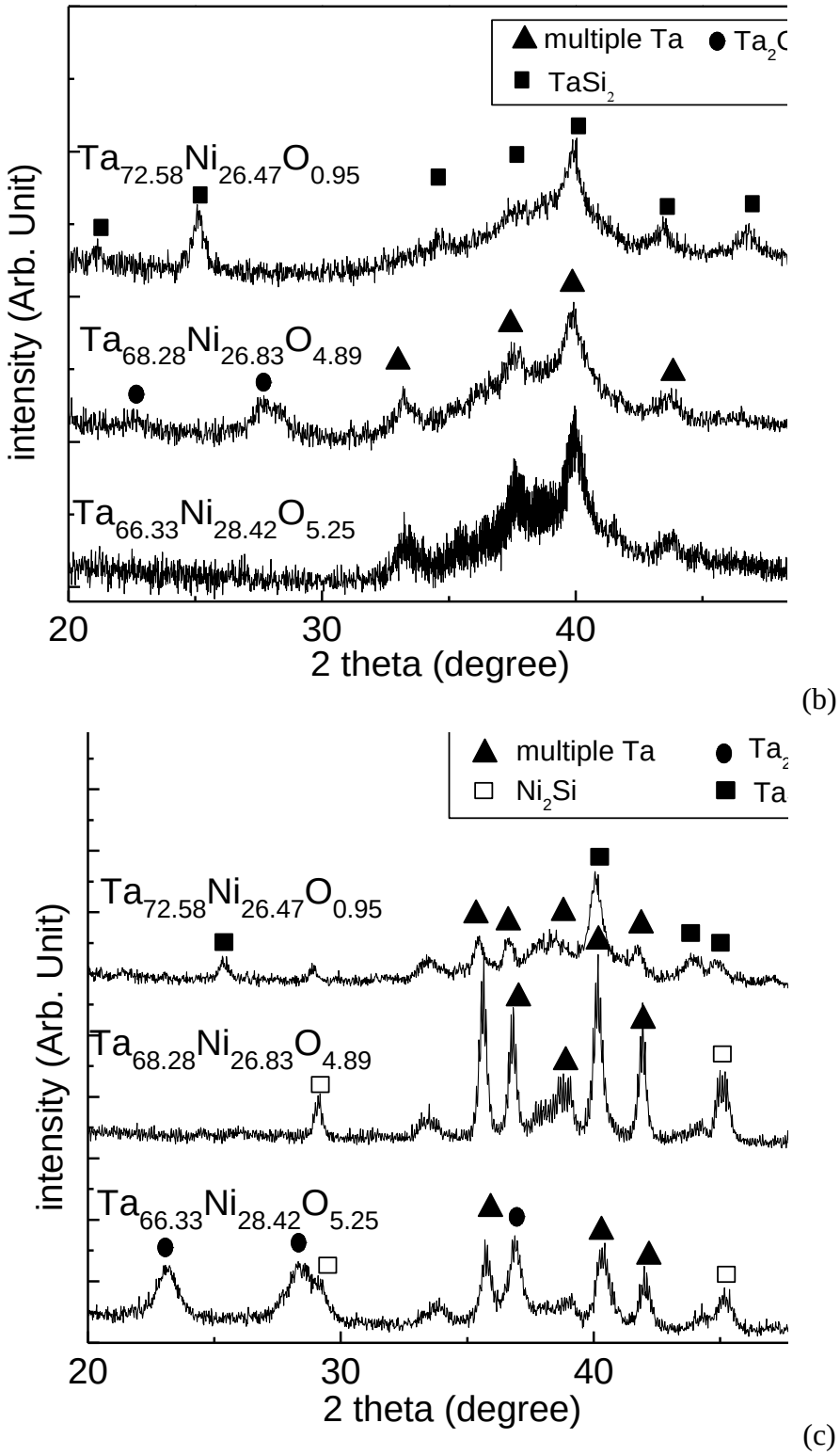

Fig. 7-5 XRD diffraction patterns of the Ta-Ni/Si films with different oxygen concentration annealed in vacuum at (a) 700 °C; (b) 750 °C; (c) 800 °C

The TEM pictures in Fig. 7-6 show interface evolution of $Ta_{66.33}Ni_{28.42}O_{5.25}$/Si and $Ta_{72.58}Ni_{26.47}O_{0.95}$/Si after annealing. At 700 ºC, in both samples there was a thin layer of silicon oxide, with thickness of about 3nm. It is the native silicon oxide because there was no HF cleaning to remove the oxide during substrate preparation. There was no crystalline phase in both films. At 750 °C, the native oxide in $Ta_{66.33}Ni_{28.42}O_{5.25}$/Si was still observable, while in $Ta_{72.58}Ni_{26.47}O_{0.95}$/Si, the native oxide became indistinguishable. Different crystalline peaks were observable in $Ta_{72.58}Ni_{26.47}O_{0.95}$ film, while the crystalline phase was not observable $Ta_{66.33}Ni_{28.42}O_{5.25}$ film. At 800 °C, the oxide layer in $Ta_{66.33}Ni_{28.42}O_{5.25}$/Si remained, with different crystalline phases. They are found to be Ta_2O_5, Ta and $NiSi_2$ in the Ta-Ni film. As a contrast, the interface between barrier and substrate were not distinguishable for $Ta_{72.58}Ni_{26.47}O_{0.95}$. The reaction is caused by diffusion of Si into Ta-Ni film as shown by the appearing of $TaSi_2$ and $NiSi_2$ crystals in the XRD. The finding is consistent with the observation in XRD. It shows that oxygen concentration helps in improving the interface stability between substrate and barrier. It helps hindering the interface reaction.

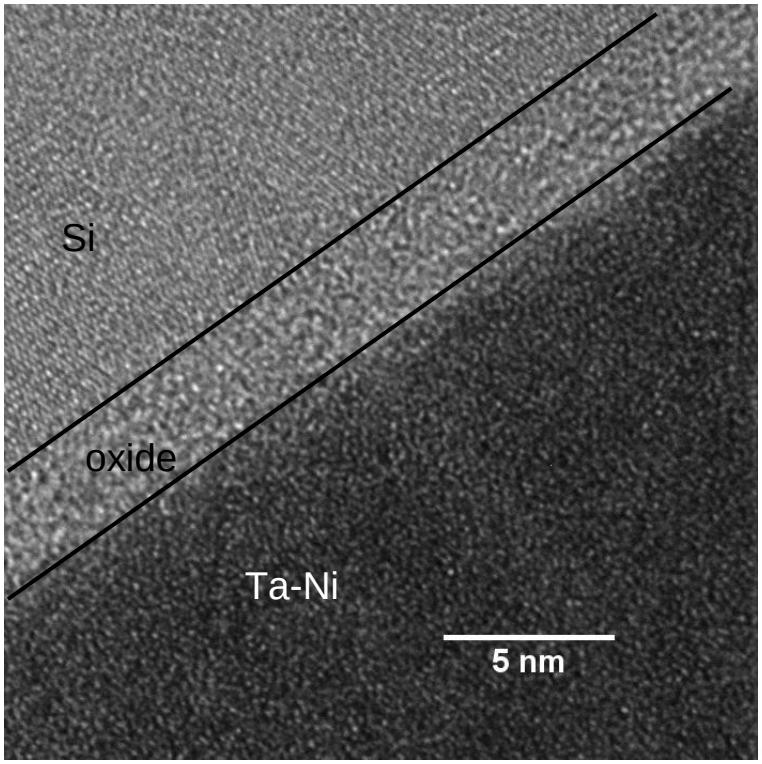

(a)

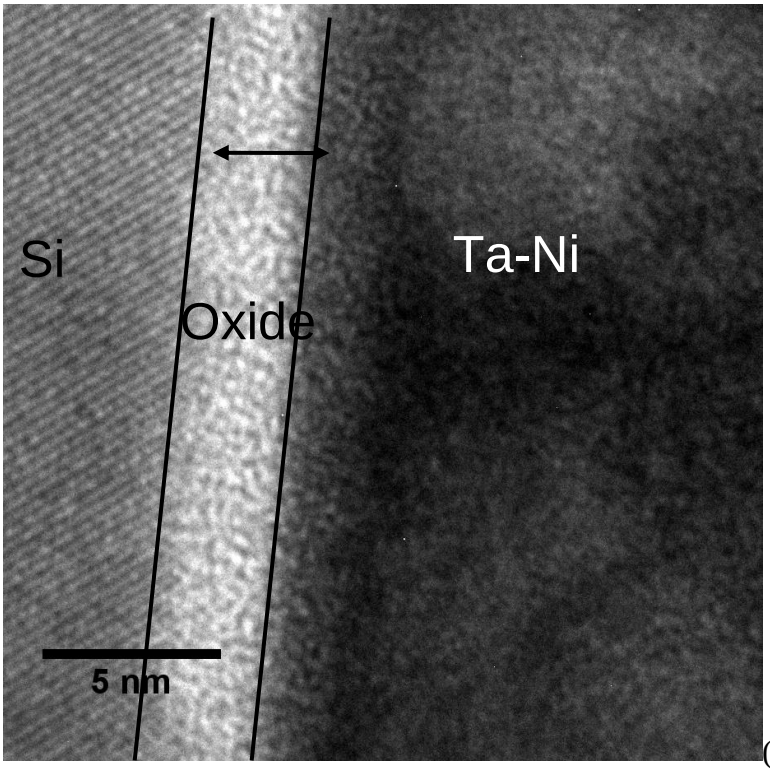

(b)

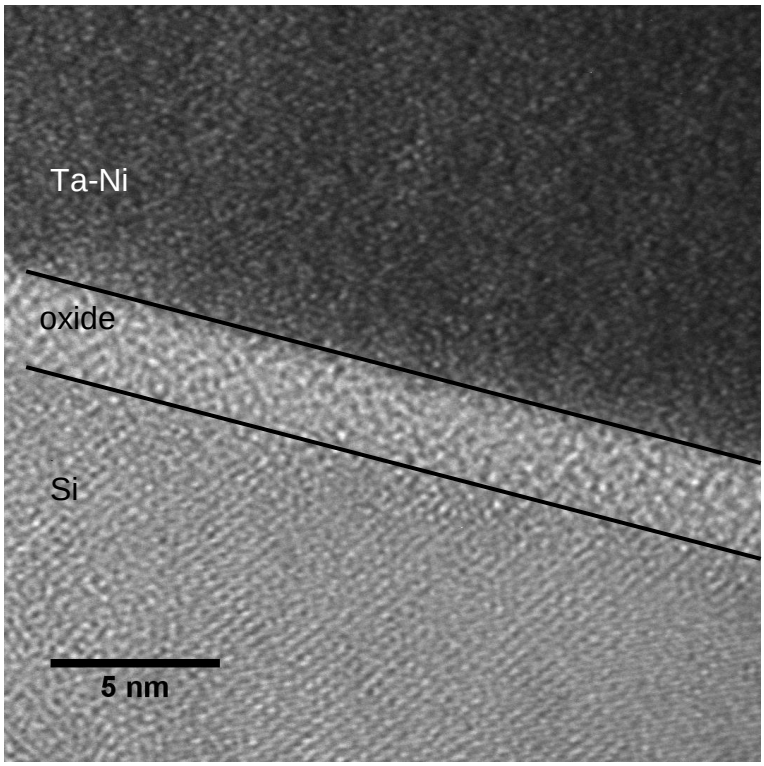

(c)

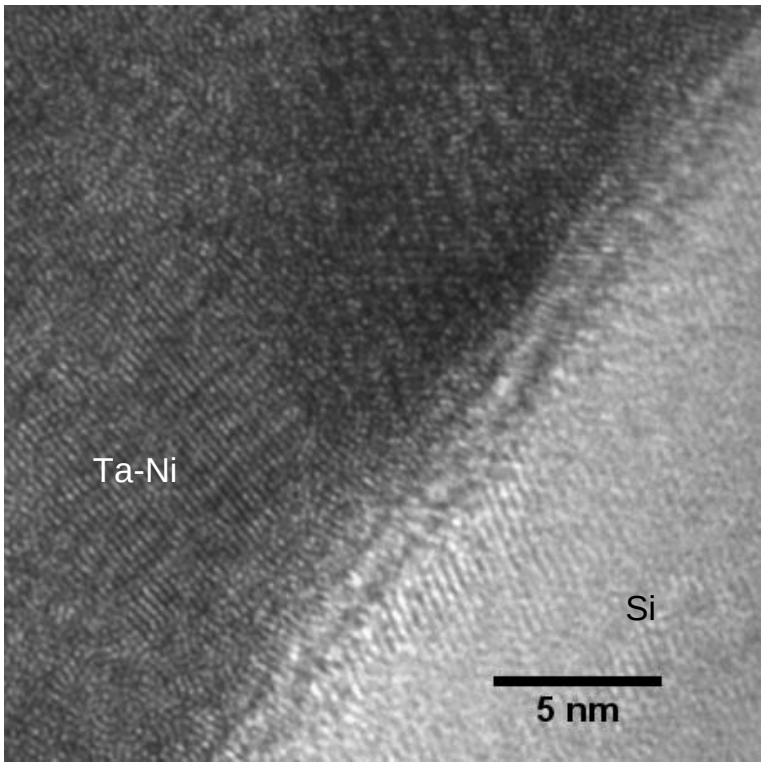

(d)

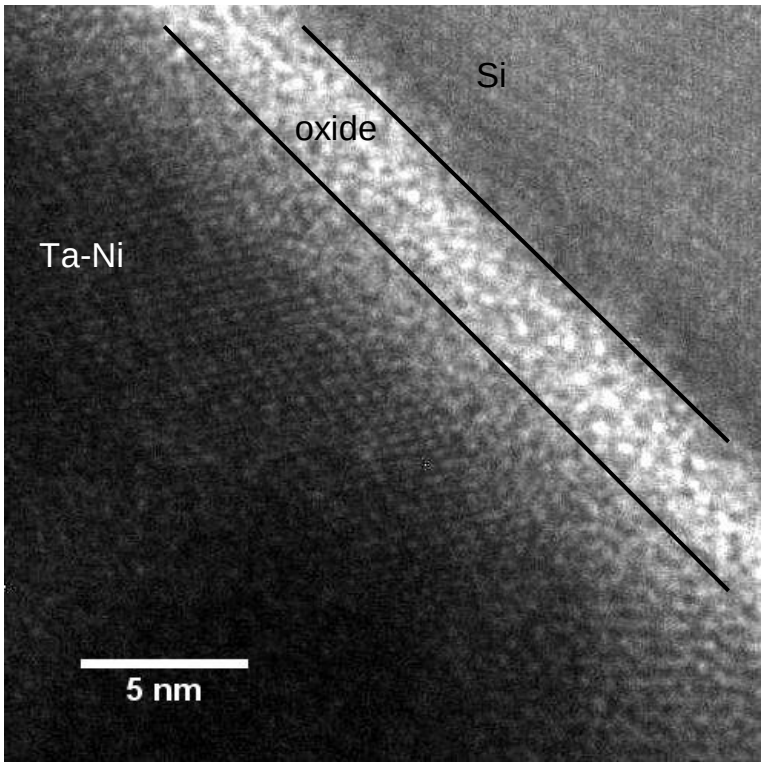

(e)

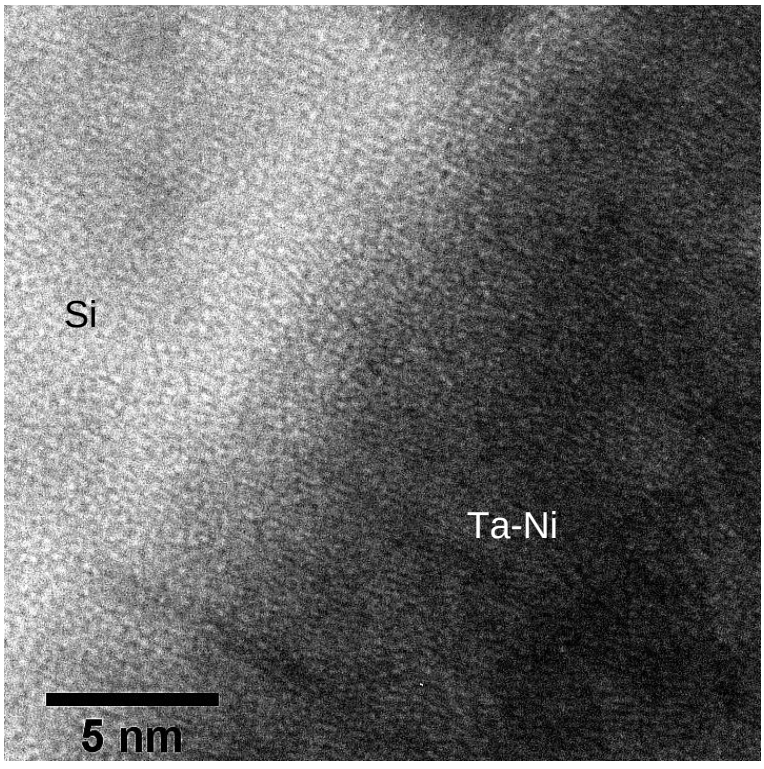

(f)

Fig. 7-6 TEM image of Ta-Ni/Si interface of (a) $Ta_{66.33}Ni_{28.42}O_{5.25}$ annealed at 700 °C; (b) $Ta_{72.58}Ni_{26.47}O_{0.95}$ annealed at 700 °C; (c) $Ta_{66.33}Ni_{28.42}O_{5.25}$ annealed at 750 °C; (d) $Ta_{72.58}Ni_{26.47}O_{0.95}$ annealed at 750 °C; (e) $Ta_{66.33}Ni_{28.42}O_{5.25}$ annealed at 800 °C; (f) $Ta_{72.58}Ni_{26.47}O_{0.95}$ annealed at 800 °C.

7.1.3. Discussion

As discussed in this part, oxygen incorporated in the barrier shows positive effect in the stability of amorphous Ta-Ni film. As the presence of oxygen is inevitable in most of film deposition, it is thus of significant importance to understand the effect. For Ta-Ni, the effect of oxygen mainly hinders the interfacial reaction between Ta-Ni and Si. The mechanism is attributed to the high heat of formation of Ta_2O_5. At elevated temperature, crystallization of Ta_2O_5 stabilized the Ta-Ni films, and retards the reaction between Ta and Si. The reaction hierarchy is following the sequence of crystallization → Ta_2O_5 → $TaSi_x$ and $NiSi_x$. Thus the effect of oxygen in Ta-Ni films is on the improvement of Ta-Ni/Si interfacial stability by consuming less oxygen from the native oxide at Ta-Ni/Si interface, rather than stabilization of the amorphous structure. In film with 1 at% oxygen, interfacial reaction is triggered after the native oxide at Ta-Ni/Si interface is consumed, probably due to formation of Ta_2O_5, while in films with 5 at% oxygen, the native oxide is stable even when $TaSi_x$ and $NiSi_x$ form by Si in-diffusion to Ta-Ni layers.

It is believed that the oxygen in Ta-Ti and Ta-Cr showed similar effect as that in Ta-Ni. in terms of film stability and barrier performance. Since it is not possible to fully impede oxygen from the thin film formation process, it is more practical to discuss the behavior of Ta-TM films without special treatment to remove the oxygen.

7.1.4. Summary

Ta-Ni films with various oxygen content are studied in this part. The oxygen content was controlled by applying different RF bias during Ta-Ni deposition from 0 W to 100 W. Ta-Ni without substrate bias contains about 5 at% oxygen. The oxygen

concentration drops to about 1 at% as the substrate bias increases to 50 W. Further increase of substrate bias has no significant effect on the oxygen content. SIMS study confirmed that the oxygen was incorporated during film deposition from the oxygen residue inside sputtering chamber. Ta-Ni films with higher oxygen content show higher electrical resistivity. No significant effects of oxygen was observed on the stability of the amorphous Ta-Ni film, as all as-deposited amorphous films crystallized at 750 °C. However films with higher oxygen concentration showed higher interfacial stability, as indicated by the retardation of $TaSi_2$ formation. $TaSi_2$ formed at 800 °C for Ta-Ni films with high oxygen content, compared to 750 °C for Ta-Ni films with low oxygen content. The interfacial stability loss was confirmed and further illustrated by TEM. Oxygen in Ta-Ni films shows beneficial effect, as it stabilizes the Ta-Ni films, and helps retarding the interfacial reaction between the thin film and substrate. However, the benefit comes with the penalty of higher electrical resistance.

7.2. Effect of Oxygen on Cu Diffusion Barrier Performance

As summarized above, oxygen was observed in deposited Ta-Ni due to the high tendency of Ta to react with even small amount of oxygen residue in the sputtering chamber. The small amount of oxygen helps in improving the interface stability of the Ta-Ni films. It was found that the reaction between barrier and substrate occurs at 750 °C for O rich Ta-Ni, while for O depleted Ta-Ni, the interfacial reaction occurs at 700 °C [152]. In the current part, the effect of oxygen in Cu diffusion barrier performance is discussed.

It has been reported that small amount of oxygen could be introduced into Ta-based Cu diffusion barrier deposited by PVD propcess [101]. The incorporation of oxygen helps stabilize Cu diffusion barrier [137, 153-154]. In Ta(O)/Cu, TaO_x formation at interface

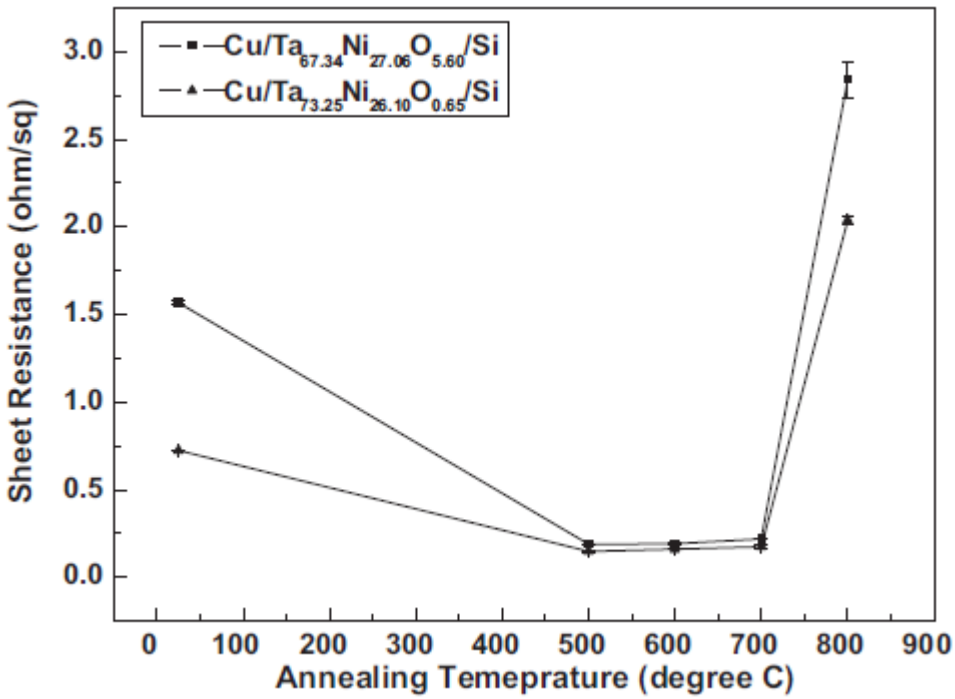

Fig. 7-7 Resistance evolution with temperature for Cu/ $Ta_{67.34}Ni_{27.06}O_{5.60}$ Si and Cu/ $Ta_{73.25}Ni_{26.10}O_{0.65}$/Si

of Ta(O)/Cu after annealing was also reported. It was believed to be contributing to the improved barrier performance [154]. The mechanism of the enhancement was not discussed in these early reports.

Films deposited without substrate bias were found to contain oxygen of 5.6 at%, while the ones without substrate bias contain 0.65 at% oxygen. The depletion of oxygen in film with substrate bias is due to the sputter-etching effect of substrate bias, as discussed previously. In this part, the two films were annotated by the composition, namely $Ta_{67.34}Ni_{27.06}O_{5.60}$ and $Ta_{73.25}Ni_{26.10}O_{0.65}$ for simplicity thereafter.

7.2.1. Resistance Evolution

The sheet resistance measured by 4-point probing system of the two Cu/Ta-Ni/Si samples at room temperature and after annealing is shown in Fig. 7-7. Cu/$Ta_{67.34}Ni_{27.06}O_{5.60}$ showed higher sheet resistance than Cu/$Ta_{73.25}Ni_{26.10}O_{0.65}$/Si for fresh sample. The resistivity of $Ta_{67.34}Ni_{27.06}O_{5.60}$ was higher than $Ta_{73.25}Ni_{26.10}O_{0.65}$ due to the oxygen stuffing, hence Cu/ $Ta_{67.34}Ni_{27.06}O_{5.60}$ shows higher sheet resistance than Cu/ $Ta_{73.25}Ni_{26.10}O_{0.65}$/Si. At 500 °C, both films showed lower resistance, and the difference between the two also reduced. The drop of resistance is resulted from the Cu crystals growth during the annealing treatment, which is also observed in XRD measurement to be discussed later. Slight increase of resistance was observed at 600 °C and 700 °C. The subtle increase of resistance could be an indication of the microstructure change or interfacial reaction. At 800 °C, drastic increase of resistance was observed for both samples. It shows the loss of Cu integrity and also suggests the failure of Cu diffusion barrier for both samples at 800 °C.

7.2.2. Microstructure Evolution

XRD spectroscopy for Cu/$Ta_{67.34}Ni_{27.06}O_{5.60}$ /Si and Cu/$Ta_{73.25}Ni_{26.10}O_{0.65}$/Si samples before and after annealing are shown in Fig. 7-8. Only Cu (111) peaks are observed for both samples at temperatures below 700 °C. That shows the Ta-Ni films remained amorphous below 700 °C. Growth of the Cu crystals was shown by the narrowing of FWHM (the full width at half maximum) of Cu (111) peaks. It explains the resistance drop at 600 °C, as larger Cu grains lead to higher conductivity. The differentiation of two films was observed when they were annealed at 700 °C. In Cu/$Ta_{73.25}Ni_{26.10}O_{0.65}$/Si, no other crystalline phase was observed besides Cu (111) peak, while in Cu/$Ta_{67.34}Ni_{27.06}O_{5.60}$/Si, Ta_2O_5 peaks were observed at 700 °C. As to be discussed later, nano-sized Cu_3Si was observed at $Ta_{73.25}Ni_{26.10}O_{0.65}$/Si substrate, while the interfaces of $Ta_{67.34}Ni_{27.06}O_{5.60}$/Si remain distinct. It needs to point out that the

Cu_3Si was not detected by XRD. It could be due to the grain size which was less than 10 nm. At 800 °C, the Cu_3Si crystalline peaks at 44.6° and 45.0° were observed for both samples, together with other crystalline phases, $TaSi_2$ and Cu_3Si for $Cu/Ta_{73.25}Ni_{26.10}O_{0.65}/Si$ and Ta_5Si_3 and Cu_3Si for $Cu/ Ta_{67.34}Ni_{27.06}O_{5.60}/Si$. The observation of Cu_3Si in both samples showed the catastrophic failure for both $Ta_{73.25}Ni_{26.10}O_{0.65}$ and $Ta_{67.34}Ni_{27.06}O_{5.60}$ barriers. It explained the drastic growth of electrical resistance at 800 °C for both samples.

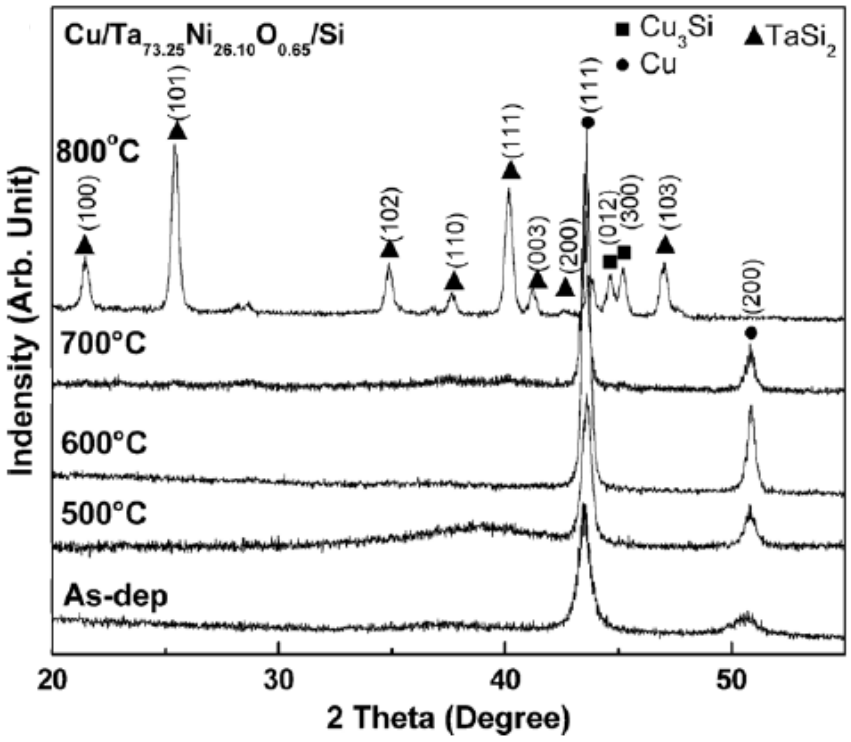

(a)

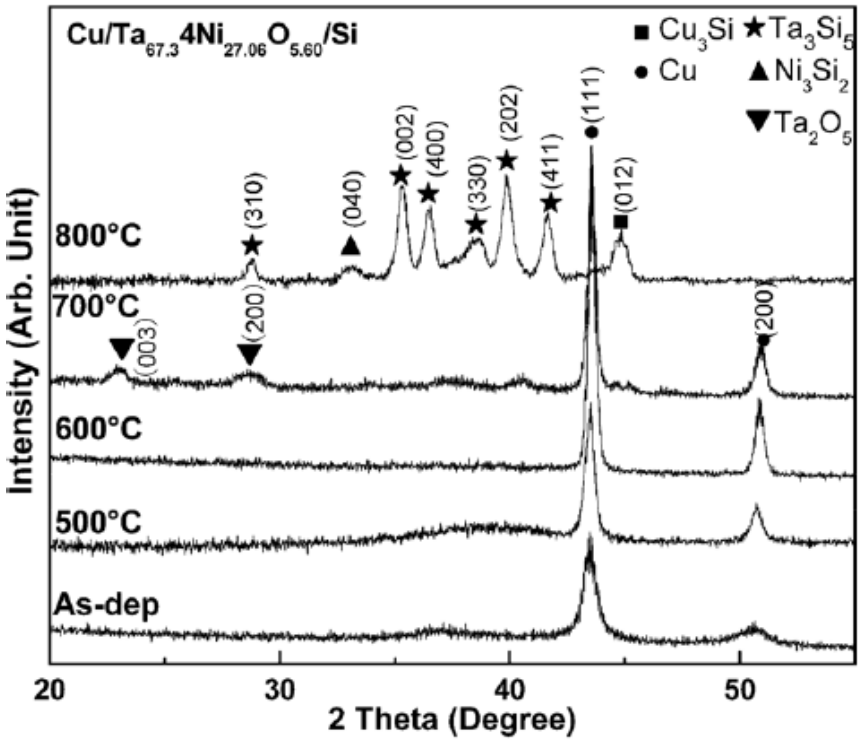

(b)

Fig. 7-8 XRD diffraction pattern of Cu/ $Ta_{73.25}Ni_{26.10}O_{0.65}$/Si and Cu/ $Ta_{67.34}Ni_{27.06}O_{5.60}$/Si annealed in vacuum at 500 °C to 800 °C

7.2.3. Diffusion profile after annealing

The films were scanned by SIMS to understand the diffusion of various elements at different annealing temperatures. As shown in Fig. 7-9, an abrupt graduating of depth profile was observed for all elements for non-annealed samples. It marked the interface between each layers. Remarkable oxygen was detected in Ta-Ni layer of Cu/ $Ta_{67.34}Ni_{27.06}O_{5.60}$/Si, while the oxygen peak was negligible in same layer for Cu/ $Ta_{73.25}Ni_{26.10}O_{0.65}$/Si. The observation further verified the difference of oxygen concentration in EDX observation. In Cu/$Ta_{73.25}Ni_{26.10}O_{0.65}$/Si, small oxygen peak belonging to the residue SiO_2 was observed at the Ta-Ni/Si interface. At 600 °C, diffusion of Cu into Ta-Ni layer for both samples was observed. Cu did not diffuse through the barrier layer at 600 °C, as there was no intersection between Cu and Si

profile. At 700 °C, the intersection between Cu and Si profiles was observed, showing the diffusion of Cu through the barrier into the Si layer. The diffusion of Cu in $Ta_{67.34}Ni_{27.06}O_{5.60}$ and $Ta_{73.25}Ni_{26.10}O_{0.65}$ film was different. For $Ta_{67.34}Ni_{27.06}O_{5.60}$ barrier, the Cu diffusion profile changed slope at the $Ta_{67.34}Ni_{27.06}O_{5.60}$/Si interface, showing the confinement of Cu in Ta-Ni film. This suggests that the concentration of Cu at $Ta_{67.34}Ni_{27.06}O_{5.60}$/Si interface is not high enough to trigger fast reaction between Si and Cu. As a contrast, In the Cu/$Ta_{73.25}Ni_{26.10}O_{0.65}$/Si stack, accumulation of Cu was observed at the Ta-Ni/Si interface, as suggested by the high Cu peak at the Ta-Ni/Si interface. This was later confirmed by TEM observation, that Cu_3Si nano-crystals were observed at Ta-Ni/Si interface. This may suggest that Cu diffusion in $Ta_{73.25}Ni_{26.10}O_{0.65}$/Si at 700 °C was faster than that in $Ta_{67.34}Ni_{27.06}O_{5.60}$/Si, and the concentration of Cu at $Ta_{73.25}Ni_{26.10}O_{0.65}$/Si was higher than that of $Ta_{67.34}Ni_{27.06}O_{5.60}$/Si, thus resulted in the formation of Cu_3Si at $Ta_{73.25}Ni_{26.10}O_{0.65}$/Si interface.

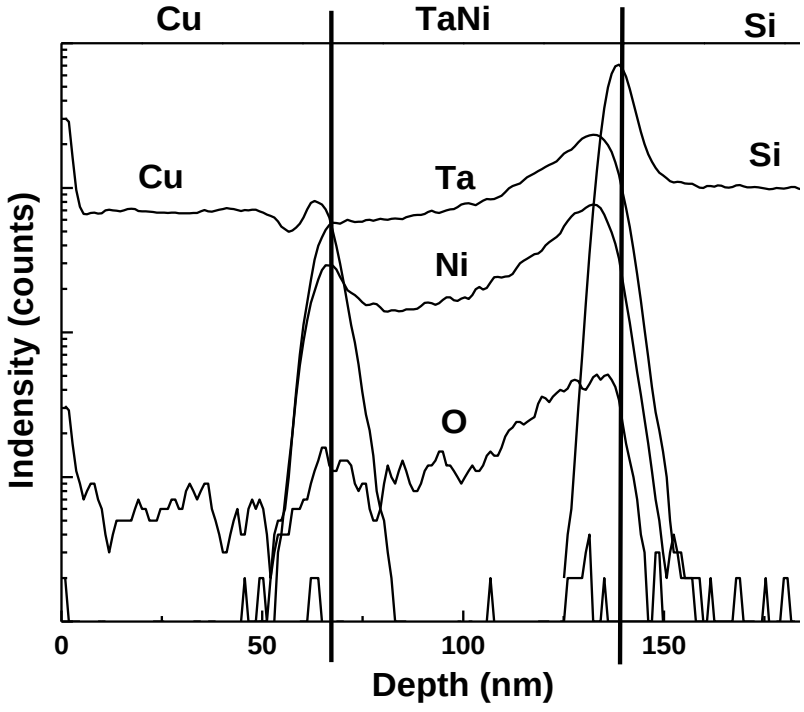

(a)

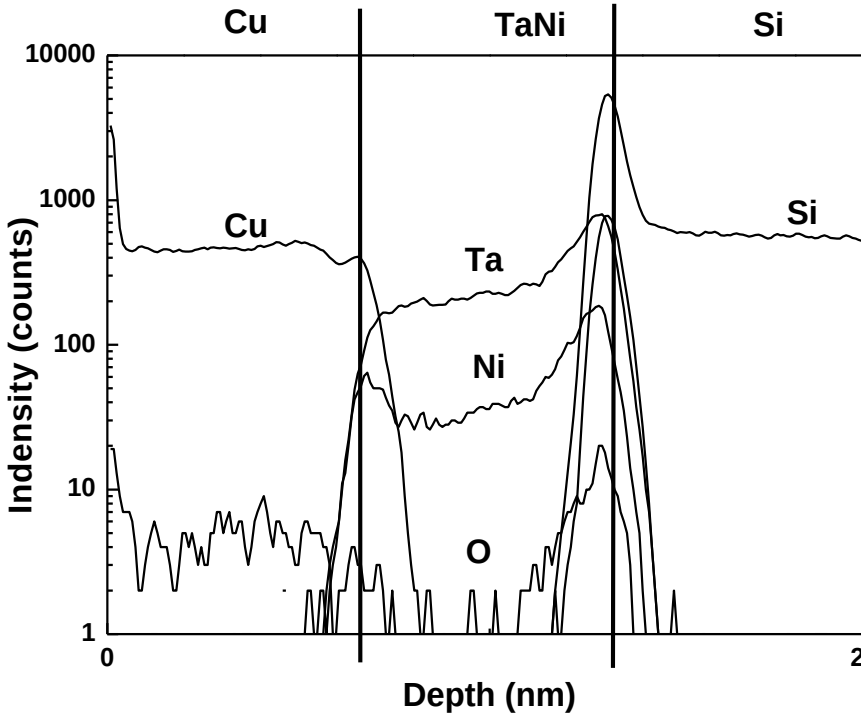
Cu
TaNi
Si
10000
1000
100
10
1
Indensity (counts)
Cu
Ta
Ni
O
Si
0
Depth (nm)

(b)

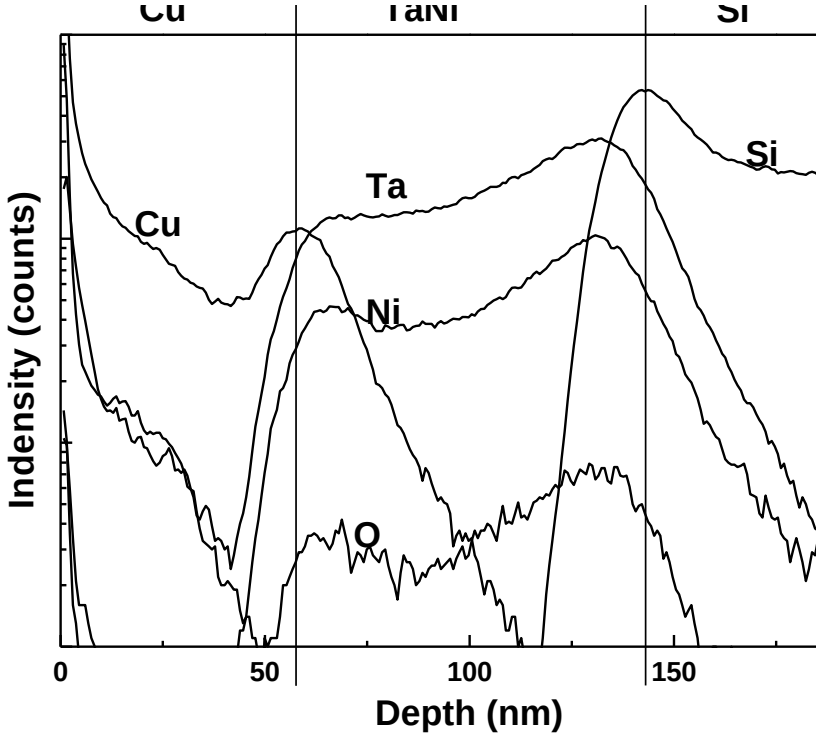
Cu
TaNi
Si
Indensity (counts)
Cu
Ta
Ni
O
Si
0
50
100
150
Depth (nm)

(c)

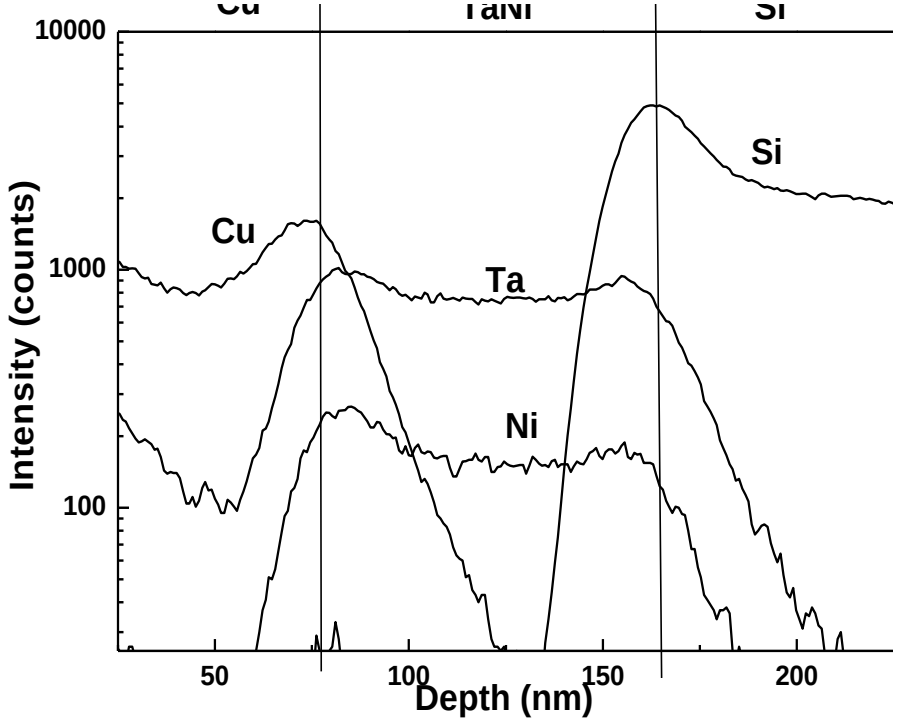
Cu
TaNi
Si
10000
1000
100
Intensity (counts)
Cu
Ta
Ni
Si
50
100
150
200
Depth (nm)

(d)

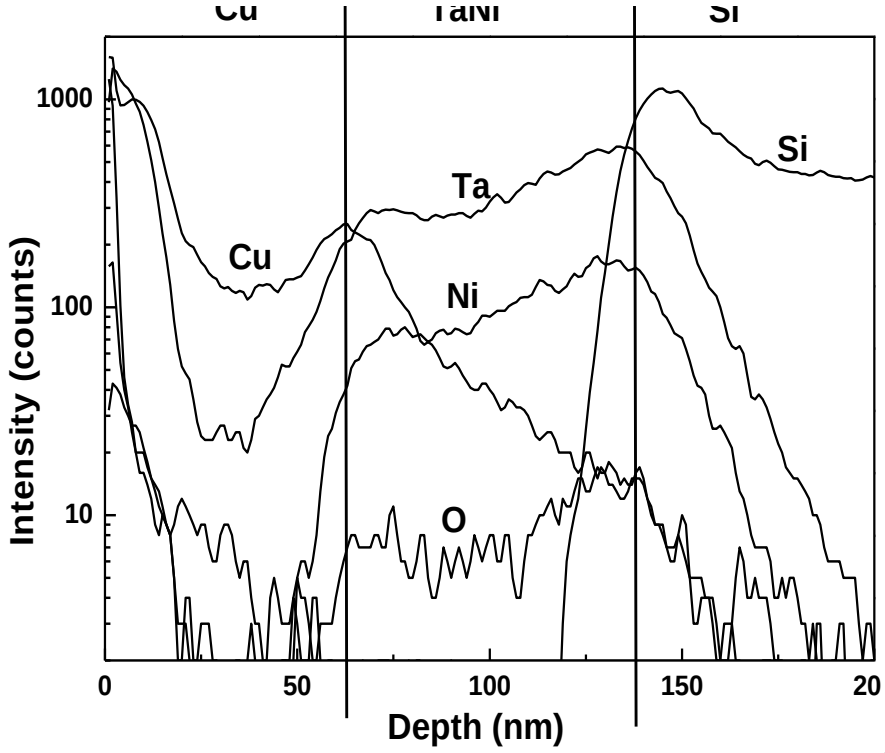
Cu
TaNi
Si
1000
100
10
Intensity (counts)
Cu
Ta
Ni
Si
O
0
50
100
150
20
Depth (nm)

(e)

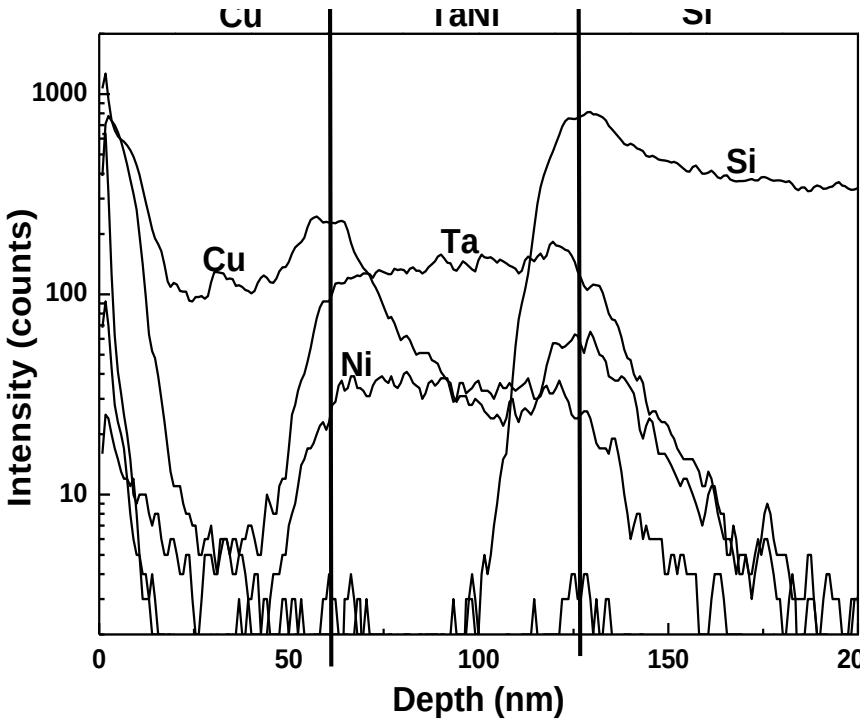

(f)

Fig. 7-9 ToF-SIMS depth profile of elements Cu, Ta, Ni O, Si of (a) Cu/$Ta_{67.34}Ni_{27.06}O_{5.60}$/Si at as-deposited state; (b) Cu/ $Ta_{73.25}Ni_{26.10}O_{0.65}$/Si at as-deposited state; (c) Cu/$Ta_{67.34}Ni_{27.06}O_{5.60}$/Si at 600 °C; (d) Cu/ $Ta_{73.25}Ni_{26.10}O_{0.65}$/Si at 600 °C; (e) Cu/$Ta_{67.34}Ni_{27.06}O_{5.60}$/Si at 700 °C; (f) Cu/ $Ta_{73.25}Ni_{26.10}O_{0.65}$/Si at 700 °C.

Fig. 7-10 shows the TEM pictures of Cu/$Ta_{73.25}Ni_{26.10}O_{0.65}$/Si and Cu/$Ta_{67.34}Ni_{27.06}O_{5.60}$ /Si at 600 °C, 700 °C and 800 °C. The interface remained clean between Ta-Ni and Si layers at 600 °C, showing no interfacial reaction or crystallization for both samples. At 700 °C, small nano-crystals were observed in Cu/$Ta_{73.25}Ni_{26.10}O_{0.65}$/Si at Ta-Ni and Si interface. EDX shows that these crystals are composed of Cu and Si with atomic ratio close to 3:1. The TEM and SIMS showed same finding. As observed in SIMS observation, there was a Cu signal hump at the Ta-Ni/Si interface, indicating accumulation of Cu at barrier/Si interface. The particles formed are believed to be Cu_3Si based on the atomic ratio. In Cu/$Ta_{67.34}Ni_{27.06}O_{5.60}$/Si, there was no secondary phase at $Ta_{67.34}Ni_{27.06}O_{5.60}$/Si interface. Instead, nano-grains were observed at

$Ta_{67.34}Ni_{27.06}O_{5.60}$/Cu interface, with high oxygen content detected by EDX. Thus it is believed that these grains belong to TaO_x, as Ta_2O_5 crystalline peaks were observed in XRD. At 800 °C, both films lost their integrity completely, with mixing of Cu and barrier film observed under TEM. This is in agreement with the XRD observation that high crystalline peaks appeared at 800 °C, belonging to Ta_2O_5, $TaSi_x$, $NiSi_x$, and no Cu peaks were observed.

As discussed, the oxygen in $Ta_{67.34}Ni_{27.06}O_{5.60}$ showed positive effect in blocking Cu diffusion into Si. Lower Cu concentration at $Ta_{67.34}Ni_{27.06}O_{5.60}$/Si interface was observed at the initial stage of the diffusion at 700 °C, which slowed down the formation of Cu_3Si.

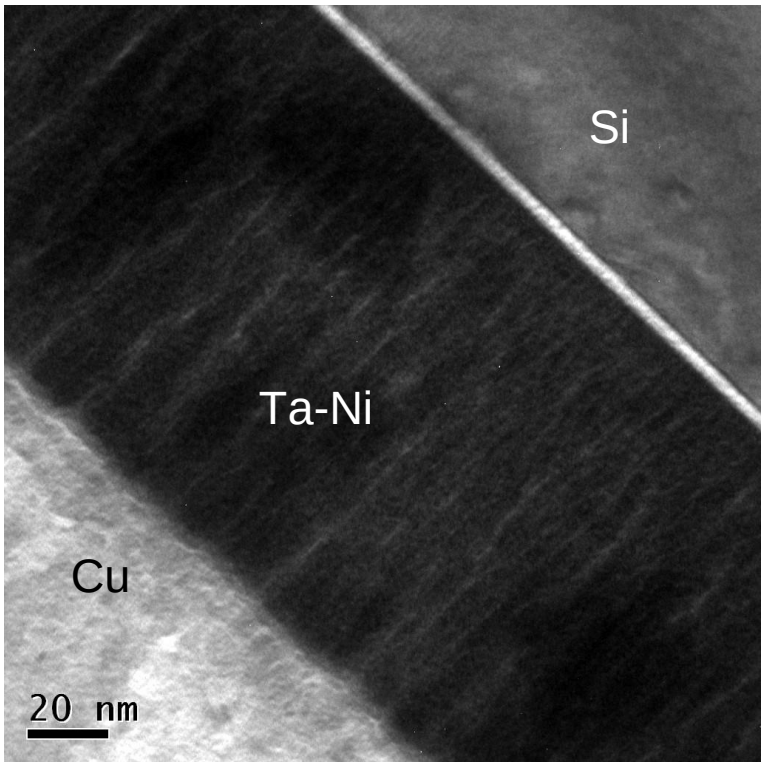

(a)

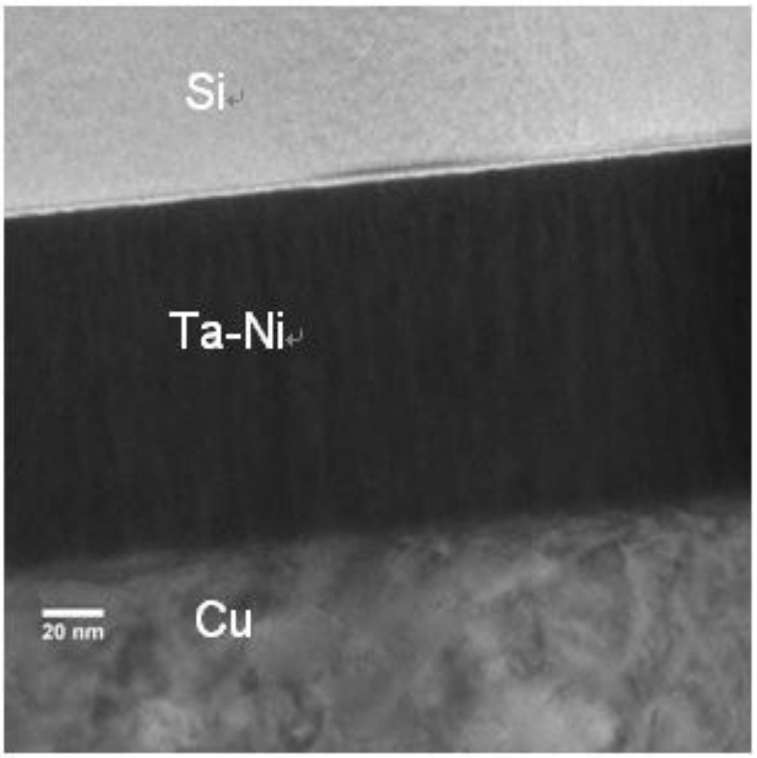

(b)

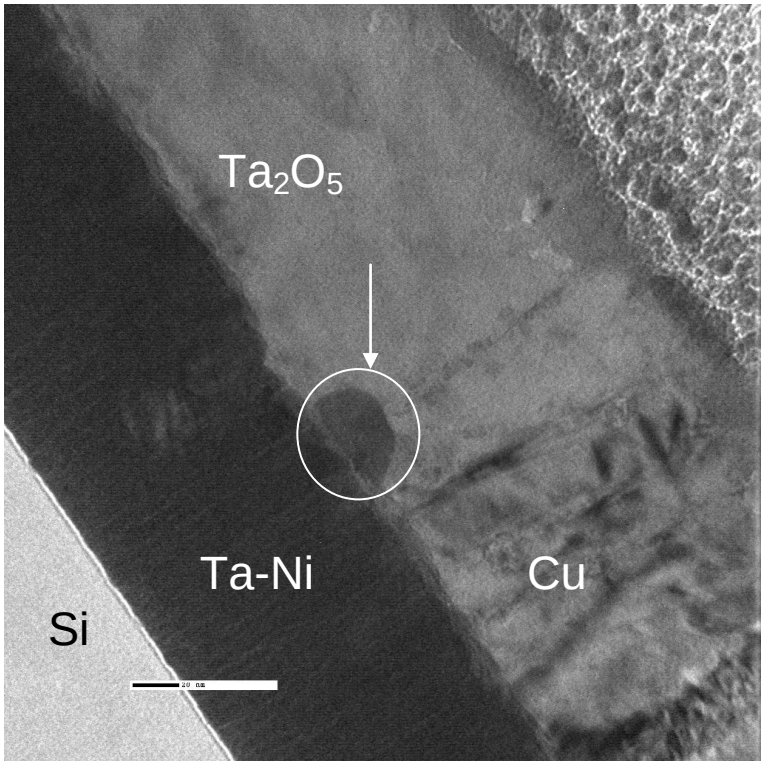

(c)

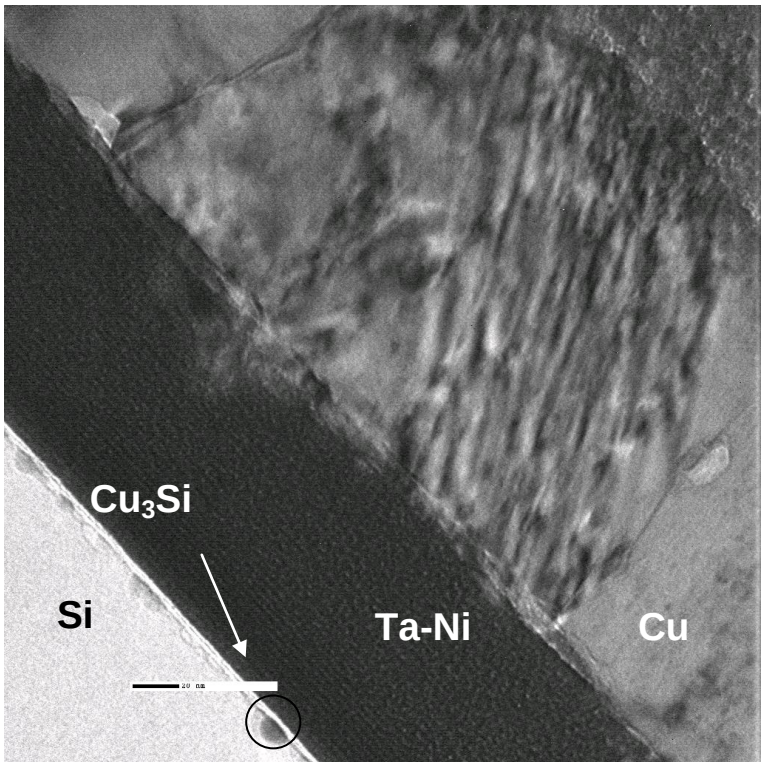

(d)

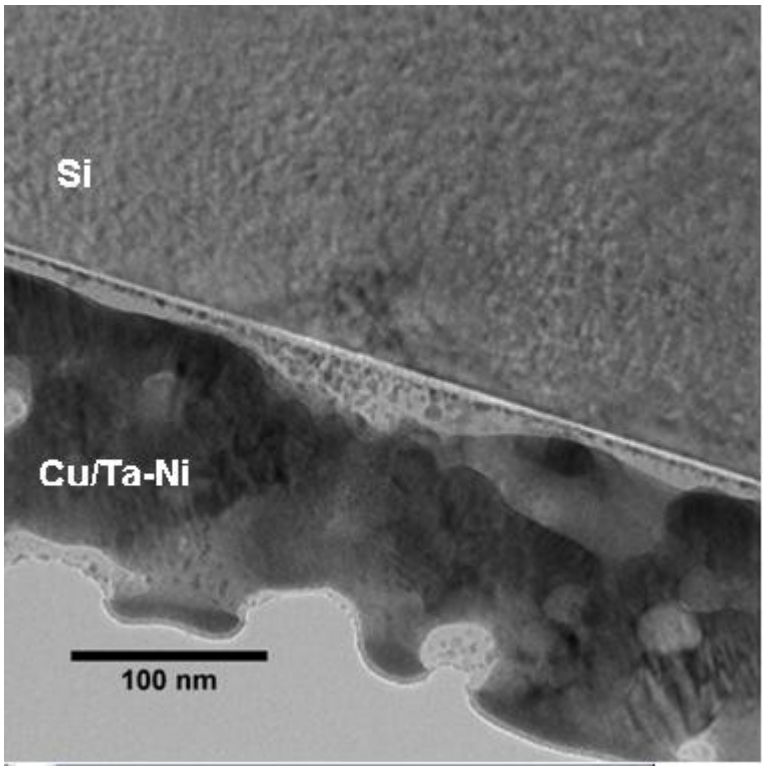

(e)

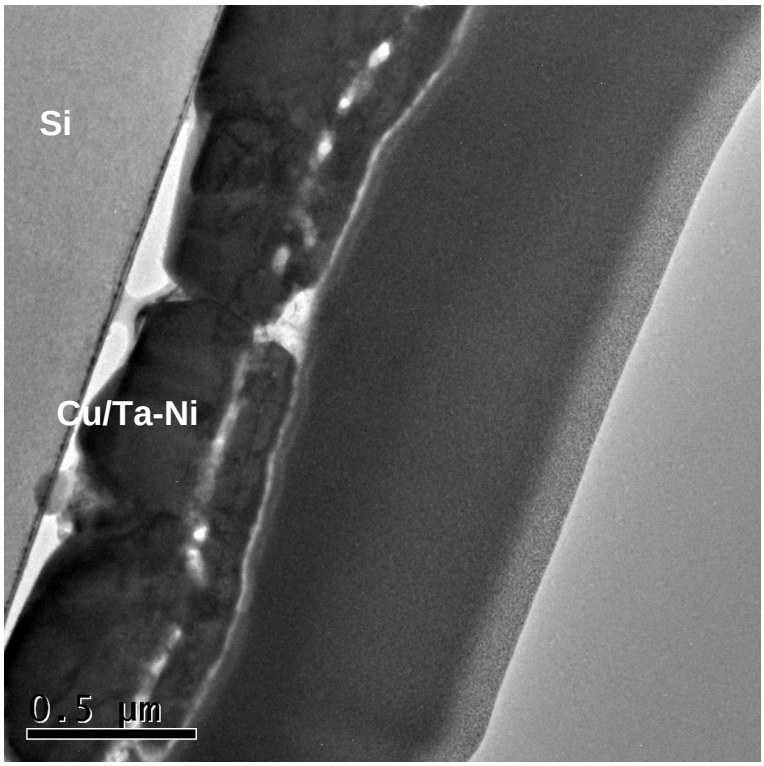

(f)

Fig. 7-10 TEM image of (a) Cu/$Ta_{67.34}Ni_{27.06}O_{5.60}$/Si at 600 °C; (b) Cu/$Ta_{73.25}Ni_{26.10}O_{0.65}$/Si at 600 °C; (c) Cu/$Ta_{67.34}Ni_{27.06}O_{5.60}$/Si at 700 °C; (d) Cu/$Ta_{73.25}Ni_{26.10}O_{0.65}$/Si at 700 °C; (e) Cu/$Ta_{67.34}Ni_{27.06}O_{5.60}$/Si at 800 °C; (f) Cu/$Ta_{73.25}Ni_{26.10}O_{0.65}$/Si at 800 °C.

7.2.4. Discussion

Based on the above analysis, the existence of oxygen is beneficial to prevent Cu diffusion. The formation of Cu_3Si was inhibited at 700 °C for $Ta_{67.34}Ni_{27.06}O_{5.60}$ barrier, while in $Ta_{73.25}Ni_{26.10}O_{0.65}$ with negligible oxygen content, Cu_3Si formed at the barrier/Si interface. The effect of oxygen in the barrier behavior is attributed to the stuffing effect at the Si/barrier interface, as well as the formation of Ta_2O_5 during annealing which inhibited the diffusion of Cu. The mechanism could be explained by the formation of thin Ta-O layer at the barrier/Si for oxygen rich barrier. The formation of Ta-O layer behaves as secondary barriers, and thus delayed the reaction between Cu and Si.

7.2.5. Summary

In this part, effect of oxygen in Ta-Ni on its Cu diffusion barrier performance was studied. Two Ta-Ni films with oxygen concentration of 5.6 at% and 0.65 at% were compared. XRD, SIMS and TEM studies showed that the growth of Cu_3Si nano-grains started at 700 °C at the Ta-Ni/Si interface for Cu/$Ta_{73.25}Ni_{26.10}O_{0.65}$/Si (lower oxygen concentration). In films with higher oxygen concentration, only Ta_2O_5 crystalline phases were observed at Cu/$Ta_{67.34}Ni_{27.06}O_{5.60}$ interface, while the $Ta_{67.34}Ni_{27.06}O_{5.60}$/Si interface remained clean at 700 °C. The delay of Cu_3Si formation for $Ta_{67.34}Ni_{27.06}O_{5.60}$ suggests that oxygen is beneficial in improving the Cu diffusion barrier performance.

Chapter 8. Conclusion and Recommendation

8.1. Summary of the current work

The current work studies the Cu diffusion barrier performance of Ta-based amorphous thin films including compound barriers and binary alloy barriers. The compound barriers include Ta-N and Ta-Si-N deposited by reactive sputtering of Ta and Si targets with N_2 precursor. The binary alloy barriers include Ta-Ni, Ta-Cr and Ta-Ti (Ta-TM) deposited by a co-sputtering of Ta and TM targets. Ta-Si-N film shows highest thermal stability up to 900 °C. The Ta-N and Ta-TM (except Ta-Ti) thin films showed amorphous structure up to 800 °C. Among all studied barriers, Ta-Ni is the best candidate for future application due to the combination of good barrier performance and low electrical resistance. Some findings are concluded from the current work.

8.1.1. Formation of amorphous Ta-N and Ta-Si-N thin films with high thermal stability

Ta-Si-N and Ta-N thin films were formed on Si substrate. All as-deposited films show amorphous phases with a wide range of composition. Thermal stability is lost for Ta-Si-N at 900 °C with Ta_2O_5 crystals formation. Ta-N loses the amorphous structure with Ta_2O_5 crystals growth at 800 °C. The chemical bonding states was studied to understand the mechanism of the high thermal stability. It was found that Ta-Si-N consists of $TaSi_xO_y$, TaN_x, TaO_x, and $TaSi_x$, while Ta-N consists of Ta, $Ta(ON)_x$, and Ta_2O_5. The complex system of Ta-Si-N might be the reason of its high thermal stability.

8.1.2. Formation of amorphous Ta-TM binary alloy thin films with high thermal stability

Ta-TM binary alloy thin films were deposited on Si substrate, showing different microstructures, electrical resistivities and thermal stabilities. The Ta-TM thin films show small variation in resistance with composition change. The electrical resistance is comparable with β-Ta barrier, and lower than Ta-N and Ta-Si-N compound barriers.

The GFA of binary thin films were estimated using the theoretical methods such as size difference method and structure difference method. These rules were usually applied in bulk amorphous materials design, and are verified to be valid for the Ta-TM thin film systems by the current work. They can be a useful tool for materials selection of amorphous alloy thin films formation.

The experimental and theoretical studies show that Ta-Ni and Ta-Cr have good glass forming ability (GFA), but Ta-Ti does not. At as-deposited state, Ta-Cr and Ta-Ni thin films are amorphous in a large composition range, while Ta-Ti shows crystalline phase. Solid amorphorization occurs for Ta-Ti films after 600 °C annealing. All the amorphorized films are stable up to 800 °C, similar as Ta-N. It shows that with the amorphous Ta-TM films can be as stable as metal-nitride compound with proper elements and compositions.

8.1.3. Barrier performance of Ta-based thin films

The Cu diffusion barrier performance of Ta-TM thin films was studied and compared with Ta and Ta-N, and Ta-Si-N. It shows that Ta-Si-N has the best barrier performance but high electrical resistivity, while Ta shows low electrical resistivity but poor barrier performance. The comparison concludes that Ta-TM provides promising barrier

properties. Ta-Ni is the best among all studied barriers because of its good barrier performance and low electrical resistance. A few guidelines are drawn based on the comparison of the barriers:

a) Barrier with stable amorphous structure provides better barrier performance than the crystalline structure.
b) Barrier which does not react with Si provides better barrier performance than barrier with potential reaction with Si.

8.1.4. Effect of oxygen on the films properties and barrier performance

We observed the beneficial effect of oxygen in thin film stability and barrier performance. Interfacial reaction happens between Ta-Ni barrier and Si at 800 °C in a film with higher O concentration, while in another Ta-Ni barrier with lower oxygen concentration, the interfacial reaction happens at 750 °C. As a result of better thermal stability, the diffusion barrier performance of oxygen-containing film is also improved. For Ta-Ni barrier with 0.56 at% of oxygen, formation of Cu_3Si at Ta-Ni/Si interface is observed at 700 °C, while for Ta-Ni barrier with 5.6 at% of oxygen, no Cu_3Si but only Ta_2O_5 is observed at 700 °C. Thus controlled amount of oxygen is beneficial for Cu diffusion barrier performance without much compromise in the electrical resistivity.

8.2. Recommendation for further work

8.2.1. Binary amorphous metallic thin films

The study of binary metallic glass has challenged many researchers [143, 155-156]. Conventionally, formation of metallic glass requires complex alloy system consisting

of several metallic elements with large atomic size difference [10, 157-158]. Binary alloy usually has low GFA because of the lack of complexity. As demonstrated in current work, formation of binary metallic glass thin films can be achieved through PVD process due to the fast densification. The amorphous phase can be obtained over a large composition range. Therefore, it could be of great interest to further extend the work on a series of binary alloy thin films. The following works are proposed for more in-depth understanding:

a) The criteria of forming binary metallic glass thin films

The current work shows that Ta-Ni, Ta-Cr and Ta-Ti lose the amorphous structure through different mechanisms, demonstrating that GFA of binary metallic glass depends on both the constituent elements, and the interaction between thin film and the substrate. Studies can be extended to other Ta-based binary alloys such as Ta-Co, Ta-Zn, Ta-V, to build up a more comprehensive database on the GFA of binary metallic thin films. Effect of the atomic size difference, chemical bonding and phase formation complexity on GFA can also be established with a comprehensive database.

b) Comparison between bulk metallic glass and metallic glass thin film

Bulk metallic glass and metallic glass thin film show different performance because of the different architectures. As the thin film technology has a wide range of applications, it is important to understand the differences and similarities between thin film metallic glass and bulk metallic glass, in term of amorphorization mechanism, crystallization mechanism, and mechanical, thermal and electrical properties.

c) The effect of formation method and substrate on the GFA of alloy thin films

As thin film can be formed by different methods such as PVD, CVD, PLD, and ALD, the kinetics in forming amorphous thin films using different deposition methods could be further studied. The effect of substrate material and structure on forming amorphous thin films needs to be studied with different substrates such as SiO_2, glass, metal substrate, etc.

8.2.2. Application of binary alloys as amorphous Cu barriers

This work shows that the Ta-TM thin films behave as good Cu diffusion barrier with comparable performance with Ta-N, while it also provides more attractive properties such as easier process control and lower electrical resistance. The barrier performances of Ta-Ni, Ta-Cr and Ta-Ti are demonstrated by the high failure temperature. Further studies are proposed to extend this work for more comprehensive understanding of

a) Reliability of Ta-based binary alloy barriers under electrical stress

The current study focuses on the barrier performance under thermal stress. In practical application, the circuit is under both electrical and thermal stresses. The barrier performance at electric field is critical in estimating the barrier performance as well. A BTS test could be designed to assess the barrier performance under thermal stress.

b) Barrier performance of other binary alloys

Besides Ta, Cu barriers based on other refractory metals such as W and Ru have also been investigated [6, 159-160]. Ru has been an attractive candidate because it can be used as seed layer for Cu direct plating; however Ru itself is not an effective Cu barrier. The barrier performance of the binary alloy based on W or Ru could also be similar as that of Ta, and thus provides more options for binary alloy barriers.

c) Barrier performance of studied barriers on dielectrics substrate

As discussed in introduction, Si substrate is used in current study, because Si forms Cu_3Si with Cu, which is a good indicator of Cu diffusion through barrier. In industrial application, Cu barrier barriers are mainly applied between Cu and dielectric layers. Because of the different interface interaction between barrier/Si and barrier/dielectric, barrier study on dielectric layers would be a potential direction of research towards industrial application.

References

[1] S.M. Sze, J.C. Irvin, Solid-State Electron. 11/6 (1968) 599.
[2] M. Miyazaki, M. Sano, S. Sumita, N. Fujino, Jpn. J. Appl. Phys. Part 2 - Lett. 30/2B (1991) L295.
[3] J. Baumann, C. Kaufmann, M. Rennau, T. Werner, T. Gessner, Microelectron. Eng. 33/1-4 (1997) 283.
[4] A.E. Kaloyeros, E. Eisenbraun, Annu. Rev. Mater. Sci. 30 (2000) 363.
[5] K. Holloway, P.M. Fryer, C. Cabral, J.M.E. Harper, P.J. Bailey, K.H. Kelleher, J. Appl. Phys. 71/11 (1992) 5433.
[6] T.N. Arunagiri, Y. Zhang, O. Chyan, M. El-Bouanani, M.J. Kim, K.H. Chen, C.T. Wu, L.C. Chen, Appl. Phys. Lett. 86/8 (2005).
[7] T. Oku, E. Kawakami, M. Uekubo, K. Takahiro, S. Yamaguchi, M. Murakami, Appl. Surf. Sci. 99/4 (1996) 265.
[8] J.S. Becker, R.G. Gordon, Appl. Phys. Lett. 82/14 (2003) 2239.
[9] C. Lee, Y.H. Shin, Mater. Chem. Phys. 57/1 (1998) 17.
[10] W.H. Wang, C. Dong, C.H. Shek, Materials Science and Engineering: R: Reports 44/2-3 (2004) 45.
[11] P.S. Ho, Thin Solid Films 96/4 (1982) 301.
[12] P.G. Shewmon, Diffusion in Solid, McGraw-Hill Book Company, 1963.
[13] V.B. Fiks, Sov. Phys. Solid State 1 (1959).
[14] H.B. Huntington, A.R. Grone, Journal of Physics and Chemistry of Solids 20/1-2 (1961) 76.
[15] A. Christou, Electromigration and Electronic Device Degradation, John Wiley and Sons, 1994.
[16] A. Scorzoni, B. Neri, C. Caprile, F. Fantini, Materials Science Reports 7/4-5 (1991) 143.
[17] C.S. Hau-Riege, C.V. Thompson, Appl. Phys. Lett. 78/22 (2001) 3451.
[18] G. NA, Am. Soc. Met, Westerville, OH, 1973.
[19] R.N. Hall, J.H. Racette, Journal of Applied Physics/35 (1964) 379.
[20] A.A. Istratov, C. Flink, H. Hieslmair, E.R. Weber, T. Heiser, Physical Review Letters 81/6 (1998) 1243.
[21] T. Heiser, A. Mesli, Applied Physics a-Materials Science & Processing 57/4 (1993) 325.
[22] A.A. Istratov, E.R. Weber, Journal of The Electrochemical Society 149/1 (2002) G21.
[23] U.M. Gosele, Annual Review of Materials Science 18/1 (1988) 257.
[24] A.A. Istratov, C. Flink, E.R. Weber, Phys. Status Solidi B-Basic Res. 222/1 (2000) 261.
[25] A.A. Istratov, H. Hedemann, M. Seibt, O.F. Vyvenko, W. Schroter, T. Heiser, C. Flink, H. Hieslmair, E.R. Weber, J. Electrochem. Soc. 145/11 (1998) 3889.
[26] A.A. Istratov, C. Flink, H. Hieslmair, S.A. McHugo, E.R. Weber, Materials Science and Engineering B-Solid State Materials for Advanced Technology 72/2-3 (2000) 99.
[27] T. Heiser, A.A. Istratov, C. Flink, E.R. Weber, Materials Science and Engineering B-Solid State Materials for Advanced Technology 58/1-2 (1999) 149.
[28] J.D. McBrayer, R.M. Swanson, T.W. Sigmon, Journal of The Electrochemical Society 133/6 (1986) 1242.
[29] G. Raghavan, C. Chiang, P.B. Anders, S.-M. Tzeng, R. Villasol, G. Bai, M. Bohr, D.B. Fraser, Thin Solid Films 262/1-2 (1995) 168.
[30] B.G. Willis, D.V. Lang, Thin Solid Films 467/1-2 (2004) 284.

[31] A.L.S. Loke, J.T. Wetzel, P.H. Townsend, T. Tanabe, R.N. Vrtis, M.P. Zussman, D. Kumar, C. Ryu, S.S. Wong, Ieee Transactions on Electron Devices 46/11 (1999) 2178.
[32] F. Lanckmans, W.D. Gray, B. Brijs, K. Maex, Microelectronic Engineering 55/1-4 (2001) 329.
[33] J.W.M. DuMond, J.P. Youtz, Physical Review 48/8 (1935) 703.
[34] M.A. Nicolet, Thin Solid Films 52/3 (1978) 415.
[35] M.A. Nicolet, Thin Solid Films 52/3 (1978) 415.
[36] P.B. Barna, M. Adamik, Thin Solid Films 317/1-2 (1998) 27.
[37] K.-L. Ou, M.-S. Yu, R.-Q. Hsu, M.-H. Lin, Journal of Vacuum Science and Technology B: Microelectronics and Nanometer Structures 23/1 (2005) 229.
[38] A.E. Kaloyeros, E. Eisenbraun, Annual Review of Materials Science 30/1 (2000) 363.
[39] S.Q. Wang, Mrs Bulletin 19/8 (1994) 30.
[40] S. Rawal, D.P. Norton, A. Hiral, T.J. Anderson, L. McElwee-White, Applied Physics Letters 90/5 (2007) 051913.
[41] J.P. Jacquemin, E. Labonne, C. Yalicheff, E. Royet, P. Vannier, R. Delsol, P. Normandon, Microelectronic Engineering 82/3-4 (2005) 613.
[42] X.-P. Qu, J.-J. Tan, M. Zhou, T. Chen, G.-P. Ru, B.-Z. Li, Materials Research Society, Warrendale, PA 15086, United States, San Francisco, CA, United States, 2006, p. 149.
[43] X.-P. Qu, J.-J. Tan, M. Zhou, T. Chen, Q. Xie, G.-P. Ru, B.-Z. Li, Applied Physics Letters 88/15 (2006) 151912.
[44] M. Stavrev, D. Fischer, C. Wenzel, K. Drescher, N. Mattern, Thin Solid Films 307/1-2 (1997) 79.
[45] K. Holloway, P.M. Fryer, J. Cyril Cabral, J.M.E. Harper, P.J. Bailey, K.H. Kelleher, Journal of Applied Physics 71/11 (1992) 5433.
[46] Y.C. Ee, Z. Chen, W.D. Wang, D.Z. Chi, S. Xu, S.B. Law, Surface & Coatings Technology 198/1-3 (2005) 291.
[47] C. Chin-An, H. Chao-Kun, Applied Physics Letters 57/6 (1990) 617.
[48] K.C. Park, K.B. Kim, Journal of the Electrochemical Society 142/9 (1995) 3109.
[49] K.T. Nam, A. Datta, S.H. Kim, K.B. Kim, Applied Physics Letters 79/16 (2001) 2549.
[50] S.K. Rha, W.J. Lee, S.Y. Lee, Y.S. Hwang, Y.J. Lee, D.I. Kim, D.W. Kim, S.S. Chun, C.O. Park, Thin Solid Films 320/1 (1998) 134.
[51] G. Bai, S. Wittenbrock, V. Ochoa, R. Villasol, C. Chiang, T. Marieb, D. Gardner, C. Mu, D. Fraser, M. Bohr, in: H.J. Frost, M.A. Parker, C.A. Ross, E.A. Holm (Eds.), Polycrystalline Thin Films: Structure, Texture, Properties, and Applications Ii, vol. 403, Materials Research Soc, Pittsburgh, 1996, p. 501.
[52] T. Laurila, K. Zeng, J.K. Kivilahti, J. Molarius, I. Suni, Thin Solid Films 373/1-2 (2000) 64.
[53] M. Stavrev, D. Fischer, A. Preuss, C. Wenzel, N. Mattern, Microelectron. Eng. 33/1-4 (1997) 269.
[54] D.S. Yoon, H.K. Baik, S.M. Lee, J. Vac. Sci. Technol. B 17/1 (1999) 174.
[55] M. Lane, R.H. Dauskardt, N. Krishna, I. Hashim, J. Mater. Res. 15/1 (2000) 203.
[56] M. Stavrev, C. Wenzel, A. Moller, K. Drescher, Appl. Surf. Sci. 91/1-4 (1995) 257.
[57] M.T. Wang, Y.C. Lin, M.C. Chen, J. Electrochem. Soc. 145/7 (1998) 2538.
[58] K.H. Min, K.C. Chun, K.B. Kim, J. Vac. Sci. Technol. B 14/5 (1996) 3263.
[59] G.S. Chen, P.Y. Lee, S.T. Chen, Thin Solid Films 353/1-2 (1999) 264.

[60]W.L. Yang, W.F. Wu, D.G. Liu, C.C. Wu, K.L. Ou, Solid-State Electron. 45/1 (2001) 149.
[61]M. Hecker, D. Fischer, V. Hoffmann, H.J. Engelmann, A. Voss, N. Mattern, C. Wenzel, C. Vogt, E. Zschech, Thin Solid Films 414/2 (2002) 184.
[62]W.F. Wu, K.L. Ou, C.P. Chou, C.C. Wu, Journal of the Electrochemical Society 150/2 (2003) G83.
[63]M. Takeyama, A. Noya, T. Sase, A. Ohta, K. Sasaki, J. Vac. Sci. Technol. B 14/2 (1996) 674.
[64]J.C. Lin, C. Lee, J. Electrochem. Soc. 146/9 (1999) 3466.
[65]M.H. Tsai, S.C. Sun, C.E. Tsai, S.H. Chuang, H.T. Chiu, J. Appl. Phys. 79/9 (1996) 6932.
[66]C.C. Chang, J.S. Jeng, J.S. Chen, Thin Solid Films 413/1-2 (2002) 46.
[67]G.S. Chen, S.T. Chen, L.C. Yang, P.Y. Lee, J. Vac. Sci. Technol. A-Vac. Surf. Films 18/2 (2000) 720.
[68]R. Hubner, M. Hecker, N. Mattern, V. Hoffmann, K. Wetzig, C. Wenger, H.J. Engelmann, C. Wenzel, E. Zschech, J.W. Bartha, Thin Solid Films 437/1-2 (2003) 248.
[69]C.C. Chang, F.M. Pan, C.W. Chen, J. Electrochem. Soc. 157/2 (2010) G62.
[70]Q. Xie, X.P. Qu, J.J. Tan, Y.L. Jiang, M. Zhou, T. Chen, G.P. Ru, Appl. Surf. Sci. 253/3 (2006) 1666.
[71]X.M. Chen, H.L. Frisch, A.E. Kaloyeros, B. Arkles, J. Sullivan, J. Vac. Sci. Technol. B 17/1 (1999) 182.
[72]Y. Senzaki, A.K. Hochberg, J.A.T. Norman, Adv. Mater. Opt. Electron. 10/3-5 (2000) 93.
[73]H. Kim, A.J. Kellock, S.M. Rossnagel, J. Appl. Phys. 92/12 (2002) 7080.
[74]H. Kim, C. Lavoie, M. Copel, V. Narayanan, D.G. Park, S.M. Rossnagel, J. Appl. Phys. 95/10 (2004) 5848.
[75]O. van der Straten, Y. Zhu, K. Dunn, E.T. Eisenbraun, A.E. Kaloyeros, J. Mater. Res. 19/2 (2004) 447.
[76]E. Langereis, H.C.M. Knoops, A.J.M. Mackus, F. Roozeboom, M.C.M. van de Sanden, W.M.M. Kessels, J. Appl. Phys. 102/8 (2007).
[77]O. Chyan, T.N. Arunagiri, T. Ponnuswamy, J. Electrochem. Soc. 150/5 (2003) C347.
[78]R. Chan, T.N. Arunagiri, Y. Zhang, O. Chyan, R.M. Wallace, M.J. Kim, T.Q. Hurd, Electrochemical and Solid-State Letters 7/8 (2004) 154.
[79]T.N. Arunagiri, Y. Zhang, O. Chyan, M. El-Bouanani, M.J. Kim, K.H. Chen, C.T. Wu, L.C. Chen, Applied Physics Letters 86/8 (2005) 83104.
[80]M. Damayanti, T. Sritharan, S.G. Mhaisalkar, Z.H. Gan, Applied Physics Letters 88/4 (2006) 044101.
[81]J.H. Shin, H.W. Kim, K. Agapiou, R.A. Jones, G.S. Hwang, J.G. Ekerdt, J. Vac. Sci. Technol. A 26/4 (2008) 974.
[82]K. Soo-Hyun, N. Ki Tae, A. Datta, K. Hyun-Mi, K. Ki-Bum, K. Dae-Hwan, Journal of Vacuum Science & Technology B (Microelectronics and Nanometer Structures) 21/2 (2003) 804.
[83]S.H. Kwon, O.K. Kwon, J.S. Min, S.W. Kang, J. Electrochem. Soc. 153/6 (2006) G578.
[84]J.J. Tan, X.P. Qu, Q. Xie, Y. Zhou, G.P. Ru, Thin Solid Films 504/1-2 (2006) 231.
[85]Q. Xin-Ping, T. Jing-Jing, Z. Mi, C. Tao, X. Qi, R. Guo-Ping, L. Bing-Zong, Applied Physics Letters 88/15 (2006) 151912.

[86]E. Blanquet, A.M. Dutron, V. Ghetta, C. Bernard, R. Madar, Microelectron. Eng. 37-8/1-4 (1997) 189.
[87]M.S. Angyal, Y. Shachamdiamand, J.S. Reid, M.A. Nicolet, Appl. Phys. Lett. 67/15 (1995) 2152.
[88]H. Park, J. Lim, C. Lee, in: W. Pan, J.H. Gong, C.C. Ge, J.F. Li (Eds.), High-Performance Ceramics Iii, Pts 1 and 2, vol. 280-283, Trans Tech Publications Ltd, Zurich-Uetikon, 2005, p. 911.
[89]J.S. Reid, X. Sun, E. Kolawa, M.A. Nicolet, IEEE Electron Device Lett. 15/8 (1994) 298.
[90]Y.C. Ee, Z. Chen, S.B. Law, S. Xu, Thin Solid Films 504/1-2 (2006) 218.
[91]Y.C. Ee, Z. Chen, S.B. Law, S. Xu, N.L. Yakovlev, M.Y. Lai, Appl. Surf. Sci. 253/2 (2006) 530.
[92]J.S. Reid, R.Y. Liu, P.M. Smith, R.P. Ruiz, M.A. Nicolet, Thin Solid Films 262/1-2 (1995) 218.
[93]S.T. Lin, C. Lee, Appl. Surf. Sci. 253/3 (2006) 1215.
[94]S. Rawal, D.P. Norton, H. Ajmera, T.J. Anderson, L. McElwee-White, Appl. Phys. Lett. 90/5 (2007).
[95]Y.Z. Liu, S.X. Song, D.L. Mao, H.Q. Ling, M. Li, Microelectron. Eng. 75/3 (2004) 309.
[96]A. Kohn, M. Eizenberg, Y. Shacham-Diamand, Y. Sverdlov, Mater. Sci. Eng. A-Struct. Mater. Prop. Microstruct. Process. 302/1 (2001) 18.
[97]Y.J. Lee, B.S. Suh, M.S. Kwon, C.O. Park, J. Appl. Phys. 85/3 (1999) 1927.
[98]R. Hubner, M. Hecker, N. Mattern, A. Voss, J. Acker, V. Hoffmann, K. Wetzig, H.J. Engelmann, E. Zschech, H. Heuer, C. Wenzel, Thin Solid Films 468/1-2 (2004) 183.
[99]J.T. No, J.H. O, C. Lee, Mater. Chem. Phys. 63/1 (2000) 44.
[100]R. Hubner, M. Hecker, N. Mattern, V. Hoffmann, K. Wetzig, H. Heuer, C. Wenzel, H.J. Engelmann, D. Gehre, E. Zschech, Thin Solid Films 500/1-2 (2006) 259.
[101]H. Yan, L. Li, F.Y. Ho, M.H. Liang, J.S. Pan, S. Xu, Z. Chen, Thin Solid Films 517/17 (2009) 5207.
[102]J.S. Reid, E. Kolawa, R.P. Ruiz, M.A. Nicolet, Thin Solid Films 236/1-2 (1993) 319.
[103]E. Kolawa, J.S. Chen, J.S. Reid, P.J. Pokela, M.A. Nicolet, Journal of Applied Physics 70/3 (1991) 1369.
[104]C.E. Ramberg, E. Blanquet, M. Pons, C. Bernard, R. Madar, Microelectron. Eng. 50/1-4 (2000) 357.
[105]Y.C. Ee, Z. Chen, T.M. Lu, Z.L. Dong, S.B. Law, Electrochem. Solid State Lett. 9/3 (2006) G100.
[106]J.O. Olowolafe, I. Rau, K.M. Unruh, C.P. Swann, Z.S. Jawad, T. Alford, Thin Solid Films 365/1 (2000) 19.
[107]C.K. Chung, T.S. Chen, C.C. Peng, B.H. Wu, Surface and Coatings Technology 201/7 (2006) 3947.
[108]S.Q. Wang, S. Suthar, C. Hoeflich, B.J. Burrow, Journal of Applied Physics 73/5 (1993) 2301.
[109]J.S. Fang, T.P. Hsu, G.S. Chen, TMS; IEEE, Charlotte, NC, USA, 2004, p. 1176.
[110]A. Noya, M.B. Takeyama, T. Sase, Journal of Vacuum Science & Technology B 23/1 (2005) 280.
[111]J.S. Fang, T.P. Hsu, G.S. Chen, Journal of Electronic Materials 35/1 (2006) 15.
[112]J. Forster, P. Gopalraja, T.J. Gung, A. Sundarrajan, X. Fu, N. Hammond, J. Fu, U. Kelkar, A. Bhatnagar, Microelectronic Engineering 82/3-4 (2005) 594.

[113]H. Park, J. Lin, C. Lee, Key Engineering Materials 280-283/pt.2 (2005) 911.
[114]J. Liu, W.D. Wang, L. Wang, D.Z. Chi, K.P. Loh, Materials, Technology and Reliability for Advanced Interconnects and Low-k Dielectrics-2004, 13-15 April 2004, Materials Research Soc, San Francisco, CA, USA, 2004, p. 147.
[115]A.E. Kaloyeros, J. Kelsey, C. Goldberg, D. Anjum, X. Chen, J. Mirza, K. Kumar, B. Arkles, B. Han, J.J. Sullivan, Advanced Interconnects and Contact Materials and Processes for Future Integrated Circuits. Symposium, 13-16 April 1998, Mater. Res. Soc, San Francisco, CA, USA, 1998, p. 499.
[116]E. Blanquet, A.M. Dutron, V. Ghetta, C. Bernard, R. Madar, Microelectronic Engineering 37-38 (1997) 189.
[117]D.-H. Kim, S.-L. Cho, K.-B. Kim, J.J. Kim, J.W. Park, J.J. Kim, Applied Physics Letters 69/27 (1996) 4182.
[118]G. Beyer, A. Satta, J. Schuhmacher, K. Maex, W. Besling, O. Kilpela, H. Sprey, G. Tempel, Microelectronic Engineering 64/1-4 (2002) 233.
[119]K.E. Elers, V. Saanila, P.J. Soininen, W.M. Li, J.T. Kostamo, S. Haukka, J. Juhanoja, W.F.A. Besling, Chemical Vapor Deposition 8/4 (2002) 149.
[120]K. Se-Hun, K. Oh-Kyum, M. Jae-Sik, K. Sang-Won, Journal of the Electrochemical Society 153/6 (2006) 578.
[121]H. Kim, Surface and Coatings Technology 200/10 (2006) 3104.
[122]K. Maex, M.R. Baklanov, D. Shamiryan, F. lacopi, S.H. Brongersma, Z.S. Yanovitskaya, Journal of Applied Physics 93/11 (2003) 8793.
[123]D.J. Kim, S.P. Jeong, Y.T. Kim, J.-W. Park, Polycrystalline Thin Films - Structure, Texture, Properties and Applications III. Symposium, 31 March-4 April 1997, Mater. Res. Soc, San Francisco, CA, USA, 1997, p. 331.
[124]R. Hubner, M. Hecker, N. Mattern, V. Hoffmann, K. Wetzig, H. Heuer, C. Wenzel, H.-J. Engelmann, D. Gehre, E. Zschech, Thin Solid Films 500/1-2 (2006) 259.
[125]L.W. Lai, J.S. Chen, W.-S. Hsu, Journal of Applied Physics 94/8 (2003) 5396.
[126]X. Sun, E. Kolawa, S. Im, C. Garland, M.A. Nicolet, Applied Physics A (Materials Science Processing) A65/1 (1997) 43.
[127]F. Faupel, W. Frank, M.P. Macht, H. Mehrer, V. Naundorf, K. Ratzke, H.R. Schober, S.K. Sharma, H. Teichler, Rev. Mod. Phys. 75/1 (2003) 237.
[128]P.C. Millett, R.P. Stelvam, A. Saxena, Acta Materialia (2007).
[129]C.E. Ramberg, E. Blanquet, M. Pons, C. Bernard, R. Madar, Elsevier, Ostende, Belgium, 2000, p. 357.
[130]G. Ouyang, C.X. Wang, G.W. Yang, Applied Physics Letters 86/17 (2005).
[131]L. Tian, M.O. Thompson, R. Dieckmann, C.-Y. Hui, Y.-Y. Lin, Journal of Applied Physics 90/8 (2001) 3799.
[132]W.N. Gill, J.L. Plawsky, Thin Solid Films 515/11 (2007) 4794.
[133]S.-H. Wang, C.-C. Chang, J.S. Chen, Effects of substrate bias and nitrogen flow ratio on the resistivity, density, stoichiometry, and crystal structure of reactively sputtered ZrNx thin films, AVS, 2004.
[134]C.-C. Chang, J.S. Jeng, J.S. Chen, Thin Solid Films 413/1-2 (2002) 46.
[135]S.M. Aouadi, M. Debessai, Journal of Vacuum Science & Technology A: Vacuum, Surfaces, and Films 22/5 (2004) 1975.
[136]J.C. Chuang, M.C. Chen, J. Electrochem. Soc. 145/11 (1998) 4029.
[137]L.A. Clevenger, N.A. Bojarczuk, K. Holloway, J.M.E. Harper, C. Cabral, R.G. Schad, F. Cardone, L. Stolt, J. Appl. Phys. 73/1 (1993) 300.
[138]A.J. Drehman, A.L. Greer, D. Turnbull, Appl. Phys. Lett. 41/8 (1982) 716.
[139]T. Egami, Y. Waseda, Journal of Non-Crystalline Solids 64/1-2 (1984) 113.

[140]B.-X. Liu, W.L. Johnson, M.A. Nicolet, S.S. Lau, Appl. Phys. Lett. 42/1 (1983) 45.
[141]F.R. De Boer, R. Boom, W. Mattens, A. Miedema, A. Niessen, Cohesion in metals: transition metal alloys, North-Holland Amsterdam, 1988.
[142]T. Egami, Y. Waseda, Journal of Non-Crystalline Solids 64/1–2 (1984) 113.
[143]J.H. Li, Y. Dai, Y.Y. Cui, B.X. Liu, Materials Science and Engineering: R: Reports 72/1-2 (2011) 1.
[144]A. Inoue, Acta Materialia 48/1 (2000) 279.
[145]L.A. Clevenger, A. Mutscheller, J.M.E. Harper, C. Cabral, K. Barmak, J. Appl. Phys. 72/10 (1992) 4918.
[146]H. Yan, Y.Y. Tay, M.H. Liang, Z. Chen, C.M. Ng, J.S. Pan, H. Xu, C. Liu, V.V. Silberschmidt, 2009 11th Electronics Packaging Technology Conference (EPTC 2009), 9-11 Dec. 2009, IEEE, Piscataway, NJ, USA, 2009, p. 567.
[147]C.-Y. Yang, J.S. Jeng, J.S. Chen, Thin Solid Films 420-421 (2002) 398.
[148]K.M. Latt, Y.K. Lee, T. Osipowicz, H.S. Park, Materials Science and Engineering B-Solid State Materials for Advanced Technology 94/1 (2002) 111.
[149]C. Li, J.H. Hsieh, Z.Z. Tang, J.-C. Cheng, Thin Solid Films 517/17 (2009) 5087.
[150]J.S. Fang, T.P. Hsu, H.C. Chen, J. Electron. Mater. 36/5 (2007) 614.
[151]Z.L. Yuan, D.H. Zhang, C.Y. Li, K. Prasad, C.M. Tan, Thin Solid Films 462-463 (2004) 279.
[152]H. Yan, R.N. Santoso, Y. Jiang, M.H. Liang, Z. Chen, Thin Solid Films/Summitted.
[153]T. Laurila, K.J. Zeng, J.K. Kivilahti, J. Molarius, I. Suni, J. Mater. Res. 16/10 (2001) 2939.
[154]J.W. Lim, K. Mimura, K. Miyake, M. Yamashita, M. Isshiki, Jpn. J. Appl. Phys. Part 1 - Regul. Pap. Short Notes Rev. Pap. 42/5A (2003) 2780.
[155]C.V. Thompson, F. Spaepen, Acta Metallurgica 31/12 (1983) 2021.
[156]D. Wang, Appl. Phys. Lett. 84/20 (2004) 4029.
[157]C.T. Liu, M.F. Chisholm, M.K. Miller, Intermetallics 10/11-12 (2002) 1105.
[158]Z.P. Lu, C.T. Liu, Acta Materialia 50/13 (2002) 3501.
[159]J.B. Yeh, D.C. Perng, K.C. Hsu, J. Electrochem. Soc. 157/8 (2010) H810.
[160]L.B. Henderson, J.G. Ekerdt, Thin Solid Films 517/5 (2009) 1645.